Optimisation Framework for the Design of Multilayered Cord-Rubber Hoses

B. Herremans

Delft University of Technology

TU Delft

TANIQ

Optimisation Framework for the Design of Multilayered Cord-Rubber Hoses

by

B. Herremans

to obtain the degree of Master of Science in Aerospace Engineering
at the Delft University of Technology,
to be defended publicly on Thursday April 2, 2020 at 14:00.

Student number:	4289579	
Project duration:	March 11, 2019 – Apr 2, 2020	
Thesis supervisors:	Dr. ir. D.M.J. Peeters,	TU Delft
	ir. P. Mouri	TANIQ

An electronic version of this thesis is available at `https://repository.tudelft.nl/`.

TU Delft TANIQ

Delft University of Technology
Faculty of Aerospace Engineering
Department of Aerospace Manufacturing Technologies

GRADUATION COMMITTEE

Dated: April 2nd, 2020

Chair holder:

Prof. C.A. Dransfeld

Committee members:

Dr.ir. D.M.J. Peeters

Dr.ir. J.M.J.F. van Campen

ir. P. Mouri

Acknowledgements

This Master Thesis would not have been possible without the support of many individuals, to whom I'd like to express my gratitude.

Thanks to Peyman Mouri, for his guidance and mentoring over the course of the project. His knowledge on the analysis of cord-rubber products was invaluable to the success of this project. I greatly appreciate his openness for quick discussions, allowing swift and critical feedback on analysis results.

Thanks to Dr. Daniël Peeters, my supervisor at the Faculty of Aerospace Engineering. I highly appreciated the weekly discussions, where his critical questions continuously challenged my conclusions. While writing this thesis, his feedback was always profound and detailed.

Thanks to Dr. Julien van Campen, my initial supervisor at the Faculty of Aerospace Engineering, for his interest in the project. His professional history at TANIQ and knowledge of the topic guided me during the early stages of the project. I am delighted to welcome Dr. van Campen on my graduation committee.

Thanks to my colleagues at TANIQ, for their patience and help throughout the project. They made my time at TANIQ such a great experience, for which I am very grateful.

Finally, thanks to TU Delft, for their swift response to COVID-19 and allowing my thesis presentation and defence to be held online, an extraordinary and quite unique experience.

B. Herremans
Delft, April 2020

Abstract

Historically, high-pressure large diameter cord-reinforced rubber hoses have been manufactured using a manual labour-intensive process. These hoses, used in e.g. the petrochemical and mining industries, need to achieve burst pressures up to 75 bar. TANIQ, a Rotterdam-based company, improved and accelerated the manufacturing process by using a rotating mandrel and robotic arm. Until now design optimisations were performed iteratively, which is a time-consuming process. With the aim of reducing the cord usage in TANIQ's Large Bore Hose product family, an optimisation framework was developed.

Currently a three-dimensional model was used in finite element analysis, where truss elements represented actual cord placement, which is computationally too expensive to be feasibly used in a design optimisation algorithm. To decrease the finite element analysis time, an axisymmetric finite element model was developed using ABAQUS's rebar method. This method smear the directional cord properties over surface elements, making the Large Bore Hose quasi-axisymmetric. The two-dimensional rebar method showed an increased stability compared to the three-dimensional truss method in finite element models of various complexity, while resulting in a analysis time reduction of up to 70 %. A difference between both methods has been observed, which was deemed acceptable for the optimisation process but is recommended to be investigated during validation of the finite element model.

The relation between radial and axial variation of the cord angles on the deformation behaviour of and the strain distribution in cylindrical cord-rubber pressure vessels was studied, resulting in several design guidelines. Peak strain was shown to be dependent on the both the angle difference between the inner and outer cord layers, and the difference between the average cord angle and the structure's neutral angle (the direction of major principal stress). It was proven that the axial location of the peak strain can be tailored by axial variation of the cord angles.

A four-dimensional surrogate model was used to disconnect the finite element analyses from the optimisation algorithm. Subsequently, this surrogate model was used in a series of genetic algorithm optimisations to identify the cord angles resulting in the lowest peak strain in cylindrical pressure vessels. This approach was applied in a case study on the Large Bore Hose product family, where the cord angle configuration resulting in the lowest cord usage was identified with a 69 % success rate. The proposed design resulted in a cord usage reduction of 14.9 % was achieved relative to a real-life reference design.

Contents

Nomenclature

Abbreviations

CLT	Classical Lamination Theory
CPU	Central Processing Unit
DACE	Design and Analysis of Computer Experiments
FE	Finite Element
FEA	Finite Element Analysis
GA	Genetic Algorithm
LBH	Large Bore Hose
MLC	Multilayered Cylinder
OF	Optimisation Framework
PET	Polyethylene Terephthalate
RFL	Resorcinol Formaldehyde Latex

Greek symbols

λ_i	Stretch in orthogonal principal orientation

Latin symbols

$\boldsymbol{C}$	Cauchy-Green strain tensor
I_i	Cauchy-Green strain tensor invariant
W	Strain energy density

ABAQUS elements

C3D8H Continuum three-dimensional 8-node linear brick with hybrid formulation

CGAX4H Continuum axisymmetric with twist 4-node linear quadrilateral with hybrid formulation

SFM3D4 Membrane-like three-dimensional 4-node linear surface

SFMGAX1 Membrane-like axisymmetric with twist 2-node linear surface

T3D2 Three-dimensional 2-node linear truss

1

Introduction

TANIQ, an R&D company founded in 2006 as a spin-off of the Aerospace Engineering faculty of Delft University of Technology, aims to "**provide solutions to manufacturers of (mandrel-built) reinforced rubber products**"[1] by providing design software and automating the manufacturing process. This thesis focusses on the design optimisation of the Large Bore Hoses (LBHs), high-pressure hoses (up to 75 bar) used in amongst others the petrochemical and mining industries.

Traditionally these hoses have been manufactured in a manual labour-intensive process where layers of rubber and reinforcing cords are applied manually on a slowly-rotating mandrel in a basic filament winding process. Lack of control and accuracy in cord placement results in a product with lower material efficiency, and consequently a heavier design.

TANIQ reinvented the manufacturing process of cord-rubber products by applying advanced filament winding techniques. Through the use of a precisely-steered robot arm and rotating mandrel, the cord placement can be controlled more accurately compared to manual techniques. This allows for the products to be designed more efficiently by using less cord for the same performance. Furthermore, the increased accuracy results in improved quality (i.e. consistency in performance) of the products, challenging the traditional design safety factors used in the industry.

In recent years the design and manufacturing of the LBH family have been researched at TANIQ, developing the capabilities to create complex cord paths and run detailed Finite Element Analysis (FEA). Up until now designs have been optimised sporadically based on engineering judgement, resulting in impactful weight savings compared to the manual hose industry. However, a full-scale optimisation with the aim to reduce cord usage even further has not yet been performed. This can be achieved by tuning the winding parameters throughout the hose body, increasing the structural efficiency of the reinforcement layers and resulting in a design which satisfies safety requirements.

The objective of this thesis is to create an optimisation framework to minimise cord usage of a TANIQ's Large Bore Hose product, using an axisymmetric parametrised finite element model. The optimisation framework is to be integrated into TANIQ's design software, providing end-users with an optimised product.

[1] http://www.taniq.com/, 15/03/2019

The thesis work has two recurring themes. Firstly, a parametrised Finite Element (FE) model suitable for integration into the optimisation framework has to be developed. Currently, TANIQ uses a three-dimensional FE model where trusses are used to represent the exact cord placement in LBH designs. While the actual geometry of the structure is represented accurately, FE models generated using this method result in a large number of elements, slowing down analysis time. An alternative method is proposed, where the directional properties of the cords are smeared in the circumferential direction. This approach, named rebar (**re**inforcement **bar**) in ABAQUS, allows the LBH design to be reduced to the axisymmetric (two-dimensional) design space. Several studies have used rebar to perform both two- and three-dimensional FEAs on rubber tyres with cord reinforcements [1–3], showing good agreement with physical tests. Bolarinwa and Olatunbosun furthermore indicated a parametric rebar model showed "significant flexibility in being used as a tyre design sensitivity tool for optimizing design parameters" [1, p. 1257]. Also in the offshore industry ABAQUS's rebar method has been used in FEA of marine hoses, where Tonatto et al. [4–6] and Gao et al. [7] performed strength analyses of the central cylindrical sections.

Subsequently, using this parametrised FE model, an optimisation framework has to be set up to reduce cord usage in the LBH design. The aim is to perform a full-scale design optimisation where the influence of cord angle variation on the failure behaviour will be studied. The framework is to be integrated into TANIQ's proprietary design software, allowing clients to manufacture material-efficient LBHs. Structural design optimisation of composite structures using evolutionary algorithms increasingly becomes popular, where increasing computational resource availability allows FEA to be used in the design loop instead of analytical methods [8, 9]. Since FEAs can still be time consuming (e.g. with highly non-linear behaviour or a detailed mesh), it can be substituted using neural networks [10–12] or a surrogate model (e.g. the Design and Analysis of Computer Experiments (DACE) toolbox developed by Lophaven et al. [13]) [14–16].

TANIQ and its LBH product are discussed in Part I, covering the design principles and manufacturing of these cord-rubber mandrel-built hoses. Furthermore, the research proposal and scope are outlined based on literature and knowledge gaps identified in studies where the rebar approach is used to perform FEAs on cord-rubber pressure vessels.

Subsequently, the performance of the proposed rebar method is assessed in Part II. Firstly cord-rubber unit tests are studied to compare the baseline truss and proposed rebar methods on an elementary level. Secondly, a cylindrical pressure vessel with one reinforcement layer is studied, analogous to the research of Klute and Hannaford [17], ten Thije et al. [18] on McKibben artificial muscle actuators. The availability of test data allows both approaches to be compared to physical data. Finally, an FE model of a cord-rubber cylindrical pressure vessel with three reinforcement layers is developed, comparable to the work of Tonatto et al. The model will be parametrised to allow the cord angle to be specified throughout the structure, which allows the influence of angle variation on the deformation behaviour to be studied. A surrogate model using the DACE toolbox by Lophaven et al. is set up to assess Genetic Algorithm (GA) optimisation capabilities, where the maximum occurring strain at a given internal pressure is minimised.

The knowledge obtained from the studies of cord-rubber cylindrical pressure vessels is applied to create an FE model of the LBH product, whose geometry is based on an existing reference design. Part III covers the development of this parametric model and the subsequent generation of a data set, which will be used to create a DACE surrogate model. A parameter sensitivity study is performed on this data set, followed by GA optimisation on the surrogate model which aims to minimise the cord usage while satisfying a safety constraint.

Finally, the thesis is wrapped-up with a conclusion, summarising the outcome of this thesis and offering recommendations on topics that were identified as being of interest for future research.

I

Research Scope

2

TANIQ Large Bore Hose

The proposed MSc thesis is a research and development (R&D) project of TANIQ, a Rotterdam-based company specialised in the optimisation and automation of cord-rubber pressure vessel manufacturing. The company started as a spin-off of Delft University of Technology's Faculty of Aerospace Engineering in 2006, after which it continued to work closely with the Aerospace Structures and Materials department. TANIQ's mission is to "*provide solutions to manufacturers of (mandrel-built) reinforced rubber products, which enable them to improve their products and stay competitive in a global market*"[1].

One of their filament wound products is the Large Bore Hose (LBH), a high-pressure hose used in, amongst others, the offshore, petrochemical, and mining industries. Traditionally these hoses have been manufactured in a manual labour-intensive process where layers of rubber and reinforcing cords are applied manually on a slowly rotation mandrel in a basic filament winding process. Lack of control and accuracy in cord placement results in a product with lower material efficiency, and therefore a heavier design.

TANIQ reinvented the manufacturing process of cord-rubber products by applying advanced filament winding techniques. Through the use of a precisely steered robot arm and rotating mandrel, the cord placement can be performed more accurately compared to manual techniques. This allows for the products to be designed more efficiently by using less cord for the same performance.

In recent years, the design and manufacturing of the LBH family has been developed, having acquired the capabilities to create complex cord paths and run detailed Finite Element Analyses (FEAs). Up until now designs have improved sporadically based on engineering judgement, resulting in weight savings compared to the manual hose industry. However, a full-scale optimisation with the aim to reduce cord usage even further has not yet been performed. This can be achieved by tuning the winding parameters throughout the hose body, increasing the structural efficiency of the reinforcement layers and resulting in a design with equal strength but lower material requirements.

This chapter introduces the reader to the TANIQ hose product, of which the design optimisation will be the subject of the thesis. Section 2.1 describes the general design of the hose, Section 2.2 will discuss the materials being used, Section 2.3 gives an overview of filament winding with a focus on the winding angle and stacking sequence. Section 2.4 describes the general manufacturing process of the LBH product, Section 2.5 discusses possible failure modes, and finally Section 2.6 presents the reference hose design which will serve as a baseline for the design optimisation.

[1] http://www.taniq.com/, 12/07/2019

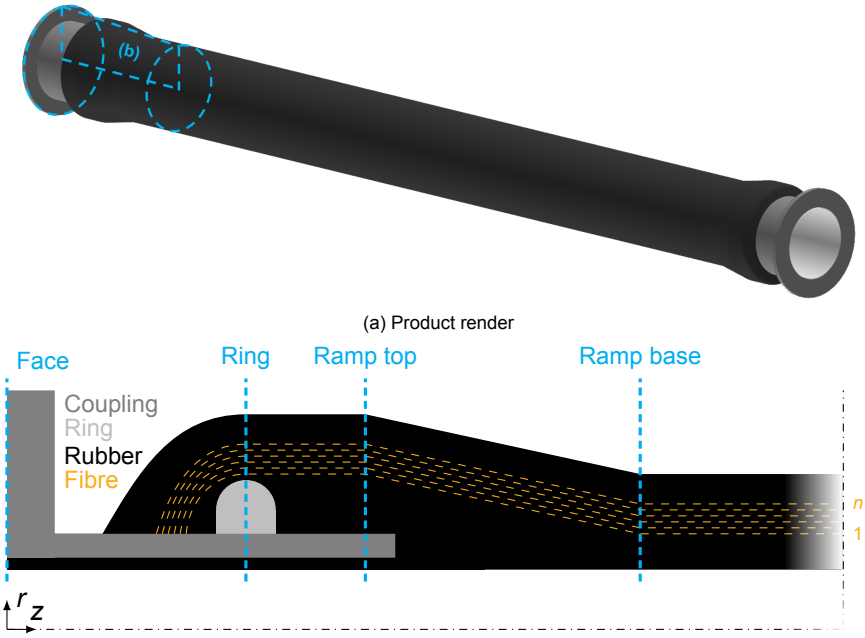

(a) Product render

(b) Axisymmetric sketch

Figure 2.1: TANIQ Large Bore Hose

2.1. General design

TANIQ LBHs exist of two major elements: the couplings and the hose body. The couplings are the end points of the hoses which serve as rigid attachment points, as well as retainers for the cords during the filament winding process. The hose body is the flexible cylindrical part between the couplings that allows the high pressure transfer of its contents. Figure 2.1 shows a design render of a LBH and an axisymmetric sketch of the coupling region.

2.1.1. Couplings

The couplings, indicated in Figure 2.1, are metal parts that serve as mechanical connectors for the hose. In general the geometry of these couplings are provided by the client, and do not make part of the hose design variables. Figure 2.2 shows an axisymmetric drawing of the coupling region of the reference hose design. One retainer ring is mounted on the shaft at 300 mm from the outer face, resulting in a coupling extension of 100 mm.

The retainer ring, around which the cords are turned during the winding process, should be sufficiently high to allow cord build-up to happen while preventing the outer cord layers to slip off the ring when the hose is pressurised. The axial position of this retainer ring influences the pressure load introduction, where van der Linden [19] argued that it should be positioned such that a section of the cylindrical part extends towards the hose body. This shifts the load introduction and resulting radial displacement away from the ring, and thus decreases the risk of cords being lifted off the retainer ring.

Furthermore the coupling has an inner rubber liner to prevent peeling at the load introduction points, by redistributing the load transfer on the metal-rubber adhesive interface as shear traction (instead of normal traction on the right edge of the coupling in the absence of an inner liner).

2.1.2. Hose body

The hose body is the cylindrical section that connects both end couplings. Thanks to its flexible nature, it can be used to connect couplings which are not aligned or have certain degrees of freedom. In operation the LBH are subjected to a high internal pressure, with past products being designed for burst pressures up to 75 bar (1.5 times the nominal working pressure).

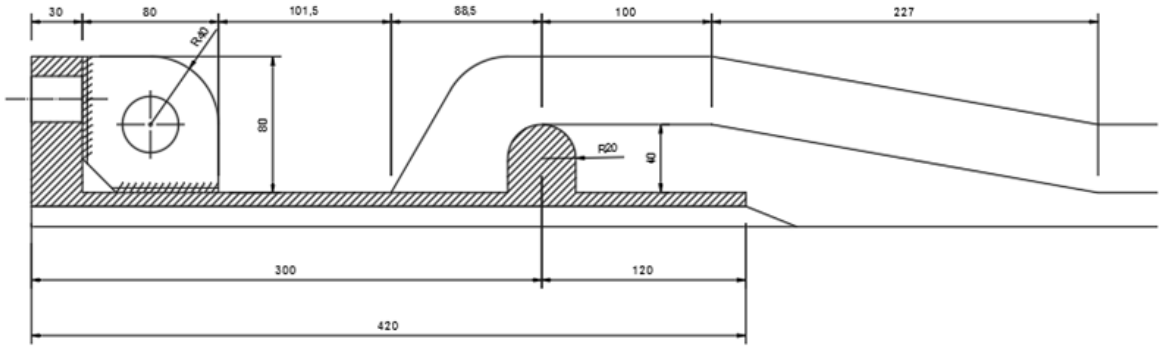

Figure 2.2: Reference hose coupling dimensions

The hose body is made out of cord-rubber composite, which is vulcanised in an autoclave at the end of its production process. Towards the couplings, a rubber ramp increases the winding profile diameter to align the cord layers radially with the reinforcement ring to allow proper winding of the cords around the rings (see Figure 2.1b).

The winding angle of the cord reinforcement layers can be varied along the length of the hose. The variability in winding angle allows for more specific tailoring of (local) hose strength and deformation behaviour. Currently in TANIQ's designs these angles are varied linearly on the ramp and kept constant elsewhere (except behind the rings, where the cords are turned around). The winding angle in the hose body of the reference design is [redacted], on which more details can be found in Section 2.6.

2.2. Materials

As mentioned already, the LBH is made from rubber reinforced with continuous cords. This section discusses the materials currently used by TANIQ during prototype manufacturing. The mechanical behaviour of cord-rubber differs from classic composites (e.g. CFRP or GFRP) due to the high elasticity of rubber compared to thermosetting resin[2]. Rubber is an elastomer, a family of polymers that have the ability to achieve strains in the order of 500 % [20, p. 511]. Because of the high elasticity, cord-rubber composites are very flexible with the stiffness in cord direction being more than three orders of magnitude larger than the elastic modulus perpendicular to them [21, p. 830]. To ensure proper modelling of the constitutive behaviour of this composite material it is important to understand the mechanical response of both components.

2.2.1. Rubber

TANIQ uses natural rubber as base compound for the rubber used in the production of their LBHs. The rubber is vulcanised to crosslink the polymer chains, which gives the elastomer its unique elastic properties. Vulcanisation is the process where rubber polymers are crosslinked with the help of additives at elevated temperature, which will form covalent bonds with unsaturated methine groups. After vulcanisation the rubber polymers are bonded to each other at previously unsaturated locations, resulting in a highly elastic material.

In its original state the material is amorphous, where polymer molecules are oriented randomly [20, p. 512]. The theory of hyperelasticity considers the strain energy density functions, which relates the elastic material response to the deformation gradient [22, 23]:

$$W = f(I_1, I_2, I_3) \quad \text{with} \quad \begin{cases} I_1 = \operatorname{tr}(\boldsymbol{C}) & = \lambda_1^2 + \lambda_2^2 + \lambda_3^2 \\ I_2 = \frac{1}{2}\left[\operatorname{tr}(\boldsymbol{C})^2 - \operatorname{tr}(\boldsymbol{C}^2)\right] & = \lambda_1^2\lambda_2^2 + \lambda_2^2\lambda_3^2 + \lambda_3^2\lambda_1^2 \\ I_3 = \det(\boldsymbol{C}) & = \lambda_1^2\lambda_2^2\lambda_3^2 \end{cases} \tag{2.1}$$

[2]Young's modulus of rubber: 0.01 GPa to 0.1 GPa, epoxy: 2 GPa to 3 GPa;
https://www.engineeringtoolbox.com/young-modulus-d_417.html, accessed: 2019-12-16

where W is the strain energy density, I_i are the fundamental invariants of the Cauchy-Green strain tensor $\boldsymbol{C}$, and λ_i the principal stretches along the orthogonal axes. In almost all studies referenced in this literature study, rubber is assumed to be isotropic, hyperelastic, and nearly incompressible. The incompressibility is expressed by keeping element volume unchanged after deformation:

$$\frac{\mathrm{d}V}{\mathrm{d}V_0} = \lambda_1\lambda_2\lambda_3 = 1 \quad \text{thus} \quad I_3 = 1, \quad I_2 = \lambda_1^{-2} + \lambda_2^{-2} + \lambda_3^{-2} \tag{2.2}$$

Several material models have been proposed to represent the constitutive behaviour of the rubber matrix. The most commonly used models based on the energy density function are discussed below.

Mooney-Rivlin model
Rivlin [24] continued upon Mooney [25]'s proposed model of the strain energy density as a function of the first two deformation invariants by turning it into a polynomial series:

$$W = \sum_{m,n=0}^{\infty} C_{mn}\left(I_1 - 3\right)^m \left(I_2 - 3\right)^n \quad \text{with} \quad C_{00} = 0 \tag{2.3}$$

where C_{mn} are material parameters. In its most general form (two terms) the function shows a linear relationship between stress and strain in simple shear:

$$W = C_{10}\left(I_1 - 3\right) + C_{01}\left(I_2 - 3\right) \tag{2.4}$$

The stress-strain relations for uniaxial tension and simple shear are given in Equation (2.5). The tensile relation is observed to be linearly dependent on uniaxial extension, whereas the shear relation is independent of simple shear deformation, resulting in a constant shear modulus, which is stiffer compared to test results [26, p. 759].

$$\frac{\sigma}{\lambda - \lambda^{-2}} = 2\left(\frac{\partial W}{\partial I_1} + \frac{1}{\lambda}\frac{\partial W}{\partial I_2}\right) = 2\left(C_{10} + \frac{C_{01}}{\lambda}\right), \quad \frac{\tau}{\gamma} = 2\left(\frac{\partial W}{\partial I_1} + \frac{\partial W}{\partial I_2}\right) = 2\left(C_{10} + C_{01}\right) \tag{2.5}$$

Ali et al. [22] found a very poor fit for the Mooney-Rivlin model to his test data, whereas Kondé et al. [3] determined that the model was only satisfactory up to 50 % uniaxial strain. This is often sufficient for tire analysis, where strains rarely exceed 20 % [27, p. 1222], but could return inaccurate results in the LBH analysis. Due to its simplicity (only two I_i terms, no powers) the model is computationally very efficient. Increasing the amount of higher order terms considered will decrease the efficiency while giving only a "marginally better fit" [23, p. 569].

Ogden model
Instead of using the Cauchy-Green strain tensor invariants I_i, Ogden [23] proposed to model W in terms of the principal stretches λ_i:

$$W = \sum_{n=1}^{N} \frac{\mu_n}{\alpha_n}\left(\lambda_1^{\alpha_n} + \lambda_2^{\alpha_n} + \lambda_3^{\alpha_n} - 3\right) \quad \text{with} \quad \alpha\mu > 0, \quad \alpha, \mu \in \mathbb{R}_0 \tag{2.6}$$

The model consists of terms with parameter pair (α,μ), with additional terms increasing the strain range of the model. Ogden showed good correlation with test data obtained from simple tension, pure shear, and equibiaxial tension tests.

Table 2.1 shows the stretch range λ in which the Ogden model is accurate depending on the amount of terms N used. An interesting property of the model is that the parameter pairs can be calibrated on data from any of these tests, and accurately model the other deformations as well. A single-term model has an accuracy up to $\lambda < 2$, where a second term will greatly increase the accuracy of simple tension and shear, but a third term is needed to enhance the equibiaxial tension response (and therefore the usable range of the model).

Table 2.1: Ogden model accurate stretch range in function of terms used [23, p. 574–577]

N	Simple Tension	Pure Shear	Equibiaxial Tension	Usable Range
1	$\lambda < 2$	$\lambda < 2$	$\lambda < 2$	$\lambda < 2$
2	$\lambda < 6$	$\lambda < 5$	$\lambda < 2$	$\lambda < 2$
3	$\lambda < 6$	$\lambda < 5$	$\lambda < 4$	$\lambda < 4$

Ali et al. [22], Phromjan and Suvanjumrat [28], Marckmann and Verron [29] concluded in their comparative studies that the Ogden model is a very accurate model in general, but can become computationally less efficient with increasing N if considering large deformations.

2.2.2. Reinforcing cords

Whereas the rubber provides flexibility and isotropic elasticity, the cords serve as anisotropic reinforcements which will define the strength of the LBH. As in classic composite materials, the presence of cords will greatly increase the stiffness in cord direction. The cord orientation determines the structural response of the LBH, as discussed in Section 2.1.

A wide variety of reinforcement cords are available, differing in ultimate tensile strength and strain, elasticity, density, etc. TANIQ currently uses Polyethylene Terephthalate (PET) cords for design and testing, because their high failure strain (11 %) compared to high strength cords increases the hose's flexibility [4]. Gao et al. found that the hose stiffness is dominated by the cord tensile stiffness, where different rubbers with stiffness values ranging from ±0.75 GPa to ±4 GPa resulted in a radial and axial stiffness variation of 27 % and 11 % respectively [7, Fig. 10/24/26].

Cords used in filament winding can either be dry or wet, where the latter are drawn through a resin bath in classic composite manufacturing [30]. The polymer molecules in synthetic cords have low polarity and reactivity, making direct bonding between the cords and rubber difficult. To improve adhesion and load transfer between these two, the cords are coated with Resorcinol Formaldehyde Latex (RFL) adhesive [31, p. 263–264]. In some cases, albeit more expensive, the cords have an additional rubber coating which increases the friction (see Section 2.3.3) and improves impregnation of cord layers with a dense coverage.

2.2.3. Wrapping Tape

A third material used in manufacturing of the LBH product is nylon wrapping tape. This tape is wrapped with high tension after application of each rubber layer. The tension results in the underlying rubber layer to be squeezed on the mandrel, increasing impregnation of the covered cord layers and removing air bubbles. After a certain waiting time the wrapping tape is removed and rolled onto its original spool by the robot. This allows the nylon tape to be reused multiple times in the manufacturing of a LBH, reducing material waste. The wrapping tape on the outer rubber layer remains applied until after vulcanisation of the product in an autoclave, where the nylon will apply radial compression due to shrinkage under elevated temperature.

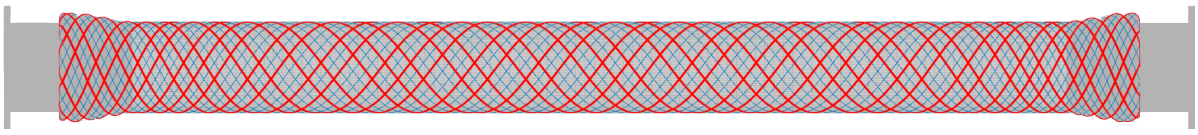

Figure 2.3: Cord pattern and repetition on a LBH profile

2.3. Filament winding

Filament winding is a manufacturing process where continuous cords (filaments) are applied on a rotating mandrel until a sufficiently repeating coverage is achieved (winding). It has been researched since the 1970's for the manufacturing of composite pressure vessels [32]. It allows for more accurate cord placement, higher cord volume fractions, and a more constant product quality compared to manual approaches (e.g. hand lay-up).

The technology has been adopted by TANIQ for the manufacturing of axisymmetric cord-rubber products, where process automation allows for higher cord placement accuracy, increased structural efficiency, and reduced manufacturing time. The addition of a six-axis robotic arm allows for more flexible process control and design liberties.

Koussios covers the fundamentals of filament winding theory in his PhD thesis *Filament Winding. A Unified Approach* [30]. This section will briefly discuss the basics, however for more information the reader is referred to this document.

2.3.1. Coordinate system

A cylindrical coordinate system is used in the design and analysis of mandrel-built cord-rubber structures. The *z*-axis, the axial coordinate, is positive along the longitudinal axis of the mandrel as indicated in Figure 2.1b. The *r*-axis, the radial coordinate, is perpendicular to the *z*-axis and is positive radially outwards. The angle φ, the azimuth or hoop coordinate, is measured positive counter-clockwise around the *z*-axis and perpendicular to the *r*-axis. The coordinate systems used in ABAQUS are shown in Table 2.2, with respect to the cylincrical baseline.

Table 2.2: Definition of coordinate systems

Cylindrical	**ABAQUS**		
	Axisymmetric	3D (default)	3D (cylindrical)
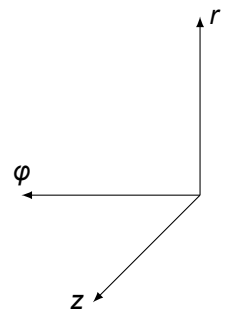	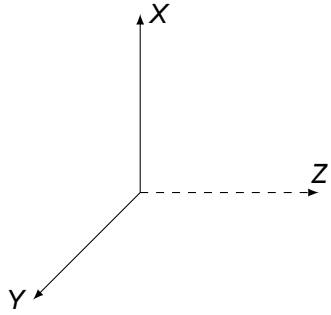	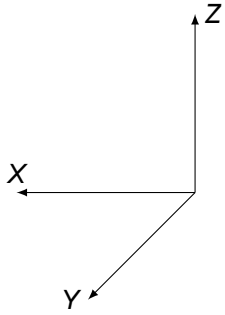	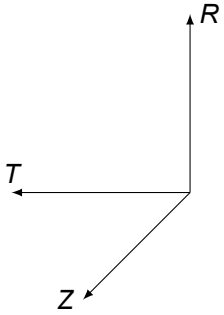

2.3.2. Winding angle

The winding angle α is defined as the counter-clockwise positive angle from the *z*-direction in a plane tangent to the shell of revolution (perpendicular to the *r*-direction). It ranges from 0° to ±90°, aligned with axial and hoop direction respectively. The winding angle determines both the deformation behaviour and strength of the hose, where its value relative to the neutral winding angle α_n is of importance. This is the angle of the principal stress direction in a cylindrical pressure vessel.

In thin walled pressure vessel theory, the hoop to axial stress ratio is $\sigma_h / \sigma_a = 2$ [33]. The angle α_n the cords should have to experience only tensile stress σ_f can be derived to be 54.7°:

$$\left.\begin{aligned} \sigma_h &= \sigma_f \sin^2 \alpha_n \\ \sigma_a &= \sigma_f \cos^2 \alpha_n \end{aligned}\right\} \frac{\sigma_h}{\sigma_a} = 2 = \tan^2 \alpha_n \quad \Rightarrow \quad \alpha_n = 54.7\,^\circ \tag{2.7}$$

Grove [33] described the effect of the winding angle on the initial deformation behaviour: imagine a cylinder with radius r, circumference s and length L, made of inextensible cords of unit-length (such that $L = \cos\alpha$ and $s = \pi d = \sin\alpha$). Figure 2.4 shows a sketch of the *unzipped* cylinder. The volume of this cylinder is then given by Equation (2.8).

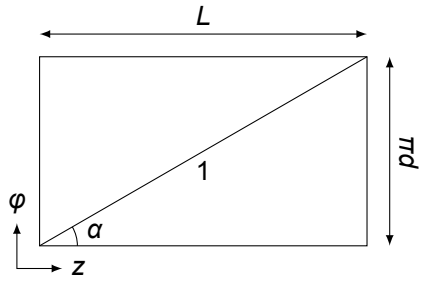

$$\left.\begin{array}{l} r = \frac{\sin\alpha}{2\pi} \\ L = \cos\alpha \end{array}\right\} \; V = \pi r^2 L = \frac{\sin^2\alpha\cos\alpha}{4\pi} \tag{2.8}$$

Figure 2.4: Unfolded cylinder with a cord length of 1 [33]

Taking α to range from 0° to 90° (axial and hoop direction respectively), the volume is 0 at the extreme bounds and maximum at $\mathrm{d}V/\mathrm{d}\alpha = 0$:

$$\frac{\mathrm{d}V}{\mathrm{d}\alpha} = \frac{\sin\alpha}{4\pi}\left(3\cos^2\alpha - 1\right) = 0 \quad \Rightarrow \quad \cos^2\alpha = \frac{1}{3} \quad \Leftrightarrow \quad \alpha_n = 54.7\,^\circ \tag{2.9}$$

Pressurisation deformation of cylinders with a winding angle different from α_n can be split in two phases: firstly the cylinder tends to maximise their volume by rotating the cords towards 54.7° (phase I), followed by cord elongation resulting in both radial and axial expansion of the cylinder (phase II).

The relation between winding angle and pressure vessel strength/deformation has been extensively researched over the past 30 years, both in single layer and multi-layer products [34]. Mertiny et al. [35] indicated that the optimal winding angle is dependent on the loading condition, of which the previously explained pressurised cylinder is an example.

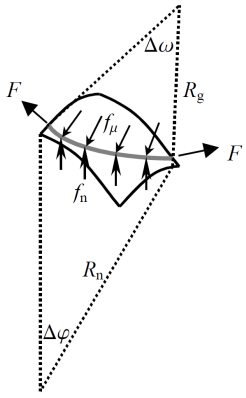

$$\mu \geq \left|\frac{f_\mu}{f_n}\right| = \left|\frac{R_n}{R_g}\right| \tag{2.10}$$

with $f_{\mu,n}$ Lateral, normal force per unit length
$R_{g,n}$ Geodesic, normal radius of curvature

Figure 2.5: Normal and geodesic radii of curvature describing a curved cord path [30, p. 75]

2.3.3. Friction winding

In filament winding cords are positioned on a rotating mandrel with a tensioning force (F in Figure 2.5) to ensure straight placement. If the cords are able to slide freely, they will always tend to follow the shortest path along a surface on so-called geodesic trajectories. In reality friction occurs between the cords and the underlying rubber layer, which allows for cord placement on non-geodesic trajectories. A sufficiently high friction μ will prevent the cords from slipping, with the cord placement stability criteria shown in Equation (2.10) [30]. As mentioned earlier, cords can be coated with rubber before application. These cords are more expensive but provide a higher friction coefficient and improved cord-rubber adhesion.

Figure 2.6 shows the cord placement on a dome and cylinder shape using a range of friction coefficients $\mu = \{-0.2, -0.1, 0, 0.1, 0.2\}$. The middle line, with $\mu = 0$, represents the geodesic path. The magnitude of the friction coefficient defines the axial angle change ($\mathrm{d}\alpha/\mathrm{d}z$), whereas the sign indicates whether the winding angle is increased or decreased. The friction coefficient can be obtained through winding tests, where the geodesic radius is decreased until the cord slips [30].

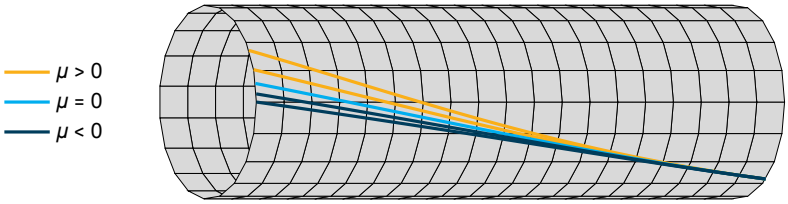

Figure 2.6: Cord placement on non-geodesic paths using friction winding

2.3.4. Winding path and pattern

The LBH has a cylindrical geometry, where the profile is axisymmetric around its central axis. As a cord is placed on the mandrel at a winding angle α, it follows a certain path around the hose profile. This path is repeated multiple times to form a winding pattern by turning the cord behind the ring, after which it is wound again on the cylindrical body.

Figure 2.3 indicates the winding pattern in red, which is the path a cord will follow until it reaches its starting position plus-minus a lead or lag angle. This pattern is subsequently repeated (with an angular shift with respect to the first loop) until sufficient cord coverage is achieved. Pattern identification is performed by search algorithms embedded in TANIQ's LBH Software, where possible cord architectures are proposed to the user.

The cord coverage c is measured at the axial centre of the LBH, which indicate how much of the circumference is covered by cords. It is dependent on the number of cords in a layer n_C, the winding angle α_F, the fcord diameter D_C, and the diameter of the cord layer profile D_L:

$$c = \frac{D_C n_C}{\pi D_L \cos\alpha} \tag{2.11}$$

2.3.5. TANIQ LBH Software software

TANIQ has developed its own filament winding toolbox: TANIQ LBH Software. The toolbox offers users a step-by-step approach to design, analyse, and produce customised LBH products. Firstly the user is required to define the hose geometry and layer architecture. Subsequently each layer has to be configured with a suitable winding pattern.

The TANIQ LBH Software and its LBH-specific version form the fundamental framework for product design. Because the outcome of this thesis is to be implemented into TANIQ LBH Software, the software will form the backbone of winding pattern and product geometry determination. The optimisation framework will make use of the TANIQ LBH Software to generate feasible designs.

2.4. Manufacturing

TANIQ's LBHs are manufactured in an automated production process, with minimal operator involvement. The machine consists of two elements: a rotating mandrel and a robotic arm. The mandrel is a cylindrical piece which will serve as the base for the winding process (rubber and cord placement). Its rotation speed is variable and computer controlled in coordination with the robotic arm, which is a six-axis robot. This allows it to have high flexibility, reducing winding process limitations and enabling both design and production improvement. The robotic arm is able to switch tools independently between application of the different material layers. The tools are capable of attaching and cutting the materials, reducing operator involvement and speeding up the manufacturing process.

2.4.1. Production process

LBHs are wound layer-by-layer on a rotating mandrel. As can be seen on Figure 2.1b the LBH consists of interchanging rubber and cord cord layers. The production process is discussed below:

1. **Mandrel preparation** The mandrel is the cylinder on which the LBH will be produced. It serves as a solid basis for application of the various material layers. A release agent is applied on the mandrel to allow removal from the interior after vulcanisation. The application quality is important to ensure detachment of the rubber from the mandrel without damaging the inner wear layer.
2. **Coupling positioning** The couplings have to be positioned on the mandrel corresponding with the required face-to-face length of the final product. Attention should be paid to ensure the coupling cross sections are perpendicular to the hose axis.
3. **Inner rubber layer** The inner rubber layer protects the inner cord layer from abrasion. Currently this layer is applied on the mandrel before the couplings are mounted. Ongoing research instead is looking to adhere the rubber to the inside of the coupling before mounting. This would result in more accurate positioning and improve the bond quality between the rubber and coupling. Another important function of the inner rubber layer is to shape the initial cord winding surface. As can be seen in Figure 2.1b it reaches the top of the retainer ring and ramps down towards the hose body.
4. **Cord reinforcement layer** The reinforcing cords ensure the structural integrity of the LBH. They are placed on the patterns generated according to the theory explained in Section 2.3. The robot head developed by TANIQ is capable of placing multiple filaments in parallel, reducing the amount of cycles required by the robot arm and thus speeding up the manufacturing process. The cords have to be attached and cut manually before and after winding. An operator will stick the cord to the underlying layer using rubber tape. In order to place (and keep) the cords at their intended paths, they are tensioned lightly (±3 N) during the winding process.
5. **Interply rubber layer** A rubber layer is added after each reinforcing cord layer to improve adhesion of the reinforcement layers. The material is softer than the inner and outer layer, allowing it to flow more freely. The rubber layer is applied through hoop winding. Layer thickness is controlled by tensioning (stretching) and overlap.
6. **Wrapping** Following the application of a interply rubber layer, a nylon tape is temporarily wrapped around the LBH. It is hoop wound under tension to apply compressive stress on the rubber layers, which ensures that the no air is entrapped in the product. Subsequently the nylon wrapping tape is unrolled back onto its spool to be reused throughout the manufacturing process, resulting in no material waste.
7. **Additional cord reinforcement layers** Repeat steps **4 – 6** until all cord reinforcement layers are applied.
8. **Outer rubber layer** Similar to the inner rubber layer, the outer one protects the outermost cord layer from environmental hazards. The thickness is specified by the customer.
9. **Autoclave wrapping** The nylon tape is applied on the outer rubber layer for vulcanisation in the autoclave. It shrinks during process due to the elevated temperature, which maintains compressive pressure on the LBH. The wrapping should fully encompass the product, to prevent rubber flow and sagging [36, p. 740].

2.4.2. Manufacturing defects

Manufacturing quality has a direct relation to product performance. TANIQ has identified several manufacturing defects that can occur, with the production process being continuously improved to reduce the likelihood of these defects to occur.

The main defects are related to uneven distribution of matrix and cords:

- **Voids** The absence of both rubber and cords in the product are called voids. These empty spaces do not carry loads and cause local stress concentrations, decreasing the strength of the composite laminate [37].
- **Rubber rich areas** Cords can slip during winding due to insufficient friction or during wrapping because of matrix squeezing moving the cords. These rubber rich areas reduce the laminate strength and are prone to matrix cracking adjacent to the cords [38].
- **Wrapping tape folding** Majority of the wrapping is applied through hoop winding, however near the ends of the hose more complex helical winding is used. Sometimes wrap folding can occur, which could lead to insufficient product sealing resulting in rubber leakage during vulcanisation.

2.4.3. Limitations

The hose design is limited by the manufacturing process. The hose geometry is constrained by the machine dimensions: the reach of the robotic arm, maximum mandrel diameter, and autoclave dimensions. Limitations of the manufacturing process related to the winding robot (e.g. path feasibility, collision detection, etc.) will not be considered during this thesis. It is assumed that every design generated using TANIQ's design software is realisable.

2.5. Failure analysis

This section will encompass the failure behaviour of the LBH product. Three causes of failure are identified and covered: damaging of the cord layers after wear, fatigue failure due to cyclic loading, and mechanical failure. For the design process in this thesis only mechanical failure will be considered.The LBH's primary purpose is to transfer pressurised contents. Under pressurisation the hose body will expand radially and axially[3]. Often at least one of the two entities connected by the hose will be dynamic (e.g. ship-shore or ship-ship transfer), which will require the hose to be flexible. This will cause the hose to bend or extend depending on the relative movement of the couplings. The LBH sizing process considers the unpressurised axial tensile strength to be a design requirement, which is specified by the customer. This strength requirement is not taken into account in this thesis, but can be imposed as a design space constraint on future implementation of the optimisation framework. The lateral displacement is not considered, since pressurised hoses will not undergo large lateral displacements (due ot their increased bending stiffness).

Several prototypes have been tested by TANIQ where the purpose of these tests was to determine the burst pressure and deformation of the hoses, as well as identify the failure location and mode. Loss of structural integrity was determined to occur upon first cord failure during burst testing. This is consistent with results obtained by Tonatto et al. [5].

Determination of the layer failure sequence was not possible, but the inner layer was known to carry the highest loads. van der Linden [19] analysed recordings of a burst test and noticed failure to be abrupt, indicating that first cord failure was critical.

The rupture was located near the coupling section, which was deemed unacceptable due to safety requirements. Currently the hose body is intentionally designed to be weaker such that failure occurs towards (ideally the centre of) the hose body. The rupture location is one of the key design requirements, which will be of great importance in the optimisation process.

[3] Assuming the pressure magnitude results in phase II deformation.

2.6. Reference hose design

The purpose of this thesis is to optimise the LBH product, where the aim is to reduce cord usage in the product, which will decrease the manufacturing cost and time. One of the latest LBH design will be used as the reference and starting point of the optimisation process. It has an inner diameter of 406 mm and an end-to-end length of 6 m. The performance requirements used in the sizing were based on burst pressure and axial tensile strength. The hose is designed to withstand either 75 bar internal pressure or 54 tf of axial tensile force. Table 2.3 shows the material consumption of the reference hose design. It consumes about 366 kg of rubber and 60 kg (30.5 km) of PET cords. The material usage is measured in the axisymmetric coordinate system, where the cord length of the turn around zone is not considered.

Table 2.3: Reference hose material consumption

	Rubber		Cord	
Layer	**Volume** [dm^3]	**Mass** [kg]	**Length** [m]	**Mass** [kg]
1	170.37	189.11	5491	10.70
2	11.26	12.50	5106	9.95
3	11.44	12.70	5114	9.96
4	11.63	12.91	5074	9.89
5	11.81	13.11	4738	9.23
6	11.99	13.31	5024	9.79
7	100.88	111.98		
Total	329.39	365.93	30 547	59.52

The cord layer design is shown in Table 2.4. The cord angle distribution is the result of an iterative design optimisation performed in cooperation with a client. As can be seen the angle is kept constant through the thickness in the hose body, and both along the length and through the thickness over the ramp. This layer build-up is the result of a series of manual iterations, where the strength of several designs with angle variations were compared. The amount of reinforcing layers and their cord coverage drives the material usage of the entire products, as it is directly related to the total cord length and rubber usage.

Table 2.4: Reference hose cord layers angles, diameter, and cord coverage at indicated locations

		Body			Ramp base			Ramp top		
Layer	**Cord amount**	**Angle** [deg]	**Diam.** [mm]	**Cover.** [%]	**Angle** [deg]	**Diam.** [mm]	**Cover.** [%]	**Angle** [deg]	**Diam.** [mm]	**Cover.** [%]
1	544	[redacted]	449	126	[redacted]	449	170	[redacted]	540	165
2	512	[redacted]	455	116	[redacted]	455	156	[redacted]	548	139
3	512	[redacted]	461	115	[redacted]	461	156	[redacted]	555	126
4	512	[redacted]	468	114	[redacted]	468	154	[redacted]	561	115
5	480	[redacted]	474	105	[redacted]	474	142	[redacted]	567	100
6	512	[redacted]	480	111	[redacted]	480	150	[redacted]	573	99

3

Research Proposal & Outline

The thesis work can be split into two main work categories. On one hand a parametrised Finite Element (FE) model suitable for integration into the optimisation framework has to be developed. On the other hand, using this FE model, an optimisation framework has to be set up to minimise cord usage in the Large Bore Hose (LBH) design. The purpose of the framework is to be integrated in TANIQ's design software, allowing clients to manufacture material-efficient LBHs.

3.1. Finite element of cord-rubber composites

Finite Element Analysis (FEA) of cord-rubber composites has been studied in the tyre industry since the 1980's. Noor and Tanner [39] discussed various computational models for tyre deformation analysis. In early research cord-rubber structures were analysed through simple models using equivalent properties, cord-network models (which neglected the rubber), and anisotropic shell models taking a continuum mechanics approach.

Tabaddor [40] aimed at approximating cord-rubbers by a set of effective composite properties to enable application of the Classical Lamination Theory (CLT). Since the CLT assumes small deformations, Tabaddor concluded that its application to cord-rubber composites is limited due to the hyperelastic properties and significantly higher strain ratios of the rubber matrix. Also Cembrola and Dudek [21] came to this conclusion, since many assumptions of the CLT do not apply to cord-rubber laminates.

3.1.1. Embedded elements in ABAQUS

ABAQUS allows for elements to be embedded in host elements. The positions of the embedded nodes are geometrically constrained respective to the host elements, while having their translational degrees of freedom eliminated. This ensures that the embedded nodes stay in the same relative position in the host elements upon deformation of the latter, while the stiffness of the former is added to the model. [41]

The work in this thesis will embed truss or surface with rebar properties elements into solid rubber host elements (see Sections 3.1.2 and 3.1.3). Both embedded element types only have stiffness in axial direction (in rebar surfaces through smeared properties along a specified orientation).

3.1.2. TANIQ's approach: truss method

TANIQ uses ABAQUS, FEA software developed by Dassault Systèmes, for their design sizing. ABAQUS is widely used in the academic and industrial world due to its customisability and accurate simulation capabilities of non-linear physical behaviour. It is used frequently in recent cord-rubber FEA studies [3–7, 19, 42]. Modern FEA of cord-rubbers in the tyre and hose industries are based on the separate modelling of the cords and rubber matrix, where the former are embedded in hybrid solid elements.

Currently the LBH product is modelled by TANIQ using truss elements (T3D2) embedded in hybrid solid rubber elements (C3D8H). This method has been developed and implemented by Davids [42], who based his work on research performed by Reese [43] and Sharma and Sutcliffe [44]. This work has been continued upon by van der Linden [19] and TANIQ engineers.

3.1.3. Proposed approach: rebar method

An alternative method to model cord-rubbers in ABAQUS is through the use of rebar-elements. These surface elements represent the reinforcing cord layers with a certain angle, area, spacing, and material. They add anisotropic stiffness to the host elements in which they are embedded. The implementation in ABAQUS is based on work performed by Helnwein et al. [45], who developed a rebar implementation in MARC FE for cord-rubber analysis (automobile tyres) in 1993. He expressed advantages compared to the truss method, amongst which an increased computational efficiency and a greater meshing flexibility because rebar elements share its host element's nodes without introducing additional degrees of freedom. These advantages, combined with the elimination of a dimension in axisymmetric modelling, make that FE analyses using ABAQUS's rebar method promise to be faster than their truss method counterparts. This method has increased in popularity over the past decade to study deformation of tyres and hoses.

Bolarinwa and Olatunbosun [1] performed a numerical burst analysis and parametric sensitivity study using an axisymmetric rebar-based tyre model. He found the calculated burst pressure to be of the same magnitude as test results of similar tyres. Behroozi et al. [2] also performed an axisymmetric tyre burst pressure analysis using rebar elements, which was validated by deformation comparison with physical inflation tests. Kondé et al. [3] successfully used the rebar method to study an aircraft tyre, stating the axisymmetric rebar-based model to be much more accurate compared to continuum mechanics based anisotropic= and hyperelastic deformation models.

Tonatto et al. performed several analyses of offshore cord-rubber hoses. In their 2015 study [4] the deformation of a six-layer cylindrical tube due to internal pressure was analysed. In a 2017 study Tonatto et al. [5] studied multi-layered cord-rubber hoses with a steel helix using rebar elements for the reinforcement layers. The analysis used a 3D model constructed out of surface rebar elements. In their most recent study (2018), Tonatto et al. [6] expanded on their previous analysis of steel helix cord-rubber hoses, where 3D surface rebar elements were used to analyse non-axisymmetric deformation (torsion and bending). Gao et al. [7] followed-up on Tonatto's work by performing a similar analysis on a cord-rubber hose with steel helix. It was focussed on assessing the effect of rubber and cord properties on the hose's deformation under axial tension and internal pressure.

The aforementioned studies show the feasibility of using ABAQUS's rebar implementation to analyse cord-rubber structures. It is, however, important to note that both Tonatto et al. [4, 5, 6] and Gao et al. [7] used cylindrical models for their analysis with a constant winding angle per layer stack. Furthermore these studies only considered the hose body, neglecting the coupling regions. Currently (published) multi-layered analyses in the industry do not cover angle variation along the axial direction. The effect of angle variation on the deformation shape and load distribution in the LBH will have to be studied in order to allow reduction of cord usage.

3.2. Large Bore Hose cord usage reduction

The anisotropic properties of composite materials can be used to increase the structural efficiency of composite structure by aligning the cords with the principal stress orientation. The relation between winding angle and pressure vessel strength/deformation has been extensively researched over the past 30 years, both in single layer and multi-layer products [4, 33–35, 46, 47].

These studies indicate that the structural efficiency of the LBH can be increased through tailoring of the winding angle in the different reinforcement layers. As a result the amount of cord material necessary can be reduced, which is the goal of this research project. Since the LBH is not an ideal thin-walled cylindrical pressure vessel, the optimal winding angle will vary with radial and axial position. Figure 2.3 shows the cord paths of an existing hose design, where the winding angle is larger near the end couplings. This adds stiffness in hoop direction to limit radial expansion. The axial variation of the fibre angle is possible due to TANIQ's innovative cord winding technology, which uses the friction between rubber and cord to realise non-geodesic paths [30].

3.2.1. Multilayer winding angle optimisation

Tonatto et al. [4, 5, 6] and Gao et al. [7] considered single-angle stacks in their FE studies of cord-rubber hoses, where layer stacks with different winding angles were separated by hoop reinforcements or a considerable amount of rubber. The studies did not analyse the interlaminar shear due to adjacent layers having different winding angles (and thus deformation upon inflation). Gurvich [48] noted that the thickness of interlaminar rubber layers affect the shear stiffness of the cord-rubber composite.

Xing et al. [47] analysed the effect of stacking sequence on cord stress distribution in carbon cord epoxy filament wound tubes. Winding with a constant angle through the thickness leads to an uneven cord loading, with the inner cord layer carrying a higher stress. A uniform stress distribution over the layers was achieved by increasing the winding angle radially outwards towards the neutral angle, consistent with van der Linden's [19] findings. A uniform stress distribution results in an increased structural efficiency, since all material is loaded equally. The effect of the neutral angle on the stress distribution in multilayer pressure vessels was not identified in this study, but could prove useful in optimising the winding angles in the LBH. Mertiny et al. analysed the sensitivity of the σ_h/σ_a failure envelope to the inner layer winding angle [46] or stacking sequence [35]. An important conclusion is that multi-angle filament winding allows for structural optimisation taking into account multiple loading scenarios.

During the literature study no research papers on axial variation of the winding angle were found. This can be because the robots to accurately control the cord placement is still an emerging technology. It does, however, open up opportunities to increase the structural efficiency.

3.2.2. Optimisation algorithm

There exist two main categories of optimisation algorithms: gradient based and evolutionary. A gradient based approach evaluates the gradients surrounding the current point and determines the next point in the sequence. Such methods tend to be quite efficient, but have difficulties with discrete variables and easily tend to converge on a local extreme. Evolutionary algorithms are stochastic global search methods, where contrarily to gradient based methods a population of points is considered at each iteration. These algorithms tend to mimic natural behaviour of populations, often based on observations of the animal kingdom.

The Genetic Algorithm (GA) is an evolutionary algorithm widely used in structural optimisation problems. It is a versatile method to optimise the stacking sequence in composites, due to its robustness and resilience towards local minima. Examples are the optimisation of composite structures by Bisagni and Lanzi [10], Pirrera et al. [49], Fu et al. [50], Wang et al. [51], and Maes et al. [9] where GAs were used to find the lightest design within a highly non-linear and heavily constrained design space. Fu et al. [50] combined the use of GA with a response surface, which decreased the optimisation time to within an acceptable time span due to the high computational FEA requirements.

No works have been found on the design optimisation of cord-rubber composite structures. In the offshore hose industry TANIQ is one of the first to offer automated filament winding production of high-pressure hoses, where the lack of design flexibility and process control in manual manufacturing suppressed optimisation opportunities. The weight optimisation of a cord-rubber hose is an unexplored topic that can reduce the environmental impact and increase the product's sustainability by decreasing the footprint of the manufacturing process.

3.3. Research question, aims and objectives

The previous section discussed the state of the art of past research on the FEA of cord-rubber composite pressure vessels. It highlighted their usefulness and shortcomings towards the proposed research project. This section poses research questions as to find an answer to the knowledge gaps identified between the existing literature and research objective.

This thesis aims to find the most optimal winding configuration that results in the highest structural efficiency and thus lowest cord usage. The research objective can therefore be stated as:

To minimise cord usage of a Large Bore Hose product by optimising the winding configuration within an acceptable computational time.

There are two main research questions in this MSc thesis, which originate from the goal to find an optimal winding configuration of a LBH to minimise cord usage. As a top-level requirement, TANIQ wants the optimisation to be performed within a time span of 24 h. This means that, as part of the optimisation project, in order to reduce the run time a faster FEA approach (identified as ABAQUS's rebar method) should be investigated.

The main research questions can be divided into several subquestions which touch the different aspects of the research project. As stated before, two main focus areas exist: firstly the rebar method is investigated as an alternative FE model approach in order to reduce FEA time such that the optimisation can be performed in a *reasonable* time span, secondly the winding angle configuration of the LBH will be optimised through the use of FEA. The cord usage reduction in LBH products will positively affect the sustainability by reducing the resource requirements and decreasing the supply chain's carbon footprint.

1. **Can an FE model be created to determine the burst pressure of a cord-rubber Large Bore Hose using ABAQUS's rebar method?**

   (a) How does the rebar method compare to the truss method (i.e. verification)?
   (b) What is the relation between burst pressure, failure ratio, and cord usage?
   (c) How much computational time is saved using the rebar method over the truss method?

   This research question investigates the possibility of using rebar to accurately model the structural response of a LBH when pressurised until failure. Tonatto et al. [4, 5, 6] and Gao et al. [7] successfully used rebar to model cylindrical multilayer cord-rubber hoses. Their studies, however, did not include the coupling regions and used a constant winding angle through the cylindrical hose body. The goal in this project is to create a rebar model of the entire LBH, including the coupling regions, and vary the angles both axially and radially.

   By putting FEA results of both rebar and truss models side by side, performance and computational requirements can be compared. Since the truss FE model has been implemented by Davids [42] and van der Linden [19], it can be used to verify the rebar FE model.

   Successful verification of a rebar LBH FE model will allow this method to be used for future development, strength analysis, and optimisation of the high-pressure cord-rubber multilayer hoses. Furthermore it would serve as a proof of concept for its application in FEA of other axisymmetric non-cylindrical cord-rubber structures.

2. **What winding angle configuration and amount of cord layers results in the highest structural efficiency for a given set of requirements?**

   (a) What effect does the neutral angle have on the stress distribution?
   (b) What effect does the neutral angle have on the deformation shape?
   (c) What effect does the neutral angle have on the failure location?
   (d) How many FEAs does the optimisation algorithm require to converge on the optimal configuration?

Following the feasibility assessment of rebar for the FE modelling of LBH products, this research question focusses on finding the configuration with the highest structural efficiency. One of the last client approved LBH designs will serve as the baseline to measure cord usage reduction. The reference design specifies both the geometry (coupling and hose dimensions) and performance requirements (burst pressure and minimal axial stiffness). One of the top-level client requirements is that failure should be ensured *not* to occur near the coupling. Since GA will be used in the optimisation, the failure location can be included in the fitness evaluation to heavily penalise designs that do not meet this requirement. The resulting axial winding variation will subsequently show insight on its influence over the (axial) failure location.

Apart from the economic benefit for TANIQ, this optimisation framework also improves the sustainability of Large Bore Hose products. The reduced (cord) material consumptions means a reduced carbon footprint of the supply chain (raw materials, processing, shipments), operational life (transportation), and end of life solution. Furthermore other TANIQ products show the opportunity to be optimised through application of the Optimisation Framework (OF).

3.4. Research hypotheses

With the research objective and questions defined in the previous section, the expected outcomes of the research should be discussed as well. These outcomes are stated below in the form of hypotheses which are to be tested. A quantitative approach is taken, where FEA is used to generate data.

1. Rebar elements can be used to create an axisymmetric FE model of the LBH with the same accuracy as the current truss-approach at TANIQ.
2. The burst failure location can be manipulated through radial and axial variation of the winding angles.
3. Cord usage of a LBH can be reduced through optimisation of the winding parameters.

The rebar function in ABAQUS models anisotropic reinforcements in host elements by assuming a smeared layer with directional stiffness. This approach is recommended to simulate structures with embedded directional reinforcements, such as steel-reinforced concrete and cord-reinforced tires [41]. Tonatto et al. [4, 5, 6] and Gao et al. [7] used rebar to simulate the cylindrical sections of cord-rubber hoses and found good correlation with physical tests. Since these studies do not incorporate the couplings nor considered angle variations, a bottoms up research methodology is taken.

II

Cylindrical Cord-rubber Pressure Vessels

4

Cord-rubber Unit Tests in Finite Element

The cord reinforcements in cord-rubber composites add directional stiffness to the otherwise highly elastic rubber. In Finite Element Analysis (FEA) of cord-rubber structures, two main approaches exist to model these directional reinforcements: through exact representation using truss elements, or through the use of a layer with smeared properties over the reinforcement plane.

In order to understand the similarities and differences between the aforementioned approaches, two basic tests are discussed in this chapter. Consider a rubber cube with sides of unit length, which has cord reinforcements on the *xy*-midplane (perpendicular to the *z*-axis). The rubber and cord material data is presented in Section 4.1. This cube is extended in *x*-direction, after which the force required for this stretch (i.e. the reaction force) is measured. Section 4.2 considers a unidirectional reinforcement layer, with the cords parallel to the *x*-axis. In Section 4.3 the reinforcement layer is a balanced angle ply, where the cords have a ±45° angle with the *x*-axis.

4.1. Material data

The cube material is rubber defined as a Mooney-Rivlin solid [24] (see Section 2.2.1), as used in the study of ten Thije et al. study on inflation deformation of a cord-rubber actuator [18].

$$W = 0.1184\left(\bar{I}_1 - 3\right) + 0.1057\left(\bar{I}_2 - 3\right) \qquad \text{[MPa]} \qquad \left| \begin{array}{l} \lambda_1\lambda_2\lambda_3 = 1 \\ I_1 = \lambda_1^2 + \lambda_2^2 + \lambda_3^2 \\ I_2 = \lambda_1^2\lambda_2^2 + \lambda_2^2\lambda_3^2 + \lambda_1^2\lambda_3^2 \end{array} \right. \tag{4.1}$$

The cord material, GRP-110-1-1/4, is a polyester braid defined by ten Thije et al. using the Nadai stress-strain curve model (Figure 4.1) [18]. This elastic-plastic material model specifies an initial linear elastic phase with a stiffness of 3.5 GPa, followed by gradual softening when exceeding the yield point (70 MPa at 2 % strain) [52, p. 186].

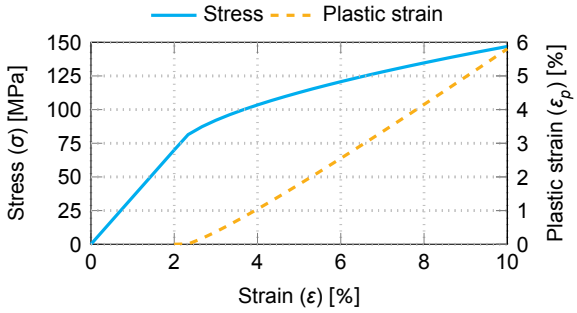

$$\sigma \le \sigma_y \;:\; \sigma = E\varepsilon \tag{4.2}$$

$$\sigma > \sigma_y \;:\; \sigma = \sigma_y + 350\left(\varepsilon - \varepsilon_y\right)^{0.6}$$

ε_y	Yield strain	0.02	–
σ_y	Yield stress	70	MPa
E	Young's modulus	3.5	GPa

Figure 4.1: Nadai stress-strain curve of GRP-110-1-1/4

4.2. Cube with longitudinal reinforcement

The first test compares two unit cubes with reinforcements on the *xy*-midplane, represented by rebar or truss elements respectively oriented in *x*-direction. The cubes are extended 10 % in *x*-direction (δL = 0.1 mm), where deformation in *y*-direction and *z*-direction is unconstrained. Figure 4.2 shows the unit cubes with rebar and truss reinforcements respectively. The cubes have sides of 1 mm. In total 10 cords are evenly distributed over the *xy*-midplane, resulting in a cord spacing of 0.1 mm. The cords are given a cross-sectional area of 0.001 mm^2, or a 35.7 µm diameter if assumed circular.

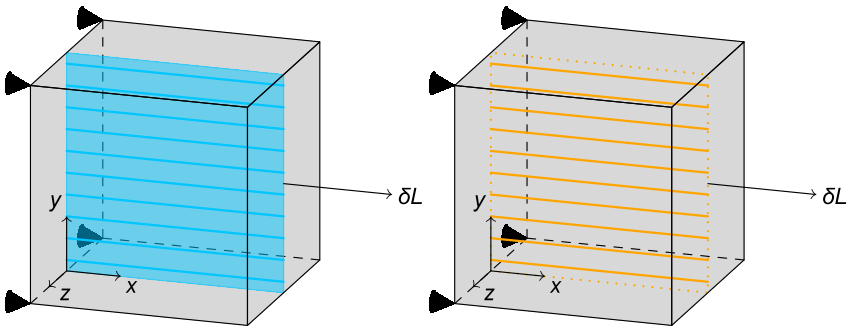

(a) Rebar specified on embedded surface (b) Trusses distributed over the plane

Figure 4.2: Unit cubes with reinforcements embedded on the mid plane

4.2.1. Finite element analysis

The Finite Element (FE) models of the cubes are created in ABAQUS 2018 as 3D deformable parts. The rubber is defined by `C3D8H`[1] elements. Herein `SFM3D4`[2] elements are embedded in the case of rebar (Figure 4.2a), or `T3D2`[3] elements in the truss case (Figure 4.2b). The FEAs were performed using elastic-plastic material data (as specified in Section 4.1), or hyperelastic material data. TIn the latter case, the stress-strain curve of Figure 4.1 is defined as uniaxial tensile test data using the Marlow material model.

Table 4.1: Mesh convergence analysis results

Elements		Elastic-plastic				Hyperelastic			
		Rebar		Truss		Rebar		Truss	
n_e	ρ_m	F_x [N]	ΔF_x [%]	F_x [N]	ΔF_x[%]	F_x [N]	ΔF_x [%]	F_x [N]	ΔF_x [%]
2	4	1.453		1.453		1.453		1.453	
3	9	1.453	0	1.453	0	1.453	0	1.453	0
4	16	1.453	0	1.453	0	1.453	0	1.453	0

A mesh convergence study was performed to ensure accuracy of the FE models, by monitoring the dependency of the reaction force F_x on the mesh density ρ_m (elements per unit area)[4]. With each step the amounts of elements in *x*-, *y*-, and *z*-directions are increased, such that the mesh density would be (approximately) doubled. Table 4.1 shows that increasing the mesh density did not cause a change in reaction force.

4.2.2. Results

The reaction force F_x measured after a 10 % stretch along the *x*-axis is 1.453 N for both the rebar and truss models (see Table 4.1). The true stress in the cords is measured as 146.9 MPa, consistent with Figure 4.1. The cord force in the rebar is 0.1336 N, in agreement with the measured true stress. No difference is observed between the elastic-plastic and hyperelastic analyses.

[1] Continuum three-dimensional 8-node linear brick with hybrid formulation
[2] Membrane-like three-dimensional 4-node linear surface
[3] Three-dimensional 2-node linear truss
[4] $\rho_m = n_e^2$, where n_e is the number of elements in any of the unit cube dimensions.

4.3. Cube with angled reinforcement

The second test is similar to the previous unit test, however in this test the reinforcements are placed at an angle instead of in x-direction. A pattern is created with the ±45° cords such that each intersection of the xy-midplane with the cube sides contains four evenly distributed crossover points. This will result in a cord spacing (between parallel cords) of 0.177 mm. The cords are given a cross-sectional area of 0.001 mm^2, or a 35.7 µm diameter if assumed circular.

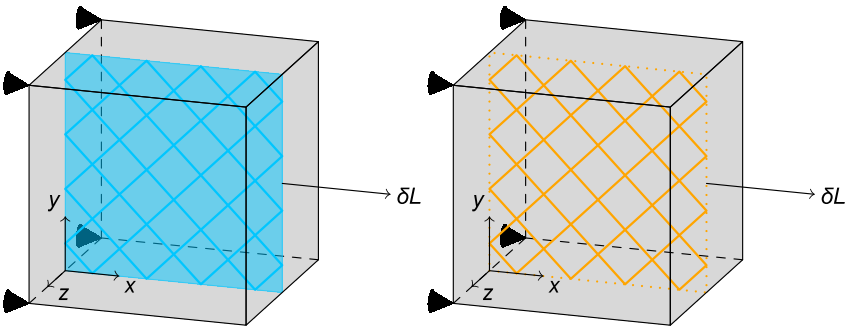

(a) Rebar specified on embedded surface (b) Trusses distributed over the plane

Figure 4.3: Unit cubes with reinforcements embedded on the mid plane

4.3.1. Finite element analysis

The FE models of the cubes are created in a similar way to the previous unit test, using rebar (Figure 4.3a) or truss (Figure 4.3b) elements to represent the cord reinforcements.

A mesh convergence study was performed to ensure accuracy of the FE models, by monitoring the dependency of the reaction force F_x on the mesh density ρ_m (elements per unit area). With each step the mesh density was approximately doubled. The models can be observed approach a reaction force of 0.141 N, however as a consequence of the model construction convergence was not achieved even with a fine mesh (n_e = 23, or 12 167 rubber elements). Since the cord tensile stiffness is significantly larger than the rubber tensile and shear moduli (3.5 GPa compared to 1.35 MPa and 0.45 MPa respectively)[5], pure shear deformation is dominant (i.e. contraction along the y-axis). With decreasing element size the cord-rubber cube representation becomes sensitive to local deformations, whereas the smeared properties of the rebar are embedded in all rubber elements. This can be seen in Figure 4.4 for both models.

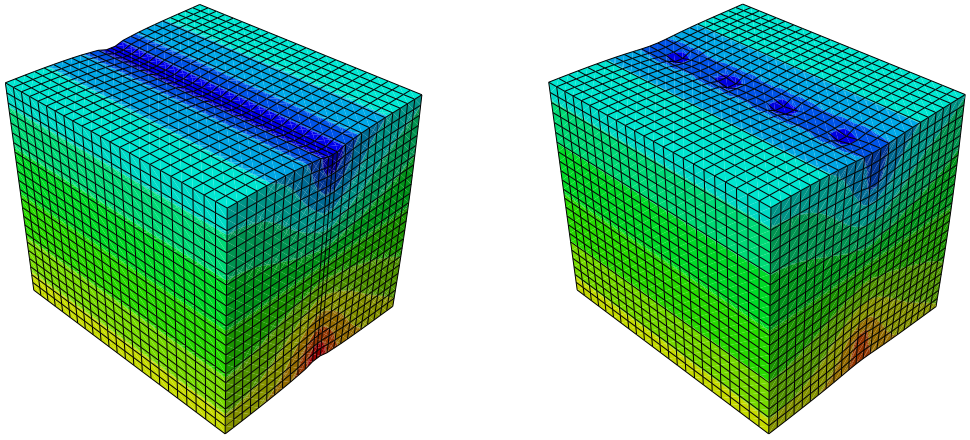

(a) Rebar model showing necking at the embedded surface edges (b) Truss model showing indents at crossover points on the outer surfaces

Figure 4.4: Deformed meshes of angled reinforced cubes with small element size

[5]For a Mooney-Rivlin model, $E_{\varepsilon=0} = 6(C_1 + C_2)$ and $G = 2(C_1 + C_2)$.

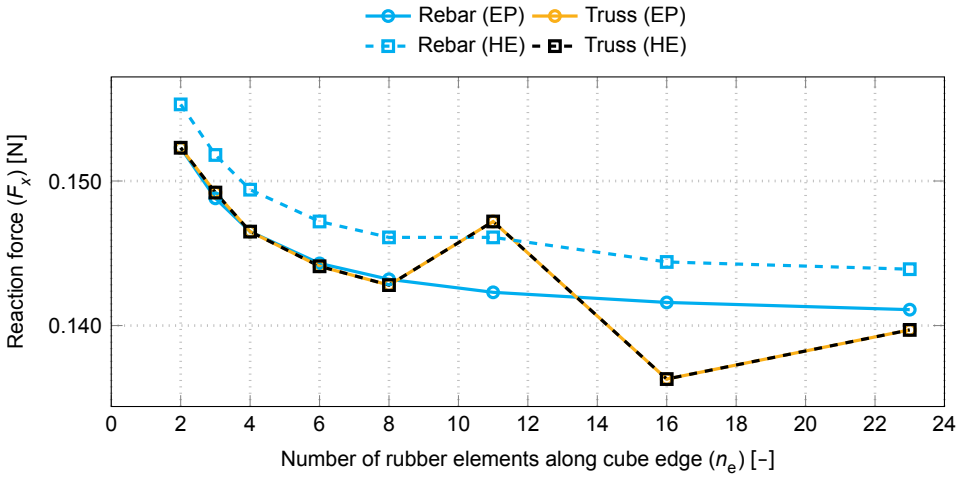

Figure 4.5: Reaction force mesh convergence

4.3.2. Results

Looking at the results of the mesh convergence analysis (Figure 4.5), the rebar models show a more stable behaviour. The truss models are oscillating around the equilibrium, whereas the rebar models approach from a single side. The oscillation in the truss model reaction forces only starts when $n_e > 8$, where the element size becomes smaller than the distance between the adjacent crossover points. This means the cord sections between crossover points are represented by multiple host and embedded elements. A difference can be observed in the hyperelastic (HE) ebar model, compared to the other models. The reported reaction force is ±2 % higher compared to the other models, whereas the rebar elastic-plastic (EP) model shows agreement with both truss models.

The rebar model undergoes a consistent element size reduction of both the rubber host and embedded rebar elements, whose relative positions remain unchanged. In this case the rubber and rebar elements have the same dimensions in the *xy*-plane, where the (projected) nodes are coinciding. The rubber elements in the truss model are identical to their respective rebar counterpart (same mesh size reduction), however the size of the truss elements is more arbitrary. In general their nodes will not be aligned with those of the rubber, resulting in truss elements having nodes in a single or multiple rubber host elements.

Interestingly at large element size both methods calculate a similar reaction force (0.26 % difference), with large differences (up to 6 %) occurring when $n_e > 8$. Looking at the meshes in detail (Figure 4.6), the coarser meshes ($n_e \leq 8$ in this case) consist of rubber elements hosting cord elements in multiple orientations. The finer meshes ($n_e > 8$) on the other hand consist mostly of rubber elements with either no or single-orientation cord elements embedded. Because of the high stiffness ratio between the cord and rubber materials, the four-node (originally square) rubber elements are significantly stiffer along one diagonal orientation. This restricts the shear deformation of the element, also known as shear locking [53].

Shear locking can be prevented by ensuring embedded cord elements have multiple orientations and nodes in a given rubber host element [54]. The rubber mesh should not be refined into micro scale modelling (such that only one cord orientation would be embedded), and otherwise cord element lengths should be more than two times smaller than their host rubber element dimensions. The rebar model does not encounter this change from macro to micro scale representation, since the stiffness properties are smeared over the host element (and therefore remaining in the macro scale).

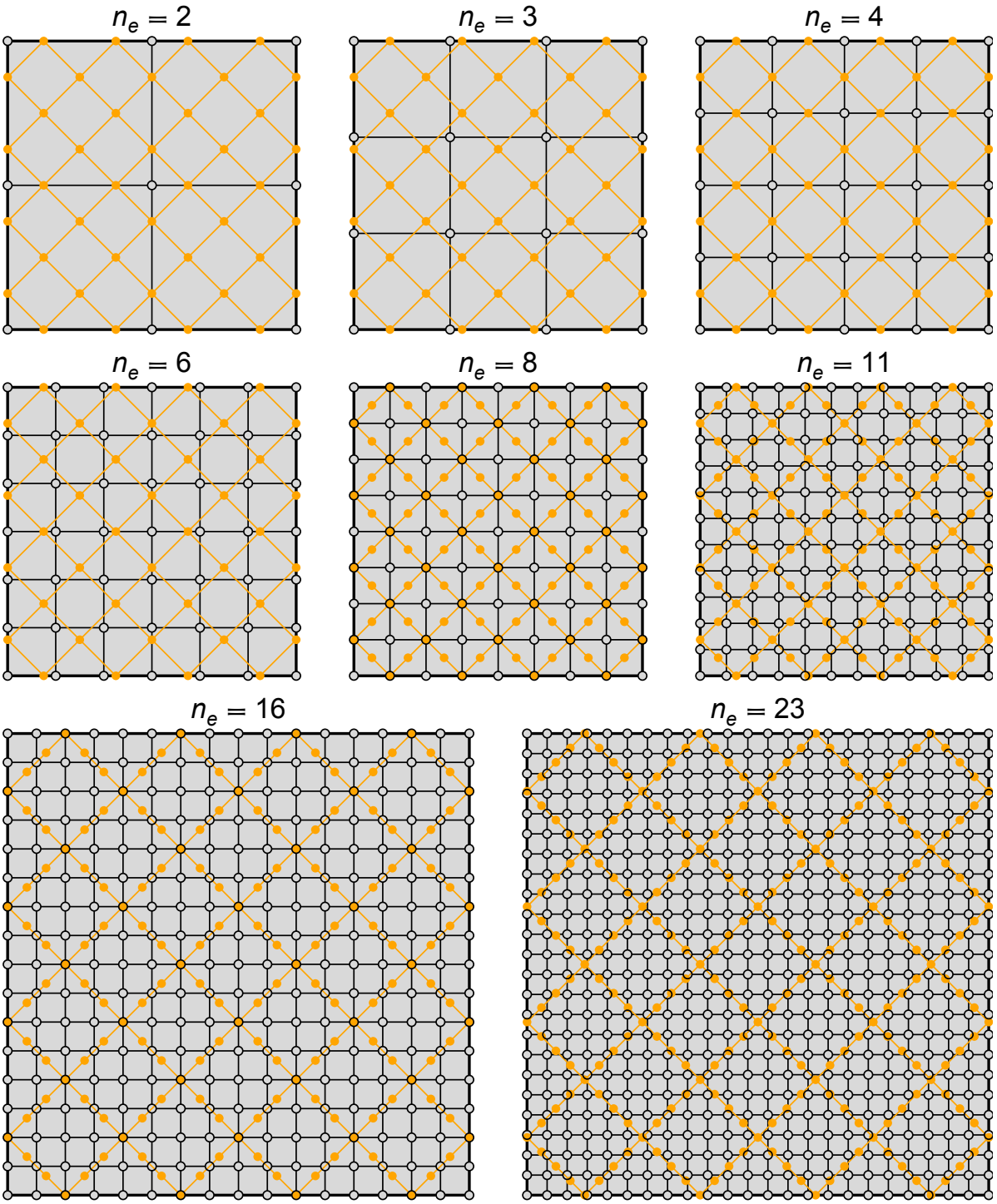

Figure 4.6: Rubber and cord meshes of the truss model with increasing mesh density (projected) on the *xy*-midplane

5

McKibben Actuator

Following the unit tests in Chapter 4, an artificial muscle actuator is modelled in accordance with studies performed by Klute and Hannaford [17] and ten Thije et al. [18]. This pneumatic artificial muscle (also referred to as McKibben actuator after one of its first adaptors, Joe McKibben [55]) consist of an inflatable inner bladder inside a double-helix braid clamped at both ends. Upon inflation the circumferential stress in the bladder is transformed into an axial force by the braid, due to a scissoring effect caused by the uniaxial reinforcements of the braid tending to align with the major principal stress direction (see Section 2.3.2).

This single layer cylinder is a simple representation of the cylindrical body of the Large Bore Hose (LBH). The design of the cylinder is based on the study of ten Thije et al., which considers a McKibben actuator inflated to 5 bar (0.5 MPa). Because the initial cord angle in the braid is 17.69° (measured with respect to the longitudinal axis), upon inflation the cord angles will tend towards the neutral angle resulting in an axial contraction of the braid during phase I deformation (as explained in Section 2.3.2). Subsequently the actuator is stretched axially to its original length, where the required (actuator) force is measured.

Section 5.1 presents the material properties of the rubber bladder and cord braid. The geometry of the McKibben actuator is discussed in Section 5.2. Section 5.3 covers the specifics of the rebar and truss Finite Element (FE) models. Section 5.4 discusses the results of the Finite Element Analyses (FEAs), comparing the two modelling approaches with the data provided by ten Thije et al.

5.1. Material data

The material data used in this analysis is as described in Section 4.1 as provided by ten Thije et al. The rubber material is modelled as an incompressible Mooney-Rivlin solid with parameters 0.1184 MPa and 0.1057 MPa, with Equation (4.1) the strain energy density function. The cord material is a initially linear elastic (E_0 = 3.5 GPa) polyester material with Nadai hardening occurring when the axial strain exceeds 2 %.

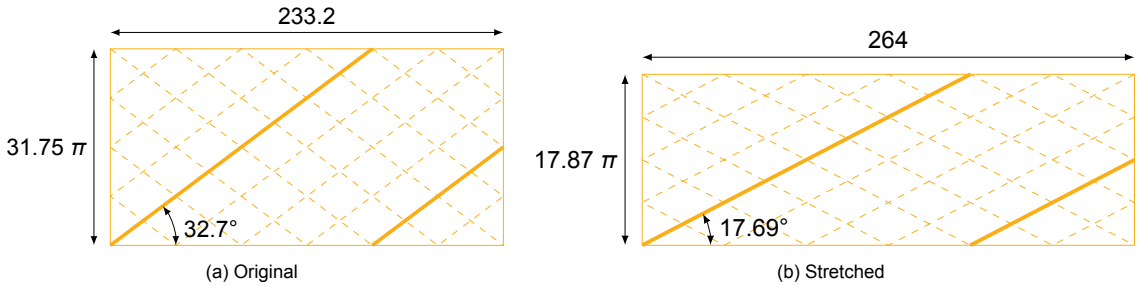

Figure 5.1: Schematic representation of the unfolded braid

5.2. Geometry

The McKibben actuator geometry is shown in Figure 5.2 and is in agreement with the dimensions provided by Klute and Hannaford. The rubber bladder has an inner diameter of 0.5 in (12.7 mm) and a thickness of $^3/_{32}$ in (2.38 mm).

The cylindrical polyester braid has an original diameter D_0 of 1.25 in (31.75 mm), where one thread (highlighted in Figure 5.1) revolves 1.5 times around the braid ($\varphi \in [0, 3\pi]$) and has a length of 277.1 mm. The original length L_0 of the braid is therefore 233.2 mm, with the cords at an angle α_0 of ±32.7°. The linear density (axially, z-direction) of the braid is given by the supplier as 24 g m^{-1}. Given that the polyester braid has a material density of 1340 kg m^{-3} [18], the original (axial) cross-sectional area is 17.91 mm^2.

The polyster braid is applied on the outside of the rubber bladder, where it is stretched to match the length of the bladder (264 mm). This stretch is assumed to be achieved by a pure shear deformation, resulting in an angle change without strain occurring in the cords. The stretched braid has a cord angle of ±17.69°, which decreases the diameter to 17.87 mm and lowers the cross-sectional area to 15.82 mm^2.

The cord radius is taken as the offset between the rubber bladder outer radius (8.73 mm) and the radius of the polyester braid (8.933 mm), i.e. 0.203 mm. Assuming the cords have a circular cross-section, the area is 0.130 mm^2. Given the braid cross-section in z-direction is 15.82 mm^2, the braid consists of 116 cords at an angle of ±17.69°.

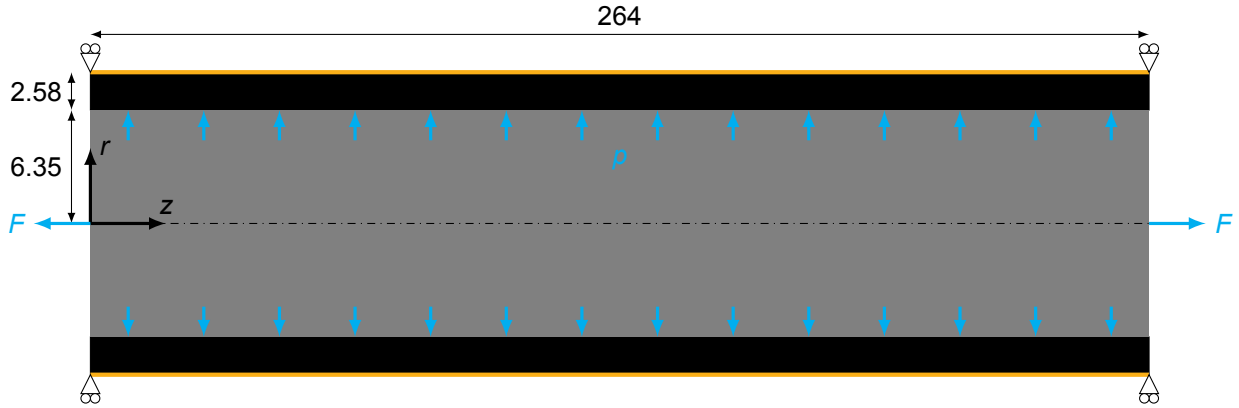

Figure 5.2: Free body diagram and geometry of the McKibben actuator

5.3. Finite element analysis

In order to compare the cord-rubber capabilities of both the 3D truss and axisymmetric (2D) rebar modelling approaches, two models were created based on the geometry discussed above.

5.3.1. Truss model

A 3D FE model is created to represent the rubber bladder and cord braid, where trusses are used to simulate the uniaxial tensile behaviour of the cords.TANIQWind was used to find a suitable winding pattern with 118 cords, close to the requested 116 cords in Section 5.2. In order to maintain the correct axial cross-section of the braid, the area of a single cord is lowered to 0.128 mm^2. With 118 cords crossing a given $r\varphi$-plane at a constant angle, the cylindrical actuator can be reduced to $\frac{1}{59}$ revolution (the angular difference between two cord crossover points), giving an angular portion with a $\Delta\varphi$ of 6.10°. Additionally half symmetry is applied to decrease the model size.

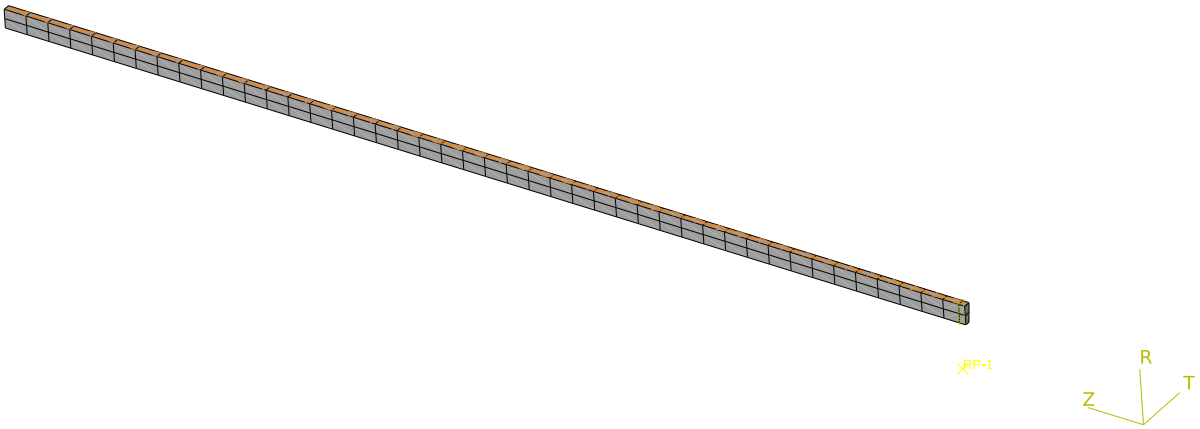

Figure 5.3: Cylindrical portion mesh and loading of truss model

The rubber bladder consists of solid hybrid `C3D8H`[1] elements. Since the truss method showed oscillatory behaviour in the mesh convergence study on the unit test cubes (see Figure 4.5), the dimensions of the rubber elements are chosen to be similar to the rebar model discussed in Section 5.3.2. The rubber mesh is created using the FEA Toolbox, TANIQ's in-house meshing software for cord-rubber products. As a result, the rubber mesh consists of two elements radially (ΔR = 1.292 mm) and one in circumferential direction.

The cord braid is represented using `T3D2`[2] elements, since the cords are assumed to be uniaxial load carriers. Because of the portion angle reduction, the trusses form a diamond pattern on the radial outside of the bladder (with an angle of 17.69° with the z-direction). The truss elements have a length of 0.783 mm, or two elements per side of such diamond. This ensures sufficient cord nodes to be embedded in a given rubber host element, based on guidelines by Yu et al. [53] and ten Thije et al. (see Figure 4.6) to reduce shear locking.

The cord mesh consists of 712 truss elements, placed in a diamond shaped pattern in axial direction where each diamond consists of eight trusses. Consequently the axial length of the cord part is 0.846 mm larger than the actual actuator length. This defines the axial length of the rubber mesh, which consists of 44 elements axially (ΔZ = 3.019 mm). To correct this discrepancy, the rubber elements at the cylinder ends are split at 132 mm from the axial middle.

Symmetry in axial direction is applied on the rubber nodes at the axial midplane, restricting displacement in Z-direction and rotation around the R- and T-axes. The rubber elements at the cylinder ends are kinematically coupled to a reference point, which has its displacement in R-direction and rotation around the T-axis restricted in order to simulate a clamped edge. Finally, in order to enable the angular portion to represent a fully revolved structure, symmetry in T-direction (cylindrical coordinate system) is applied to each of the rubber side faces.

[1] Continuum three-dimensional 8-node linear brick with hybrid formulation
[2] Three-dimensional 2-node linear truss

During the inflation step the actuator is loaded with a pressure of 0.5 MPa on the inner surface and an axial force of 1.074 N, which is 1⁄59 (respective to the angular portion) of the force that would result from the internal pressure acting on the end caps. During this step the reference point is allowed to move freely along the *Z*-axis, resulting in an axial shrinkage of the actuator. Subsequently the stretching step is performed by returning this reference point to the origin.

5.3.2. Rebar model

Since rebar smears directional properties over the element to which it is assigned, it can be used to represent the cord braid in the McKibben actuator on a macroscopic level. Both the geometry (cylindrical rubber and braid) and loading (inflation and axial stretch) are axisymmetric, allowing the model to be reduced to a 2D representation. Additionally half symmetry in axial direction was applied, reducing the size of the model.

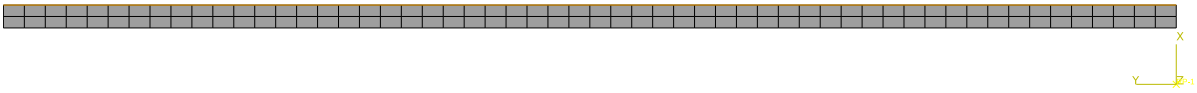

Figure 5.4: Axisymmetric rebar mesh and loading

The rubber bladder is made of `CGAX4H`[3] elements. The element size was determined with a mesh convergence study, where the actuator stretch upon inflation was used as convergence metric. The base model had 14 elements in axial (as a result of a maximum element size of 10 mm) and one in radial (thickness) direction. The mesh converged at 112 elements, as doubling the number of elements resulted in an improvement of only 0.05 % (<0.1 %). As a result the used mesh consists of 112 elements, two in radial (thickness) direction (Δr = 1.292 mm) and 56 in axial direction (Δz = 2.357 mm).

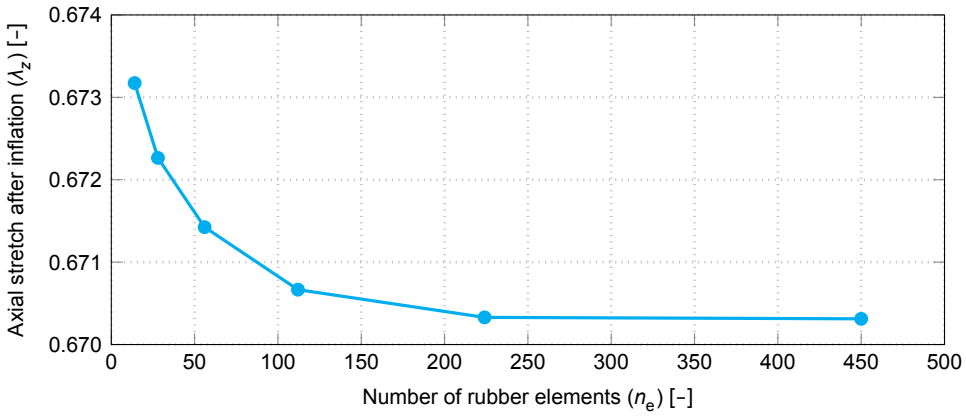

Figure 5.5: Inflation stretch mesh convergence (rebar HE)

The cord braid uses rebar properties assigned to `SFMGAX1`[4] elements. The nodes of these elements are coincident with the nodes on the radially outer surface of the rubber part, where the degrees of freedom are linked through embedding. This restricts the surface nodes to follow the movement of the coinciding rubber nodes, while adding anisotropic stiffness to the outer edge of the rubber mesh. The rebar properties are based on the number of cords in the truss model (discussed in Section 5.3.1). Since the axisymmetric model allows axial twist, both a positive and negative angle layer have to be specified. The rebar properties are as follows: a cord area of 0.128 mm^2, spacing of 0.906 mm, and reinforcement angle of ±17.69°.

[3] Continuum axisymmetric with twist 4-node linear quadrilateral with hybrid formulation
[4] Membrane-like axisymmetric with twist 2-node linear surface

Since the surface elements are embedded in the rubber elements and as a result have no independent degrees of freedom, the boundary conditions and loadings are applied on the rubber part. Symmetry in axial direction is applied on the nodes at the axial midplane, restricting displacement in *Y*-direction and rotation around the *X*- and *Z*-axes. The nodes at the cylinder end have all degrees of freedom constrained in a kinematic coupling with a reference point at the origin, of which the radial displacement (*X*-direction) and rotation around the *Z*-axis are restricted in order to simulate the clamped ends of the artificial muscle.

The actuator is loaded in two steps: during the first step a pressure of 0.5 MPa is applied on the inner surface, where an axial force of 63.34 N in negative *Y*-direction represents the internal pressure acting on the cylinder ends. During the second step the actuator is stretched to its original length, realized by returning the reference point to its origin.

5.4. Results and discussion

The analyses were performed in ABAQUS/2018 with parallelization using two Central Processing Units (CPUs). The performance of both modelling strategies is assessed looking at the global structural response of the actuator. On one hand there is the change in winding angle the cord braid goes through during inflation (step 1), on the other hand the force required to return the actuator to its original length (step 2).

Table 5.1: Analysis results at the step instances

	Axial stretch	**Reaction force [N]**	**Cord angle [deg]**		**Cord strain [%]**	
Step	1	2	1	2	1	2
Rebar	0.6795	1382	50.97	30.77	2.438	9.832
Truss	0.6802	1381	50.95	30.71	2.467	9.777

5.4.1. Axisymmetric twist

Initial rebar models used `CAX4H` elements in the rubber part and `SFMAX1` elements in the cord braid part. These elements do not allow twist around the axis of revolution (*Y*-axis) in an axisymmetric coordinate system. The models were observed to fail consistently in achieving equilibrium convergence around 30 % of the inflation step (0.15 MPa), whereas a similar 3D portion model with an revolution of 0.1° (using the respective 3D elements, `C3D8H` and `SFM3D4`) did not experience any difficulties reaching full inflation.

Allowing axial twist (hence the `G` in the element definition) did resolve this convergence issue. At the end of the inflation step the maximum twist occurring was 4.09×10^{-16} rad at the reference point. This twist only starts appearing once the cords in the braid are getting loaded. Even though the deformation and stresses originating from this twist are negligible, it indicates that restricting the axial twist results in an over-constrained model and should therefore be allowed.

5.4.2. Reaction force

Klute and Hannaford created a theoretical model to calculate the actuator force of a rubber-braid McKibben actuator. The model takes the non-linear rubber material properties into account, whereas the braid was assumed to be inextensible (relying solely on braid kinematic). Subsequently ten Thije et al. constructed an FE model that allows braid extension and plastic deformation, which they validated through experimental tests. The experimental data is shown in Figure 5.6a.

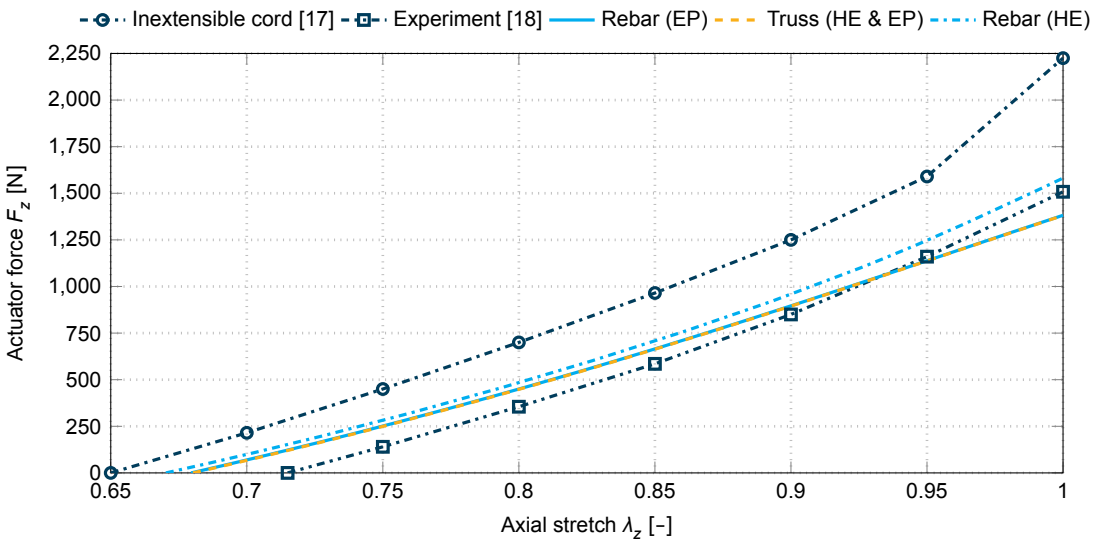

(a) Force required to stretch the McKibben actuator to its original length (step 2)

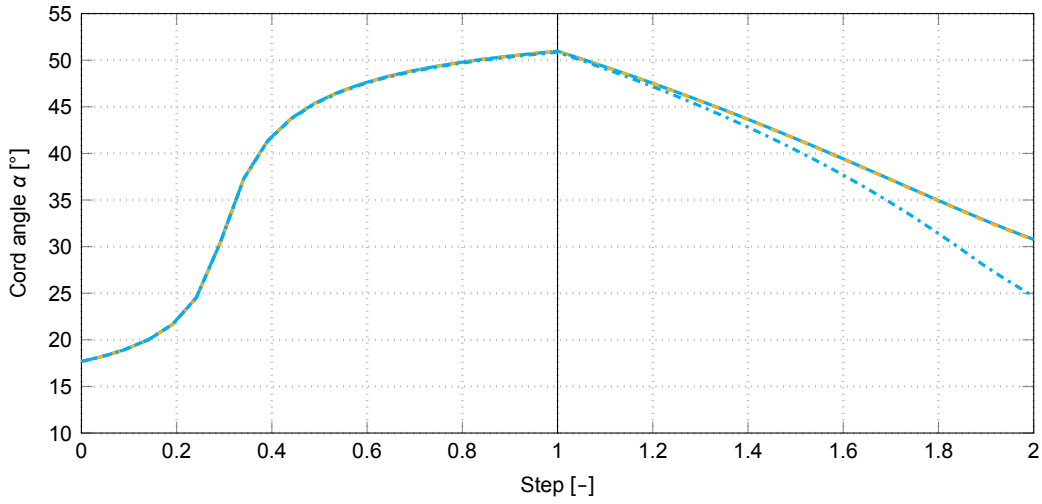

(b) Braid angle at the axial middle of the actuator

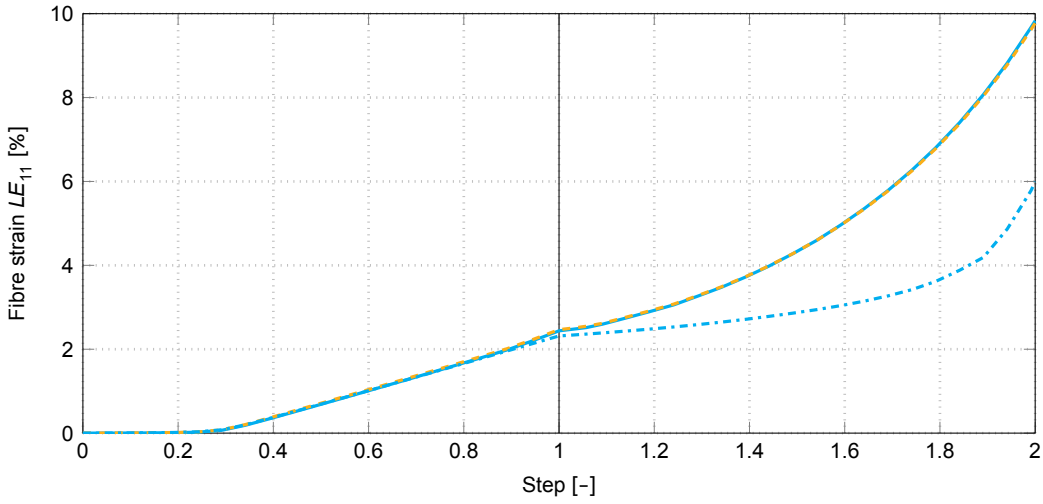

(c) Strain of the fibre braid at the axial middle of the actuator

Figure 5.6: Comparisons between the rebar and truss models during inflation (0 < step ≤ 1) and stretching (1 < step ≤ 2)

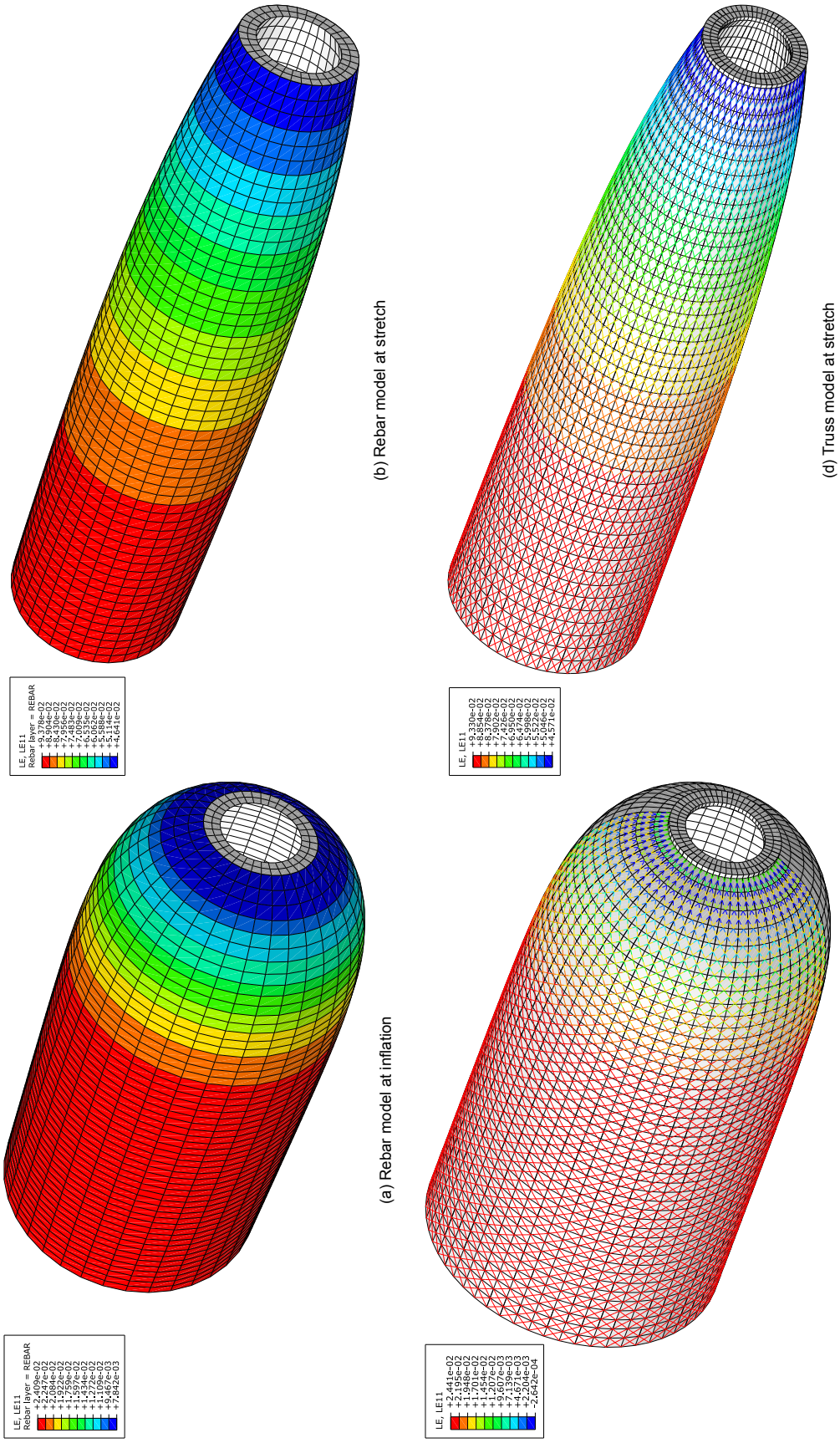

Figure 5.7: Logarithmic strains in the cord braid at the end of each loading step

The actuator forces of the elastic-plastic (EP) rebar and truss model show almost perfect agreement with each other. A difference is observed with the experimental data of ten Thije et al., where the actuator has less axial shrinkage after inflation. In their FEA plastic strain started occurring in the cords at 2.5 bar, whereas the maximum axial stresses in the EP rebar and truss models at this pressure were 23.95 MPa and 24.85 MPa respectively. Furthermore, the EP rebar and truss actuators show a lower stiffness during the stretching step, where the actuator forces at the end of the stretch are 91.6 % of the load reported by ten Thije et al. The hyperelastic (HE) rebar model, however, shows a stiffer behaviour upon stretching. The linear stiffness is 90.6 % of the experimental data, compared to 83.5 % shown by the EP rebar and truss models.

5.4.3. Reinforcement angle and cord strain

Figure 5.6b shows the evolution of the braid angle during the two deformation steps at the middle of the actuator. In the inflation step the two deformation phases typical for a cord-rubber pressure vessel can be observed. 90 % of the angle change is achieved around 60 % of the pressurisation, after which the angle gradually increases towards the neutral angle. At around 30 % inflation the cords start straining (Figure 5.6c, increasing linearly with the pressure. The deformation during the first 30 % of the pressurization is achieved solely by the cords shearing towards the principal load direction, with the neutral angle of an infinite ideal cylindrical pressure vessel being 54.7° [33].

A divergence between the HE rebar and the other models is observed during the stretching step. The decrease in cord angle is larger as a result of the axial stretch, resulting in lower strains occurring in the cords. The increased reaction force discussed earlier is a consequence of the cords being aligned more with the *z*-axis (smaller winding angle).

5.4.4. Analysis time

ABAQUS/2018 was used to perform the FEAs, with two CPU parallelisation. The CPU time ABAQUS needed to perform both FEs serves as a first indicator on the time savings that can be achieved by using an axisymmetric model with smeared properties (rebar) instead of a 3D model using trusses at the exact cord positions. The former required 7.1 s of CPU time whereas the latter needed 11.8 s, a time saving of 40 %.

6

Finite Element Analysis of Multilayered Cord-rubber Cylinders

In order to study the effect of reinforcement angle variation along the *z*-axis and through the thickness of a cord-rubber pressure vessel, a parametric model with three cord layers is created. This research is an extension of studies performed by Tonatto et al. [4], Gao et al. [7], Xing et al. [47]. These studies looked at the influence of the cord angle (uniform in all layers) on the structural response of cylindrical cord-rubber pressure vessel.

Through varying the reinforcement angle axially and radially in a three-layer cylinder, upon inflation the influence of these angles on the structural response can be examined. Like the McKibben actuator, this Multilayered Cylinder (MLC) is a simplified representation of the cylindrical hose body of the Large Bore Hose (LBH). The edges of the cylinder are clamped to simulate end caps, as well as differentiate the influence of the reinforcement angle axially.

Sections 6.1 and 6.2 present the geometry and material of the MLC. Similarly to Chapter 5, both a truss and rebar Finite Element (FE) model will be developed. The details of the FE models are discussed in Section 6.4. Section 6.3 shows the locations where the reinforcement angle will be specified in the various parametric studies. Firstly, the reinforcement angle is kept uniform throughout the MLC, similar to the studies of Tonatto et al., Gao et al., Xing et al. in Section 6.5. Subsequently the reinforcement angle is varied radially and axially in Sections 6.6 and 6.7, respectively.

6.1. Geometry

The MLC cylinder has a length of 1000 mm, with an inner diameter of 200 mm and a thickness of 16 mm (depicted in Figure 6.1). The aspect ratio of 5 reduces the effect of the clamped edge on the middle of the MLC. Even though this value is smaller than the aspect ratio of the LBH cylindrical section (≈11), it was chosen to sufficiently distance the cylinder edge and middle while limiting the FE model size. A radius-to-thickness ratio of 6.25 reduces the gradient of the radial stress distribution [35, 46, 47], compared to ≈4 in the LBH cylindrical section. The MLC is given three cord reinforcement layers, which allows assessment of the influence of the angles in the inner, intermediate, and outer layers.

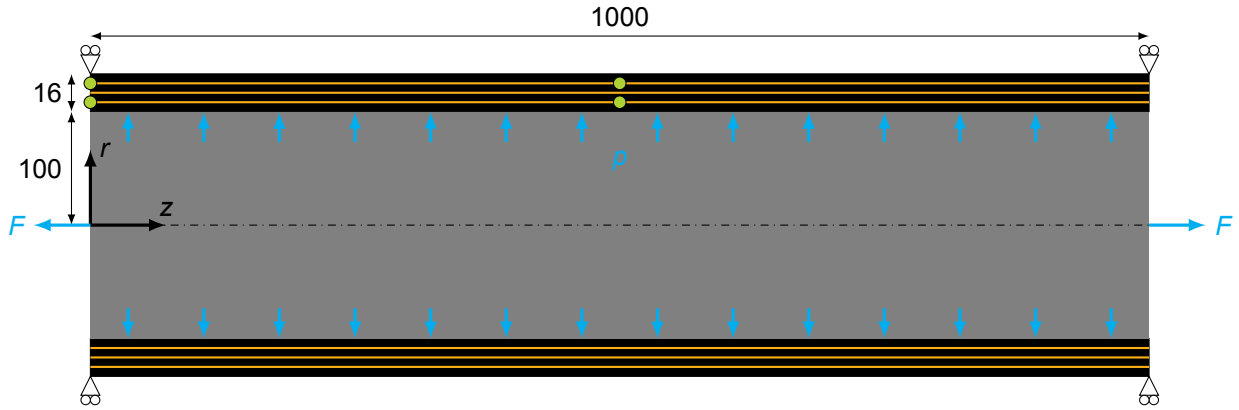

Figure 6.1: Free body diagram and geometry of the multilayer cylinder
● : cord angle parameter

6.2. Material data

The rubber is modelled using the Ogden material model (N = 3, see Section 2.2.1) with the parameters provided in Table 6.1a. These were obtained by evaluating uniaxial tensile test data using ABAQUS/2018. This material model is stable within the ranges indicated in Table 6.1b (i.e. where $\partial\sigma/\partial\varepsilon > 0$). The uniaxial test data and corresponding Ogden fit are shown in Figure 6.2a.

Table 6.1: Ogden material model properties

(a) Parameters

n	1	2	3
μ_n	-0.171	0.479×10^{-3}	0.706
α_n	2.365	9.891	1.590

(b) Stability strain ranges

Strain mode	Min. compression	Max. tension
Uniaxial	-0.075	2.240
Biaxial	-0.444	0.040
Planar	-0.083	0.090

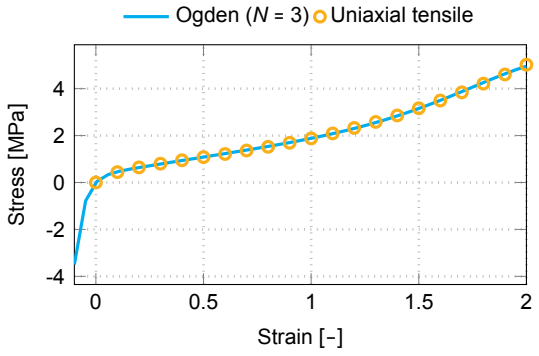

(a) Rubber uniaxial tensile test data and Ogden fit

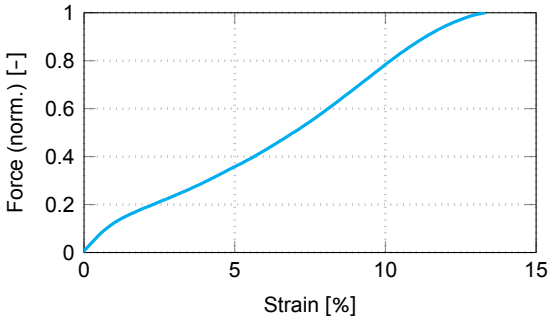

(b) PET 1100 2x3 yarns tensile test data

Figure 6.2: Material data used in the MLC FEA

As cord material Polyethylene Terephthalate (PET) 1100 2x3 yarns are used. The tensile properties have been measured through a series of tensile tests in the *Delft Aerospace Structures and Materials Laboratory*, which are discussed in detail in Appendix A. Figure 6.2b shows the average force-elongation curve obtained from the tensile tests. Since PET is hyperelastic, the Marlow material model is used provided with the uniaxial stress-strain test data. Even though Section 5.4 concluded that the axisymmetric rebar method using a hyperelastic material model for the cords diverges from the other models[1], the Marlow material model is used to assess whether it impacts the relation between the reinforcement angle inputs. This material model requires the uniaxial test data to be provided as nominal stress, which is obtained by dividing the force measurements by the cord cross sectional area (0.636 mm^2 with a cord diameter of 0.9 mm).

6.3. Angle definition and winding parameters

The aim of the MLC model is to investigate the influence of radial and axial variation of the cord angle on the deformation upon inflation. In order to allow these variations, the MLC is parametrised such that cord angle can be specified at the following points: axially at the edge and in the middle, on the outer and inner reinforcement layer. This results in four parameters, indicated in Figure 6.1.

The reinforcement angle on the intermediate layer is the average of angles in the inner and outer layers at a given axial location. When the specified angles at the edge and axial middle differ in a given layer, the reinforcement angle is varied linearly over the axial distance. Since changing the winding angle on a cylindrical profile requires friction to keep the cords on non-geodesic paths, some designs could be infeasible to realise when the available friction is insufficient. In this study, however, friction limitations are not considered when generating the cord paths.

For each design (a given set of angle parameters) the cord path is generated using TANIQWind. Subsequently this path is used to select a winding pattern which results in 100 % cord coverage. The cord coverage is measured at the axial centre of the MLC, which indicates how much of the circumference is covered by cords. It is dependent on the number of cords in a layer n_C, the winding angle α, the cord width D_C, and the diameter of the cord layer profile D_L:

$$c = \frac{D_C n_C}{\pi D_L \cos\alpha} \tag{6.1}$$

The cord angles are limited to a range between 45° to 70°. The lower bound of 45° was determined throughout the development of the FE models, where the convergence rate dropped drastically for designs which had low reinforcement angles specified. Furthermore, designs with a low winding angle at the axial middle would result is a large amount of cords in the MLC to satisfy the coverage requirement. Even though cord usage is not considered in the design optimisation of the MLC (discussed in Chapter 7), the inherent increased cord usage makes lower angles undesirable in the LBH optimisation (where the same design space will be used). The upper bound is set at 70°, centring the cord angle range around the neutral angle of thin-walled anisotropic pressure vessels (see Section 2.3.2). Since cord build up increases with the winding angle (due to a larger projected cord cross section on the $r\varphi$-plane), higher winding angles are undesirable as well.

[1] Elastic-plastic rebar and truss, and hyperelastic truss

6.4. Finite element analysis

As was the case in Chapters 4 and 5, FE models will be created using both the axisymmetric rebar and three-dimensional truss approach.

6.4.1. Truss model

The 3D FE model is generated using the existing framework of TANIQ's FEA Toolbox, which has been extended to enable the input file and mesh creating of MLC designs. Similarly to the single layer truss model (see Section 5.3.1), the model can be reduced to an angular portion of $\Delta\varphi$. The size of this portion is dependent on the winding pattern in the innermost layer. If other layers have a different number of cords, the cross-sectional area of the truss elements is scaled such that the total cross-sectional area in a given $r\varphi$-plane matches the actual pattern.

The rubber mesh consists of solid hybrid `C3D8H`[2] elements. Radially the mesh consists of seven elements (Δr = 2.268 mm), such that the three even rows each have a cord layer embedded. In axial direction the mesh has 436 elements (Δz = 2.294 mm) to keep the element aspect ratio close to unity. The number of elements in tangential direction is determined by the size of the angular portion, where an aspect ratio (radial-to-tangential) between 1 and 2 is desired. Figure 6.3 shows a close-up of an example MLC FE mesh (1.4° portion), where the reinforcement layers have a uniform angle of 45°.

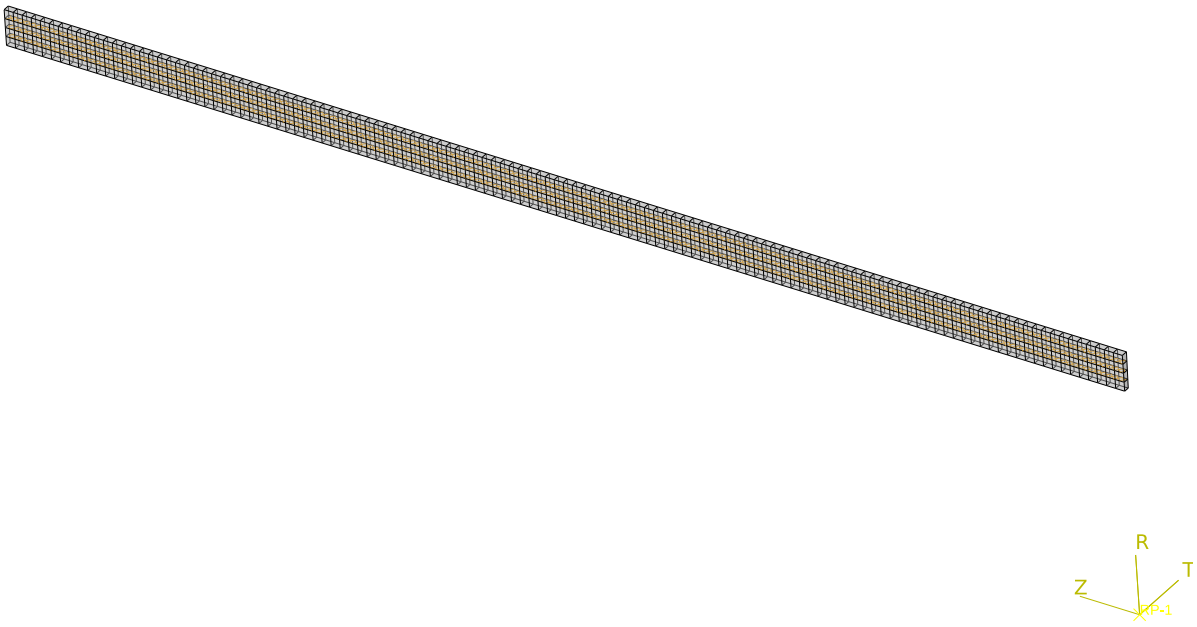

Figure 6.3: Close up of the truss mesh of a Multilayer Cylinder with a uniform cord angle of 45°

The cord layer meshes are constructed using `T3D2`[3] elements, which are placed along the exact cord paths and form a diamond pattern. Since the exact element length is dependent on the portion size and winding angle, a maximum length of 1 mm is specified in the FEA Toolbox. This will ensure sufficient nodes are embedded in any given rubber host element to prevent shear locking from occurring [18].

[2] Continuum three-dimensional 8-node linear brick with hybrid formulation
[3] Three-dimensional 2-node linear truss

Since the cord angle will be variable throughout the MLC and the cord mesh is based on the winding path generated by TANIQWind, the resulting cord mesh is not symmetric in *z*-direction. Therefore it was not possible to reduce the model size by applying symmetry conditions at the axial midplane. The nodes on the tangential faces (facing in *T*-direction) are constrained by cylindrical symmetry conditions along the *T*-axis, preventing displacement along this axis and rotation around the *R*- and *Z*-axes. The nodes axial edges (*Z*-axis) of the rubber mesh each have their degrees of freedom linked to their respective reference point through a kinematic coupling, whose displacement along the *R*- and *T*-axes as well as all rotations are constrained. Finally the radially outer rubber nodes at the axial midplane have their displacement in *Z*-direction constrained to prevent rigid-body motions.

The MLC is inflated with a pressure p of 30 bar (3 MPa), which ensures phase II deformation without any design reaching peak cord strain (the analysis results are discussed in Sections 6.5 to 6.7). As the internal pressure also acts on the end caps, the axial load is proportional to the angular portion size $\Delta\varphi$ [rad]:

$$F_Z = p\pi r^2 \frac{\Delta\varphi}{2\pi} = 15\,000\Delta\varphi \qquad \text{[N]} \tag{6.2}$$

6.4.2. Rebar model

Similarly to the rebar model generated for the McKibben actuator (Chapter 5) both the geometry (due to rebar's smeared properties) and loading (inflation) are axisymmetric, allowing the reduction of the FE model to a two-dimensional axisymmetric design space. Since the cord mesh does not represent the physical cord paths but instead averages the directional stiffness over the element, the cord mesh is independent of the cord angles in the reinforcement layers. As a result half symmetry can be applied consistently (in contrast with the truss model) to reduce the FE model size. Figure 6.4 shows the generic FE mesh of the MLC.

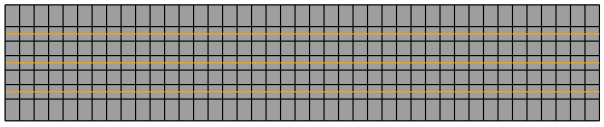

Figure 6.4: Close-up of the generic axisymmetric rebar mesh of the Multilayer Cylinder

Since during the development of the rebar model in Section 5.3.2 axial twist had to be allowed to improve convergence, the rubber mesh consists of `CGAX4H`[4] elements. In radial direction the mesh has seven elements, where the inner five have a width of 4 mm such that the rebar elements are centred in their rubber host elements. The outer and inner rubber element row have a width of 3 mm, where adding additional elements on these rows did not change the Finite Element Analysis (FEA) results of the MLCs at the design space corners ($\alpha \in \{45, 70\}$). In axial direction the mesh consists of 125 elements (Δz = 4 mm), resulting in a unity aspect ratio of the cord hosting elements.

The cord mesh size is kept consistent with the host rubber elements, where each layer has 125 `SFMGAX1`[5] elements axially. Because of the rubber mesh construction, the rebar surface nodes lie radially exactly in between two rubber nodes at identical *z*-coordinates. Since rebar properties are assigned through the use of element sets, if the winding angle varies axially each element is assigned to its unique element set. The rebar angle is obtained from the cord path, while the spacing is obtained from the pattern generated by TANIQWind.

The rubber nodes at the axial middle of the MLC have axial symmetry boundary conditions applied, effectively restricting their displacement in *z*-direction and rotation around the φ-axis. The rubber nodes at the opposite side (edge) are kinematically coupled to an axial reference point to simulate a clamped end, which in turn is only allowed to move and twist along the *z*-axis. Like the MLC truss model an internal pressure of 3 MPa is applied, combined with an axial load of 94.25 kN which represents the pressure acting on the end cap.

[4] Continuum axisymmetric with twist 4-node linear quadrilateral with hybrid formulation
[5] Membrane-like axisymmetric with twist 2-node linear surface

6.5. Uniform angle

In the first study the cord angle is defined as uniform throughout the MLC, by equalling all four input parameters. Over the allowable angle range ($\alpha \in [45, 70]$) 25 designs were evaluated spaced evenly over the interval. The results of the parametric study are visualised in Figure 6.5.

Figure 6.5a shows the peak strain in each reinforcement layer, in relation to the uniform cord angle. In both the truss and rebar cases, the peak strain on the inner layer is generally the highest on the inner layer and decreases outwards. This is consistent with the findings of Xing et al. [47], who analysed the radial stress distribution in thick-walled E-glass/epoxy cylindrical pressure vessels. Tonatto et al. [4] used a 3D rebar FE model of a cord-rubber MLC with uniform reinforcement angle, where the cord stress on the outer layer was 25 % lower than on the inner layer. The cord angles resulting in the lowest peak strain are 55.4° and 57.5° in the truss and rebar models, respectively. The rebar model shows a more consistent radial strain (stress) distribution compared to the truss model, where the peak strains seem to diverge and show more noise when the cord angle increases. Finally, at lower winding angles the two approaches show the most agreement but diverge with increasing cord angle, especially when $\alpha > 58°$.

At this angle the axial location of the peak strain can be seen to change from the MLC middle ($z = 500$ mm) to the clamped edge ($z = 0$ mm) in Figure 6.5b. The peak strain occurs at either of these locations in a binary-like behaviour, as a result of the simple geometry of the MLC. When $\alpha < 58°$, the MLC is seen to experience predominantly a radial extension (Figure 6.5c) and axial contraction (Figure 6.5d)[6]. Figure 6.6 shows the strain distribution and deformation of MLCs with 45° and 70°, the extreme values of the permitted alpha range which show the largest deformation.

The relation between initial cord angle and both the radial and axial stretch shows the typical phase I deformation behaviour. Smaller initial uniform cord angles ($\alpha < 58°$) result in radial expansion and axial contraction, vice versa for larger angles ($\alpha > 58°$). The noisiness in the $\varepsilon_{max} - \alpha$ trend of the truss model (Figure 6.5a) appears at larger angles, where the peak strain is located near the clamped edge. As can be seen in Figure 6.6d, the deformation shape causes a stress concentration at the edge. One of the known complications of the truss model is the occurrence of stress concentrations when the trusses do not form a half or full diamond at a constrained axial edge.

6.6. Radial angle variation

The stacking sequence (i.e. radial angle variation) influences the stress distribution through the thickness, and therefore ultimately the strength of the design [4, 35, 46, 47]. Where the previous study in Section 6.5 assumed a uniform cord angle throughout the MLC, in this study the cord angles in the outer and inner reinforcement layer, α_O and α_I respectively, are varied from 45° to 70°. The cord angle on the middle layer is the average of the other layers, resulting in a linear angle distribution through the thickness. The cord angle is constant within each layer, resulting in a two-dimensional design space (based on the parameters discussed in Section 6.3).

In order to visualise the dependence of the deformation and loads on the cord angle parameters, a linearly distributed 25 × 25 grid was created such that $\alpha_O, \alpha_I \in [45, 70]°$. For both the rebar and truss methods, 625 FEAs are performed using ABAQUS/2018 with four node parallelization. At the end of each analysis the peak strain in each cord layer, together with the axial position at which it occurred, was recorded. This allows for assessment of the dependency of the structural efficiency on the cord angle parameters. To study the influence of these parameters on the deformation, the radial stretch (at the axial middle, $z = 500$ mm) and axial stretch were registered as well.

[6] Since the deformation is phase II, where the entire structure expands equally in all directions, the stretches at the end of phase I are lower than indicated in Figures 6.5c and 6.5d.

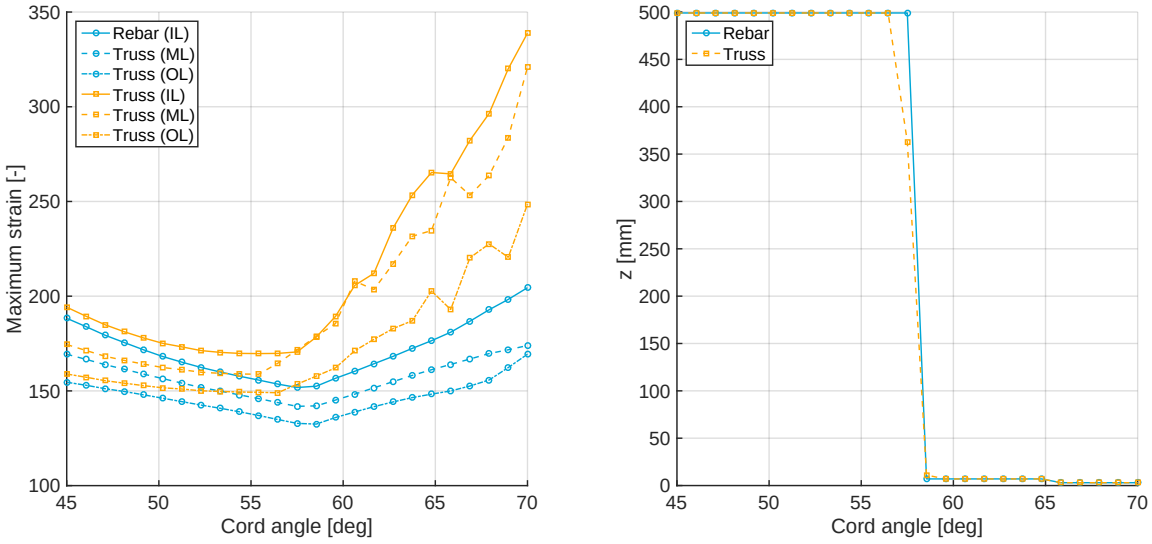

(a) Peak strain in each cord layer
(IL = inner layer; ML = middle layer; OL = outer layer)

(b) Axial location of peak strain

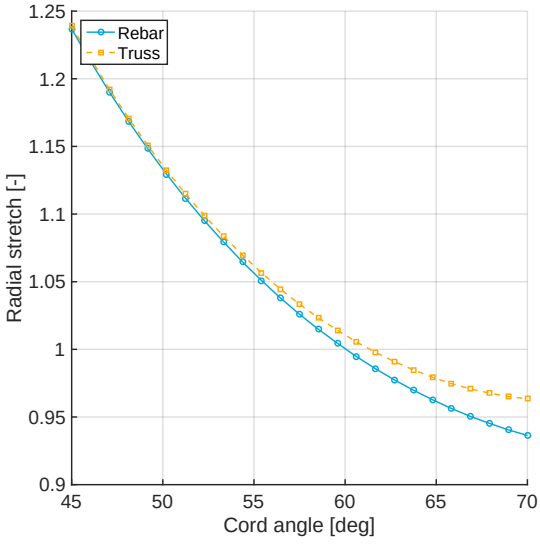

(c) Radial stretch at the axial middle (z = 500 mm)
Expansion > 1 > contraction

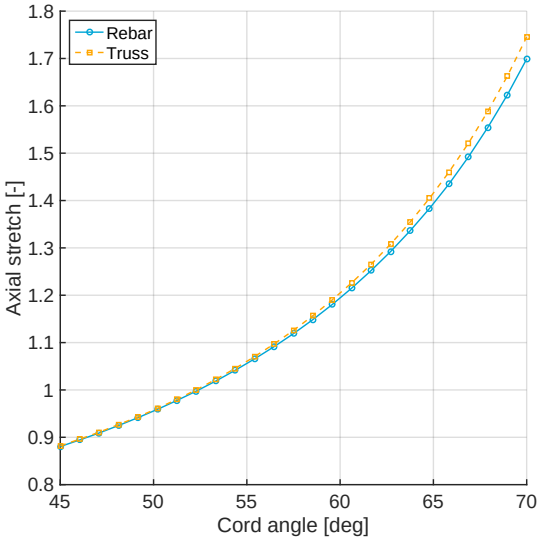

(d) Axial stretch along the z-axis
Expansion > 1 > contraction

Figure 6.5: Relation between the cord angle and the structural response in a MLC with a uniform cord angle (p = 30 bar)

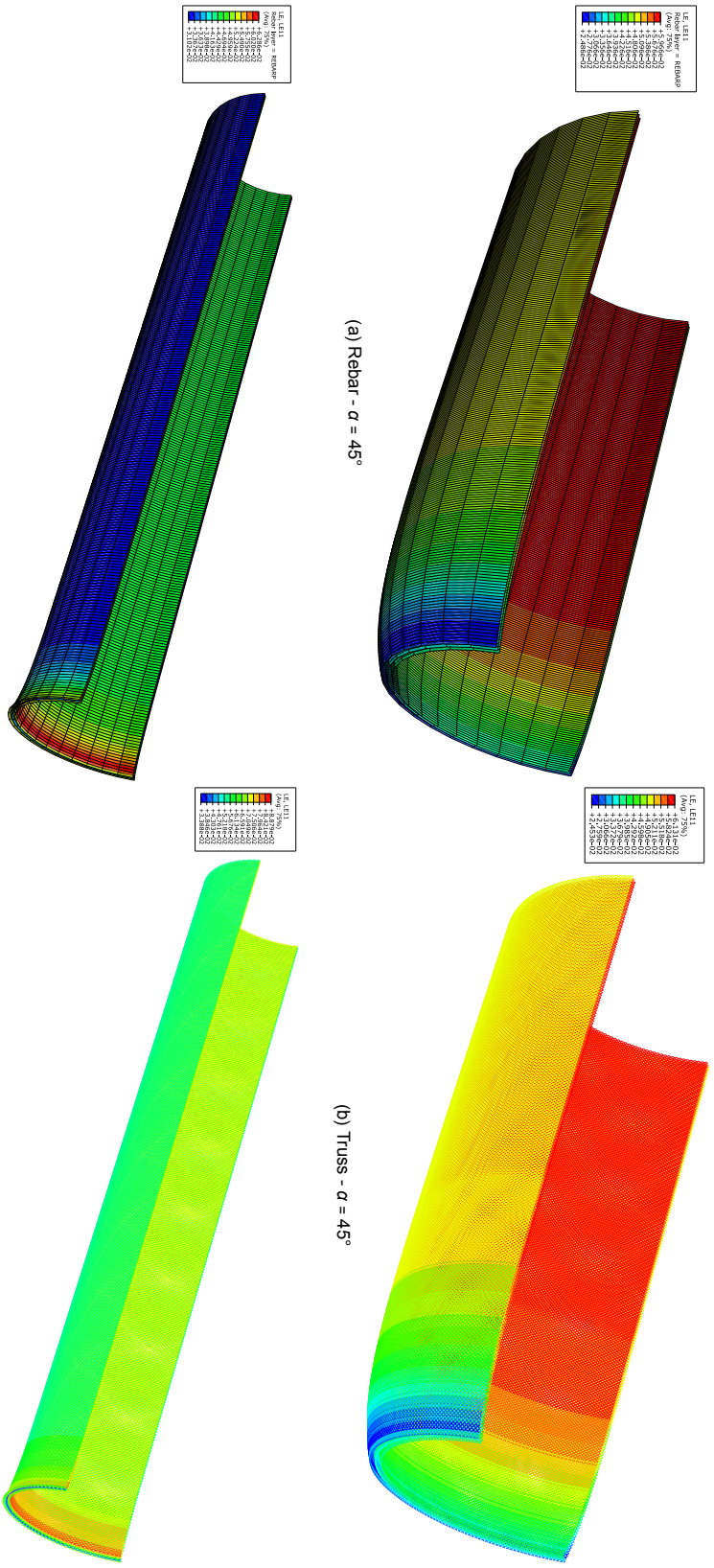

(a) Rebar - α = 45°

(b) Truss - α = 45°

(c) Rebar - α = 70°

(d) Truss - α = 70°

Figure 6.6: Strain distribution in uniform cord angle MLC

6.6.1. Peak cord strain

Figure 6.7 shows the peak strain that occurs in the MLC depending on the cord angles of the inner and outer layers. Comparatively to Figure 6.5a, the rebar and truss models show good agreement when the average angle $\tilde{\alpha}$ (i.e. the cord angle of the middle layer) is smaller than 58°, whereas the strains diverge with larger angles. Note that the designs of the constant angle study in Section 6.5 can be found on the south west - north east diagonal, where the inner and outer angle are equal. Since the truss model showed significantly higher strains at large cord angles in Figure 6.5a, the valley that can be observed in Figure 6.7a is not as pronounced in Figure 6.7b. In general both models show a similar trend, where two local minima are contoured. The valleys in the design space run along both diagonals, which represent a constant average cord angle ($\partial\alpha_I/\partial\alpha_O = -1$) and a constant angle difference between the inner and outer layers ($\partial\alpha_I/\partial\alpha_O = 1$).

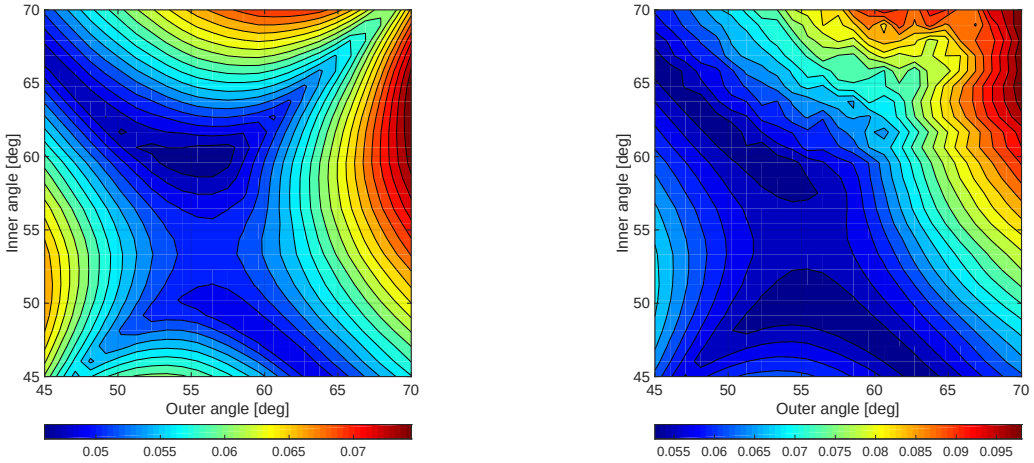

(a) Rebar

(b) Truss

Figure 6.7: Peak strain in all layers [-]

Figure 6.8 indicates in which layer the peak strains of Figure 6.7, respectively, occur. At first glance, the rebar models have majority of the peak strains happen in the inner or outer layers. The boundaries between these two regions trace the valleys that can be seen in Figure 6.7a, indicating that the structural efficiency increases (i.e. the global peak strain decreases since the total load is distributed more efficiently) when the peak strain in all layers is near equal. This strain is more likely to occur on the inner cord layer, as a result of the hoop stress being the largest on the inner surface of a thick-walled cylinder. In order to force the peak strain to occur on the outer layer, the outer layer should have a cord angle closer to the neutral angle than the inner layer. The zones in Figure 6.8 where the outer layer (layer 3) experiences the largest strain roughly satisfy the conditions: $\alpha_I > \alpha_O > \alpha_n$ or $\alpha_I < \alpha_O < \alpha_n$. The same relations between the peak strain and the layer in which they occur can be recognised in Figures 6.7b and 6.8b, albeit less pronounced in the regions with high average cord angle.

The axial location at which the peak cord strain is achieved is shown in Figure 6.9. These figures show that the binary-like behaviour observed in the uniform cord angle case (Figure 6.5b) is still present. At first glance the front between peak strain occurring near the edge ($z = 0$ mm) and the middle ($z = 500$ mm) runs along the line where $\tilde{\alpha} = 58°$, which is the two-dimensional equivalent of Figure 6.5b. The location of peak strain appears to be predominantly affected by the average initial cord angle, while generally being unaffected by radial angle variation. The front between the two extreme locations is disturbed where the peak strains in all layers are quasi equal (Figure 6.8a), indicating that at high structural efficiency (equal load distribution) the location of the peak strain becomes less certain (even undetermined in the ideal case).

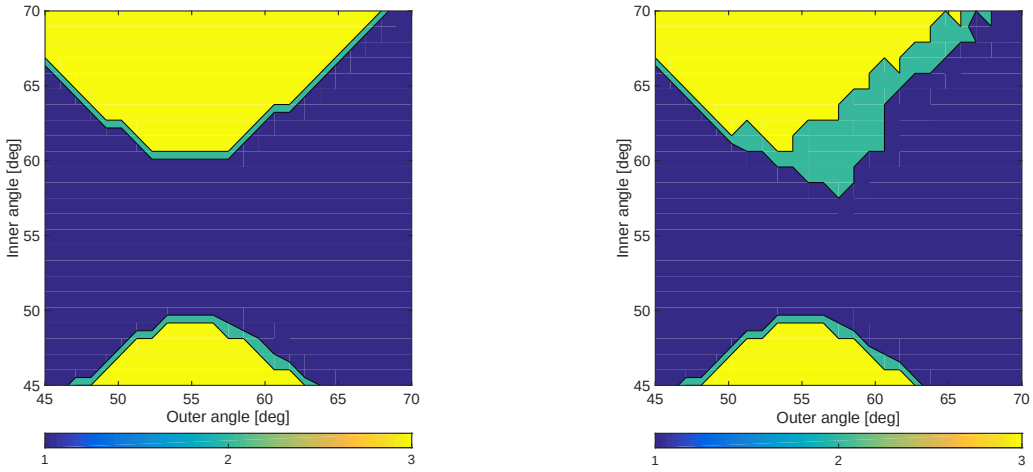

(a) Rebar (b) Truss

Figure 6.8: Cord layer of max. strain (1 = inner; 2 = middle; 3 = outer)

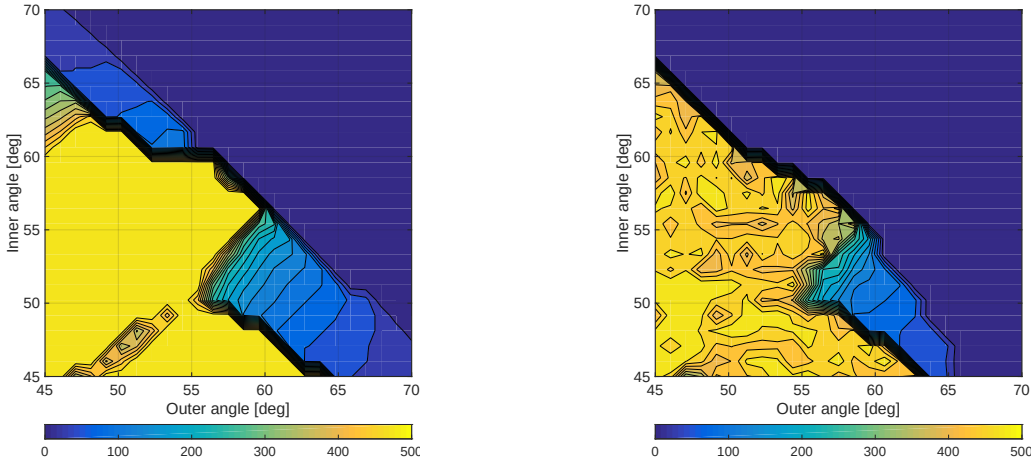

(a) Rebar (b) Truss

Figure 6.9: Axial location of max. strain in all layers [mm]

6.6.2. Stretch ratios

Figures 6.10 and 6.11 show the radial and axial stretches experienced by the MLC designs, as well as the average final cord angle upon inflation to 30 bar. Where there is some distinguishable difference between the strains reported by the rebar and truss models, there is good agreement in the deformation experienced by both models (similar to Figures 6.5c and 6.5d). Both the radial and axial stretches have their primary gradient along the uniform angle diagonal ($\alpha_O = \alpha_I = 45$ degree to $\alpha_O = \alpha_I = 70$ degree). The magnitude of these stretches is primarily determined by the average cord angle in the MLC, where the angle that has the largest difference to the neutral angle dominates the deformation as the average angle increases. Interestingly there is no importance to whether the inner or outer cord layer is more dominant. The distribution of the stretch ratios over the design space, the two-dimensional equivalent of Figures 6.5c and 6.5d, is in agreement with the braid deformation principles where difference of the cord angle with the neutral angle determines the phase I deformation shape [33].

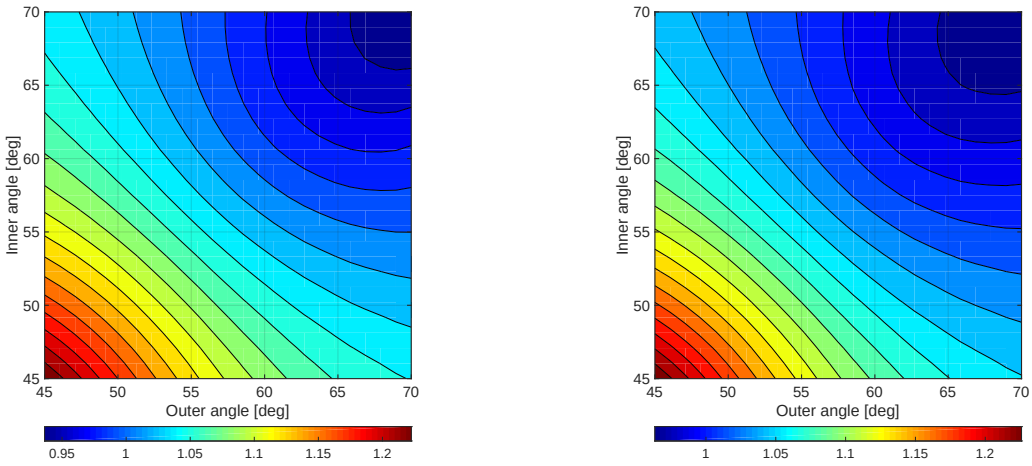

(a) Rebar (b) Truss

Figure 6.10: Radial stretch at the axial centre (z = 500 mm) [-]

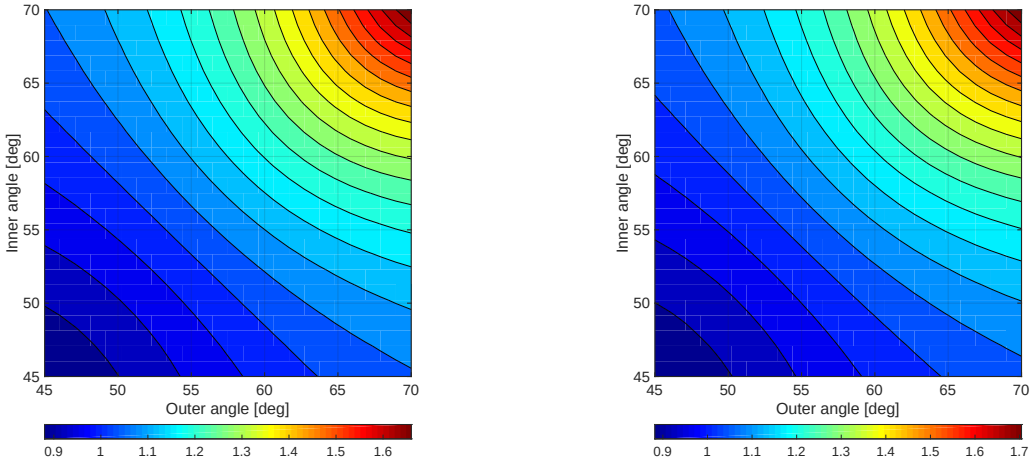

(a) Rebar (b) Truss

Figure 6.11: Axial stretch along the z-axis [-]

The average final cord angle (measured at the axial middle of the MLC) is displayed in Figure 6.12, which shows a dependency on the average initial cord angle where the reinforcement layers tend to rotate towards the neutral angle during phase I deformation. Along the uniform angle line ($\alpha_I = \alpha_O$) the average final cord angle is closer to the neutral angle than other design with identical average initial cord angle. A smaller difference between initial cord angles in the inner and outer layers allows for more cord rotation during phase I deformation. As a results the loads are distributed more evenly throughout the structure.

6.6.3. Analysis time

The FEAs discussed above were performed on the HPC cluster of the *Faculty of Aerospace Engineering*, where four node parallelization was used to decrease analysis time. At the end of each FEA the wall clock time as reported by ABAQUS was registered, which is the real-life time during which the analysis process occupied the designated Central Processing Units (CPUs) to pre-process the input file and perform the FEA. On average the rebar model required 40 s, compared to the 176 s wall clock time required by the truss model. Figure 6.13 shows a histogram of the reported analysis times.

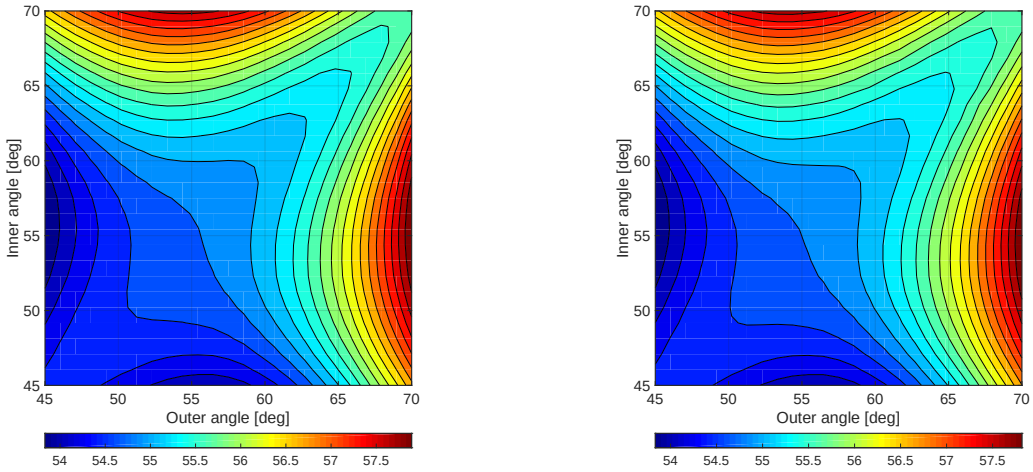

(a) Rebar (b) Truss

Figure 6.12: Average final cord angle [deg]

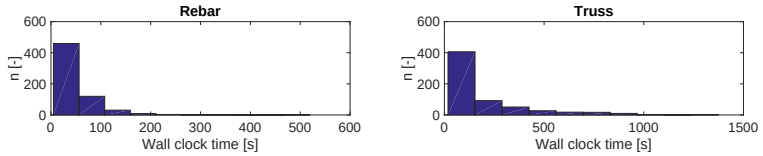

Figure 6.13: Wall clock times reported by ABAQUS

6.7. Axial angle variation

Where radial angle variation primarily influences the stress distribution through the thickness (see Section 6.6.1) and allows for improvement of the structural efficiency, the location of peak strain is determined generally by the average cord angle $\bar{\alpha}$. While studies have been performed to analyse the relation between stacking sequence and stress distribution in anisotropic pressure vessels [4, 35, 46, 47], axial angle variation is often not included in the study because the location of failure is generally not of high importance. Furthermore they are often manufactured using angle plies or constant angle winding, meaning axial angle variation is not achievable. TANIQ, however, is capable of accurate cord placement during friction controlled winding, allowing the axial variation of the cord angle. Since the burst failure location of the LBH is not allowed to be near the coupling for the safety of nearby operators, axial angle variation could prove useful to force the peak strain towards the cylindrical section of the LBH. The design space is kept consistent with that of Sections 6.5 and 6.6, where the angles at the edge α_E (z = 0 mm) and the centre α_C (z = 500 mm) are varied from 45° to 70°.

6.7.1. Peak cord strain

Figure 6.14 shows the peak strain occurring in the MLC depending on the cord angles at the centre and edge. Similarly to Section 6.5 the strain is the highest on the inner cord layer for all designs, indicating no influence between axial angle variation and the stress distribution through the thickness.

When both specified cord angles are smaller than the neutral angle, the strain seems to be dependent on a weighted average of the specified cord angles. The equal peak strain levels follow $\partial\alpha_C/\partial\alpha_E = -0.4$, indicating the cord angle in the centre has a larger influence on the peak strain. The smaller effect of the cord angle at the edges is a consequence of the MLC being clamped at the edges, which restricts cord rotation and consequent load redistribution during phase I deformation.

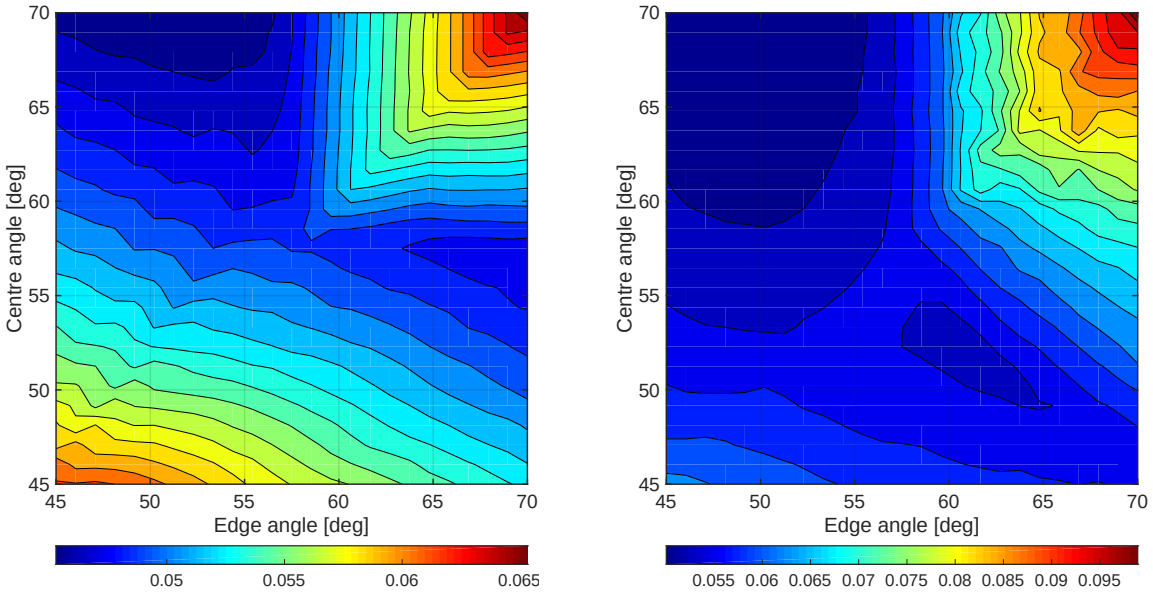

(a) Rebar (b) Truss

Figure 6.14: Peak strain in all layers [-]

On the other had, when both specified angles are larger than the neutral angle, radial contraction and axial expansion occur during phase I deformation. In this region of the design space the peak strain is defined by the smaller angle, represented by the horizontal and vertical gradients when $\alpha_E > \alpha_C$ and $\alpha_C > \alpha_E$, respectively. Figure 6.19 shows the strain distributions of three design with equal peak strain, yet different angle specifications. In all three cases the peak strain occurs towards the clamped edge, consistent with the behaviour observed in Figures 6.5b and 6.9a when the $\bar{\alpha} > 58°$. The MLC in Figure 6.19a has a uniform cord angle of 61.7°. The strain is relatively constant in axial direction, with an increase near the clamped edge. In Figures 6.19b and 6.19c the cord angle is increased to 70° at the centre and edge, respectively. The strains are observed to be lower in the regions with larger initial cord angles, whereas the peak strain near the edge remains unchanged.

The axial location at which the peak strain occurs is displayed in Figure 6.15, where the same binary-like behaviour observed in Figures 6.5b and 6.9 is recognizable. Overall the truss and rebar models show good agreement, with the exception of one region. The following regions can be identified (starting in the top right corner, going counterclockwise):

- $\alpha_C, \alpha_E > \alpha_n$ The large average cord angle results in radial contraction and axial expansion during phase I deformation. Consistent with the observations in Figures 6.5b and 6.9, the peak strain occurs near the clamped edge.
- $\alpha_E < \alpha_n, \alpha_E < \alpha_C$ When the cord angle at the clamped edge is smaller than both the neutral angle and the centre cord angle, the peak strain occurs primarily towards the clamped edge. As difference between α_E and α_C decreases, however, the peak strain location shifts gradually towards the centre.
- $\alpha_C, \bar{\alpha} < \alpha_n$ With a cord angle at the centre and average cord angle in the MLC being smaller than the neutral angle, radial expansion and axial contraction occur during phase I deformation. Consistently with the observations in Figures 6.5b and 6.9, the peak strain occurs near the axial centre.

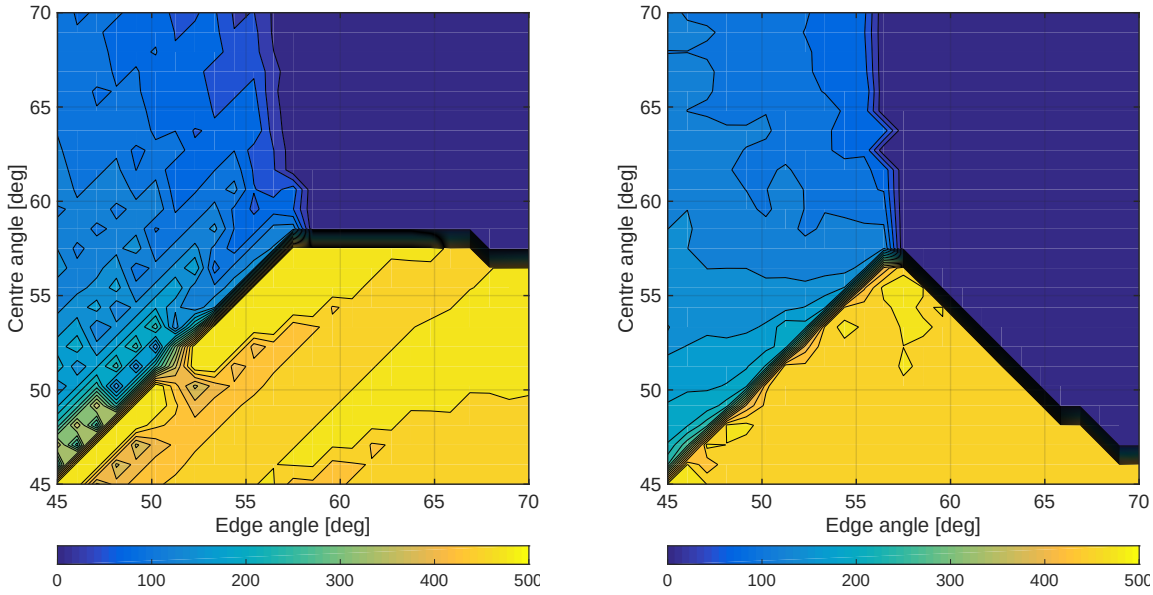

(a) Rebar

(b) Truss

Figure 6.15: Axial location of max. strain in all layers [mm]

- $\bar{\alpha} > \alpha_n, \alpha_C < \alpha_n$ In this region the rebar and truss models predict opposing locations of peak strain, at the centre and the edge respectively. Figure 6.18 shows the strain distribution in the rebar and truss model of a MLC with $\alpha_E = 70°$ and $\alpha_C = 51.3°$. The axial strain distributions are comparable to one another, decreasing from the centre towards the edge (where the cord angle is higher). The difference, however, is that the truss model predicts a stress concentration at 5 mm from the edge.

6.7.2. Stretch ratios

The radial stretch, measured at the centre of the hose, depending on axial angle variation is shown in Figure 6.16. The influence of the cord angle at the clamped edge is minimal, with a large angle reducing the radial stretch slightly. Logically, the angle at the axial centre primarily dictates the radial stretch according to phase I deformation principles. The axial stretch, similarly to Sections 6.5 and 6.6, is primarily determined by the average cord angle.

6.7.3. Analysis time

The FEAs discussed above were performed on the HPC cluster of the *Faculty of Aerospace Engineering*, where four node parallelization was used to decrease analysis time. At the end of each FEA the wall clock time as reported by ABAQUS was registered, which is the real-life time during which the analyses process occupied the designated CPUs to pre-process the input file and perform the FEA. On average the rebar model required 79 s, compared to the 218 s wall clock time required by the truss model. Figure 6.17 shows a histogram of the reported analysis times.

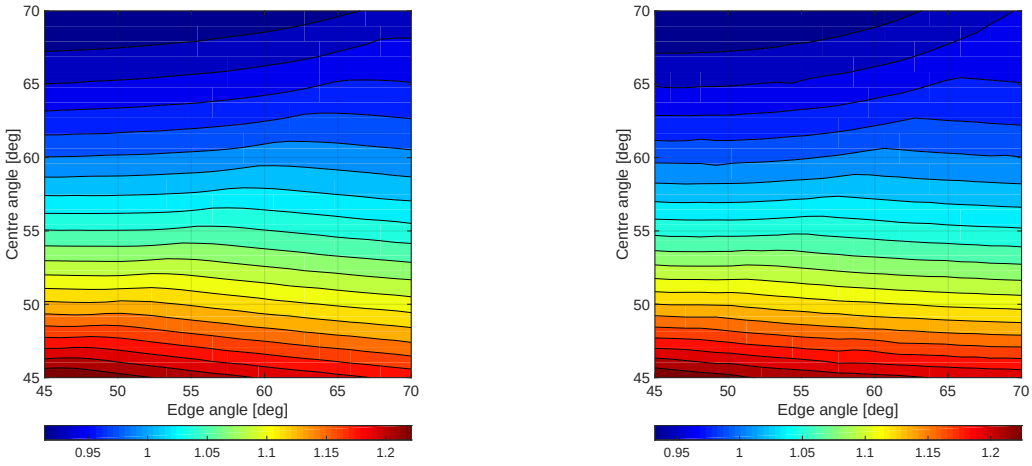

(a) Rebar (b) Truss

Figure 6.16: Radial stretch at the axial centre (z = 500 mm) [-]

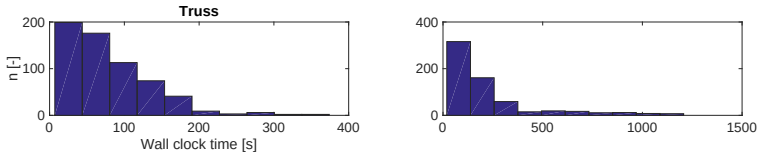

Figure 6.17: Wall clock times reported by ABAQUS

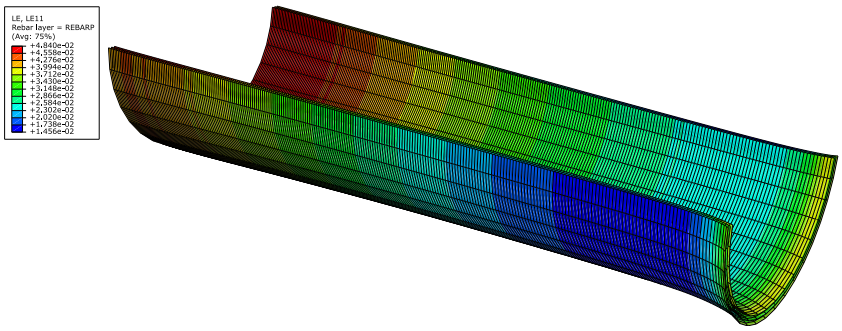

(a) Rebar

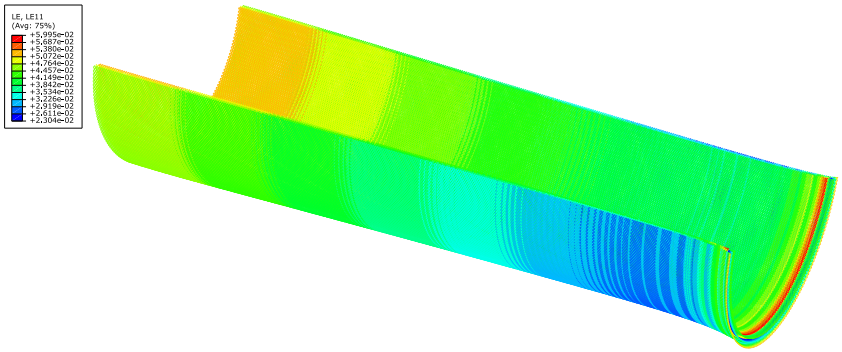

(b) Truss

Figure 6.18: Strain distribution of MLC with α_E = 70°, α_C = 51.3°

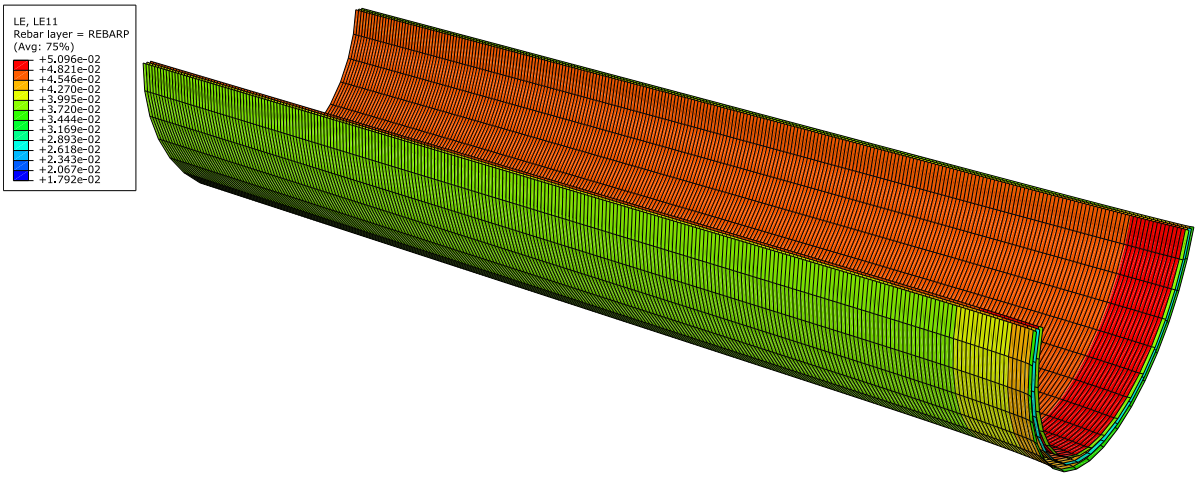

(a) α_E = 61.7°, α_C = 61.7°

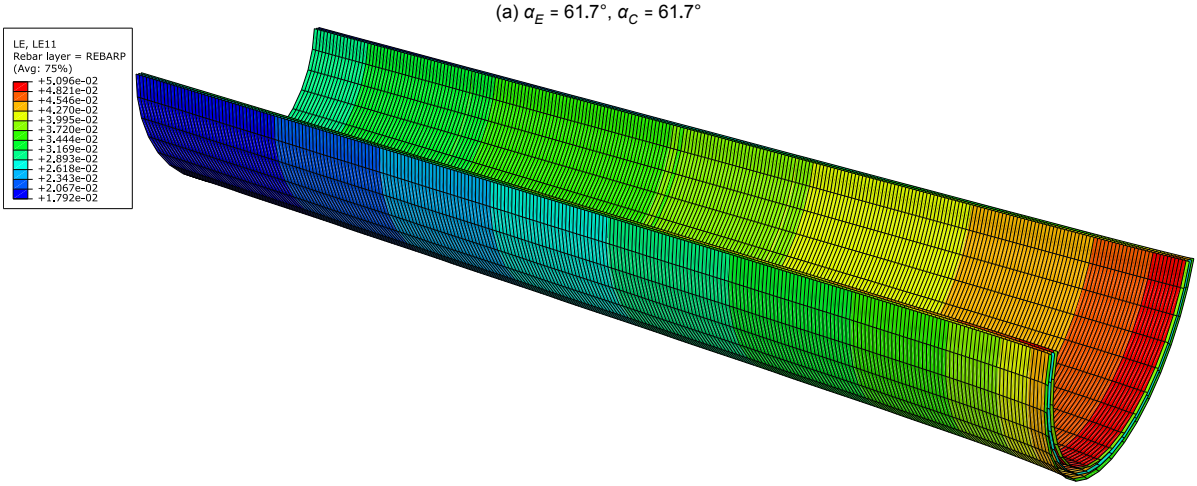

(b) α_E = 61.7°, α_C = 70°

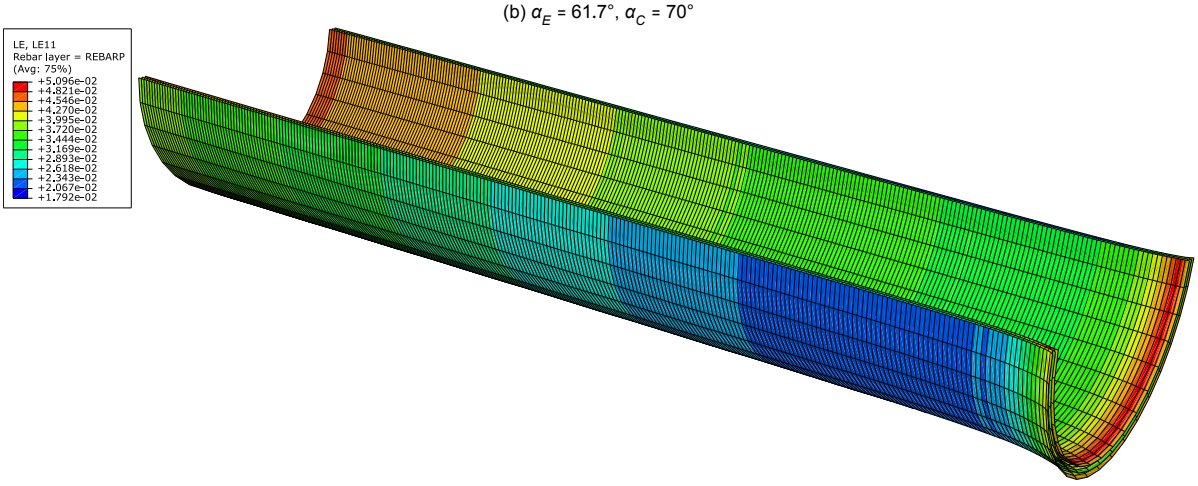

(c) α_E = 70°, α_C = 61.7°

Figure 6.19: Strain distribution in rebar MLC models with equal peak strain $\alpha_C, \alpha_E > \alpha_n$

7

Reinforcement Angle Optimisation of Multilayered Cord-rubber Cylinders

The previous chapter covered the Finite Element Analyses (FEAs) of Multilayered Cylinders (MLCs) with parametrised cord angles. The rebar and truss methods were compared to each other and while differences existed in the peak strain levels reported by both methods, they showed good agreement regarding the deformation shapes and strain distributions. Additionally the rebar method indicated smoother and better defined relations between the cord angles and various output metrics, while being 70 % faster than the (baseline) truss method.

The cord angle optimisation of the MLC will be performed using this newly developed rebar method, because the significant time saving this method offers reduces the total time an optimisation run would take when FEA is integrated directly into the fitness calculation. A Genetic Algorithm (GA) was selected as the optimisation method because of its robustness and resilience towards local minima (discussed in Section 3.2.2), since two regions with a local minimum were observed in Section 6.6.1. Other evolutionary algorithms such as particle swarm or ant colony optimisation could also be used, but are outside the scope of this thesis.

For development purposes and to decouple the FEAs from the optimisation algorithm, a surrogate model will be generated from a four-dimensional dataset. This surrogate model allows for the GA to be executed in rapid succession by substituting the expensive FEAs in the fitness evaluation. While a large number of FEAs is required initially to construct a representative data set, time and resources are saved during each GA optimisation. Section 7.1 covers the implementation and verification of the surrogate model. Subsequently Section 7.2 discusses the results of the GA applied on the surrogate model.

7.1. Surrogate modelling

The Design and Analysis of Computer Experiments (DACE) toolbox developed by Lophaven et al. [13] provides a methodology for creation of a surrogate model in MATLAB. The toolbox relates inputs and outputs through regression on the normalised data. The model solves a generalised least squares minimisation problem to obtain the regression function parameters. These functions form the DACE model and can be used after determination of the coefficients to predict values based for given combinations of input parameters [56].

7.1.1. DACE model

To fit the DACE model a dataset of 2000 designs was created using Latin hypercube sampling in four dimensions. This method, described by McKay et al. [57], is a statistical method for generating a near-random multidimensional sample of parameter values. It ensures the entire range of each parameter is represented in the dataset and provides better coverage than orthogonal sampling with increasing design space dimension [13]. The four input parameters are the angles presented in Section 6.3, which are given the following numbering:

Table 7.1: DACE model input parameter numbering of the cord angle specifications

	Axial	
Radial	Edge	Centre
Outer	α_1	α_3
Inner	α_2	α_4

A quadratic regression function is used to correlate the input parameters with the peak strain of each design point. This function is shown in Equation (7.1), where $\boldsymbol{\alpha}$ is a vector of the input parameters α_i, $\boldsymbol{\beta}$ a coefficient vector with elements β_i, and $\boldsymbol{\beta}_U$ the upper triangle of a coefficient matrix with entries β_{ij}.

$$f = 1 + \boldsymbol{\beta}^T\boldsymbol{\alpha} + \boldsymbol{\alpha}^T\boldsymbol{\beta}_U\boldsymbol{\alpha} \tag{7.1}$$

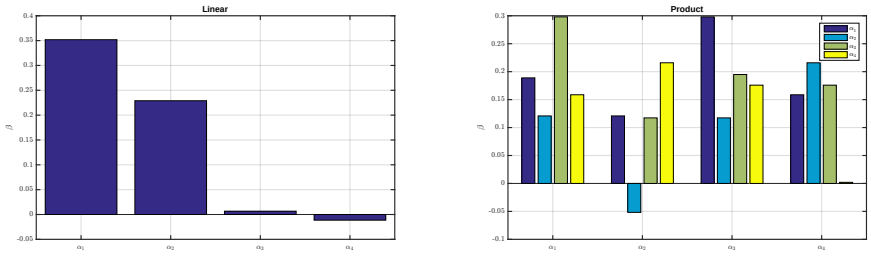

Figure 7.1: Regression coefficients of the 4 parameter DACE model fitted with 2000 points

The quadratic regression function therefore has 15 coefficients, four linear (β_i) and 11 quadratic (β_{ij}). Since the regression functions finds the least square fit between the normalised input and output data, the coefficients do not indicate an absolute value contribution of the input parameters to the predicted strain values. Instead these coefficients show the relative influence of the input parameters (or products thereof), shown in Figure 7.1. The linear coefficients show that the cord angles at the edge have a relatively large contribution to the peak strain compared to the angles at the centre, whereas the product coefficients indicate a larger contribution of the product of the angles on the outer layer.

7.1.2. Model error

To assess the accuracy of the DACE model fit with 2000 data points, a comparison is made with the data sets generated for the radial and axial angle variation studies (Sections 6.6 and 6.7 respectively). In both cases FEAs were performed on a 25 × 25 grid, resulting in two data sets of 625 points each.

The DACE model can be used to predict the peak strain distribution in the two-dimensional design space with constant cord angle layers (studied in Section 6.6). The cord angles are specified on the outer (α_O) and inner (α_I) layer, represented by the input vector:

$$\boldsymbol{\alpha} = \left[\alpha_O\ \alpha_I\ \alpha_O\ \alpha_I\right]^T$$

The two-dimensionally projected DACE model in Figure 7.2 shows good agreement with the FEA data set, where the distribution of peak strain throughout the design space is comparable. The mean and maximum absolute prediction errors are 0.0008 and 0.0063, respectively. The mean and maximum relative errors are 1.36 % and 9.44 %, respectively. These maxima are observed in Figure 7.3 to be the largest near the edges of the design space, in the (45,45) and (70,70) corners particularly.

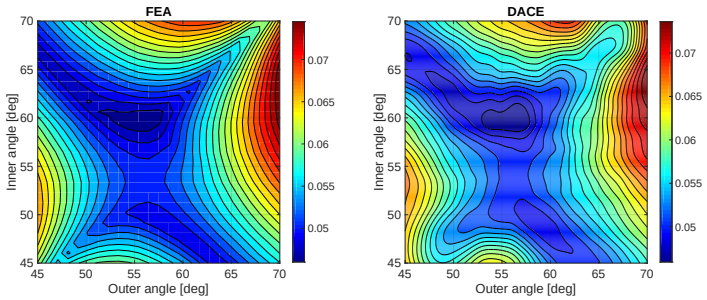

Figure 7.2: Peak strains obtained from FEA (Section 6.6) and 2D projection of the DACE model

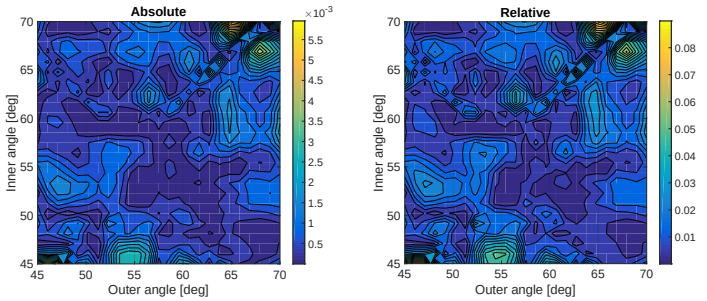

Figure 7.3: Absolute and relative error of DACE model predictions vs FEA (Section 6.6)

Consequentially the design space used in the axial angle variation, with angles specified at the edge (α_E) and axial centre (α_C), can be emulated by the DACE model through an input vector

$$\boldsymbol{\alpha} = \left[\alpha_E \alpha_E \alpha_C \alpha_C\right]^T$$

The predicted peak strain distribution shows waviness compared to the FEA reported values in Figure 7.4. Especially the well defined corner in the FEA data where $\alpha_E, \alpha_C > 58°$ is not as pronounced in the DACE prediction. The mean and maximum absolute errors between the predicted and FEA strains are 0.0007 and 0.0060, respectively, whereas the mean and maximum relative errors are 1.30 % and 12.66 %, respectively. The errors are larger towards the equal angle corners and near the edges of the design space shown in Figure 7.4, while being small towards the centre of the design space.

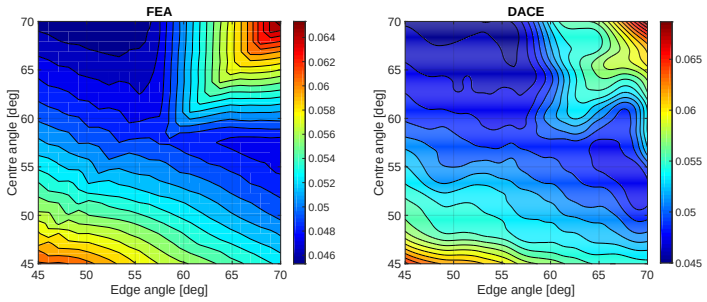

Figure 7.4: Peak strains obtained from FEA (Section 6.7) and predicted by the DACE model

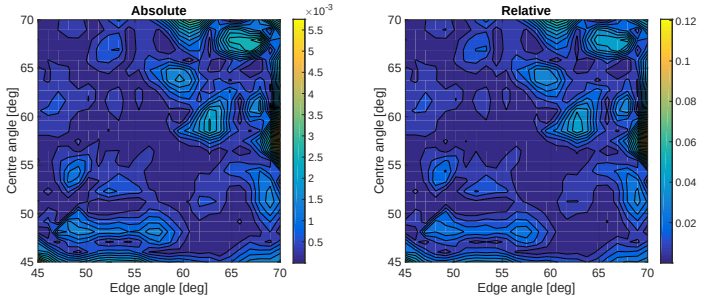

Figure 7.5: Absolute and relative error of DACE model predictions vs FEA (Section 6.7)

7.2. Genetic algorithm

The *Global Optimization Toolbox* in MATLAB provides functions that search for global solutions to problems that contain multiple maxima or minima[1]. One of such optimisation functions is the GA solver (discussed in Section 3.2.2), a robust evolutionary optimisation algorithm that randomly searches the entire design space. The randomness provided by mutation and crossover of the design parameters reduces the chance of the search function converging on a local minimum.

The `ga` function is able to perform an optimisation using both real and integer parameters. Restricting the cord angle inputs to integer values has the potential to decrease the number of function calls the GA needs to convergence on the global minimum. Furthermore the accuracy achieved during the manufacturing process is 1°, meaning that allowing the specified cord angles to be non-integer values is not worth the additional computational cost nor physically feasible.

The default GA options set by MATLAB were used, which differ slightly between the real and integer problem. A population size of 40 was used, with the initial population being randomly selected with a uniform distribution in the four-dimensional design space.

7.2.1. Projected radial angle variation

In order to allow visual assessment of the GA performance in identifying the lowest peak strain value in a given design space, the algorithm was tested in the 2D constant angle design space (Section 6.6) emulated by the 4D DACE model as shown in Figure 7.2. Consistency of the GA algorithm was tested by performing 1000 optimisation runs during two series: one where the input parameters were allowed to be real values ($\alpha_i \in \mathbb{R}$) and one where the cord angle inputs were limited to integer numbers ($\alpha_i \in \mathbb{N}$).

[1] `https://www.mathworks.com/products/global-optimization.html`

Since the DACE model errors were largest near the edges of the design space, the allowed range of the cord angle parameters was limited to $[46, 69]$, lowering the mean and maximum error to 1.23 % and 6.53 %, respectively. The performance of both GA approaches was consistent in identifying the cord angle combination resulting in minimum peak strain for a MLC with constant angle reinforcement layers. Comparing the results of the real-valued angles with the integer-limited ones in Figure 7.6, where the bins of the former have a 1° width. The integer-limited GA is seen to indicate the optimal angle combination with a 99.9 % success rate, compared to 93.5 % with real-valued parameters. In the latter case the number of combinations is quasi-infinite, with the decimal precision dictated by the convergence criteria of the GA, whereas in the integer-limited scenario this number is limited effectively to 576 (24^2) design points.

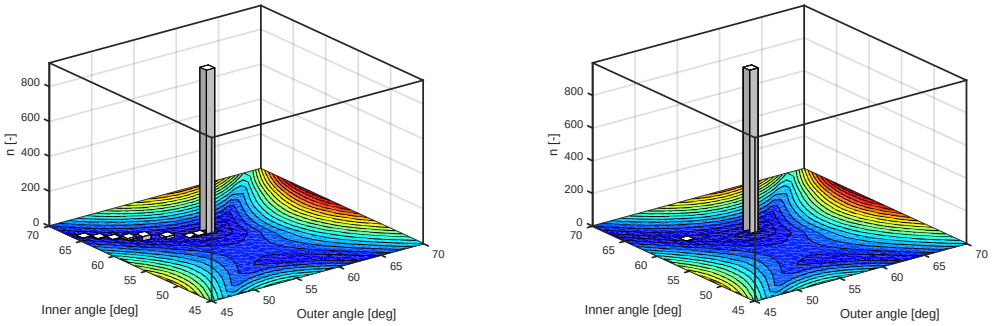

(a) $\alpha_i \in \mathbb{R},\ \Delta\alpha_i = 1°$ (b) $\alpha_i \in \mathbb{N}$

Figure 7.6: GA results (n = 1000) on emulated 2D (constant angle) space from 4D DACE model, shown on FEA 2D space (Section 6.6)

The 935 design points identified by the real-valued GA follow a normal distribution (shown in Figure 7.7) with mean 56.110° and 59.678° and standard deviation of 0.015° and 0.011° for the outer and inner cord layer angle, respectively. The peak strains corresponding to these points have a mean value of 0.0459 with a 2×10^{-6} standard deviation. The integer-limited GA indicated 56° and 60° as the optimal cord angles on the outer and inner layers, respectively, corresponding with a peak strain value of 0.0461.

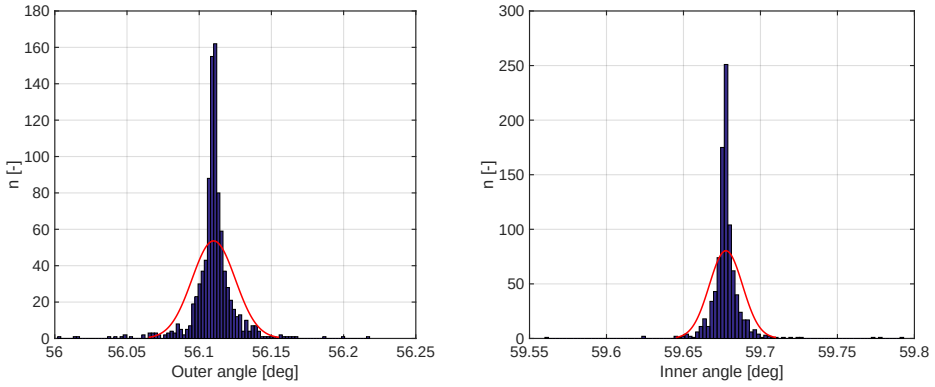

Figure 7.7: Distribution of the real-valued GA solutions near the optimal configuration

7.2.2. Four parameter optimisation

Also for the four-dimensional DACE model design space two sets of 100 GA runs were performed, with real and integer-limited parameters in $[46, 69]$ (331 776 (24^4) design points in the latter case). The histograms of the optimal parameter distributions in Figure 7.8 indicate a more consistent identification of the configuration with a lowest peak strain with integer-limited parameters. It identified the cord angle combination shown in Table 7.2 with a 86 % success rate. The real-valued GA, however, managed to identify the optimal configuration of which the parameter distribution is shown in Figure 7.8c only 45 % of the time. Taking into account the manufacturing limitations on the required cord angle accuracy, it is therefore beneficial to restrict these angles to integer values.

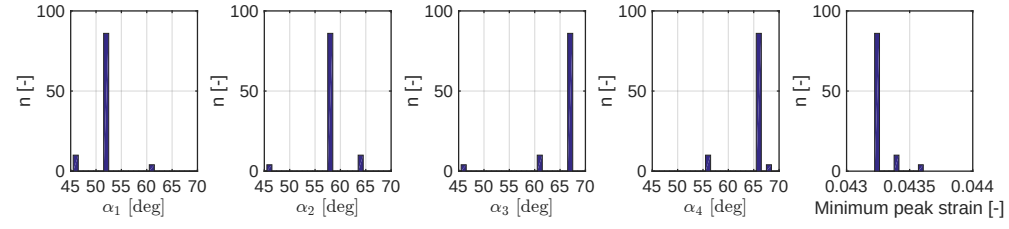

(a) $\alpha_i \in \mathbb{N}$

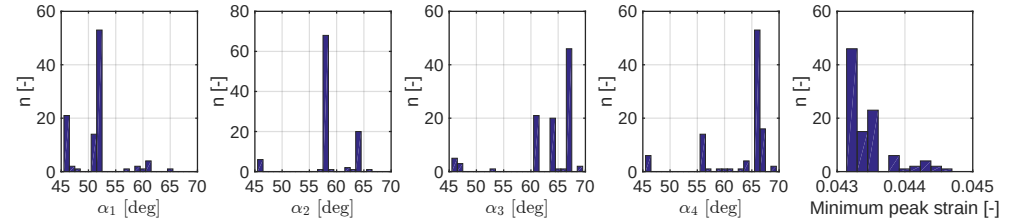

(b) $\alpha_i \in \mathbb{R}$

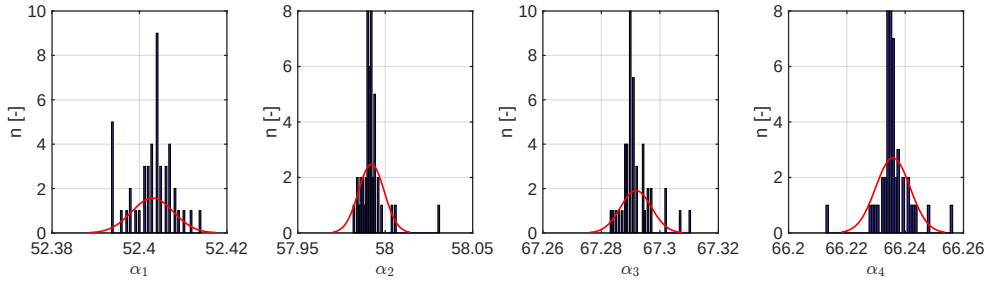

(c) Design points near the optimal configuration ($\alpha_i \in \mathbb{R}$)

Figure 7.8: Cord angle distribution of GA results (n = 100) on the 4D DACE model

Table 7.2: Optimal cord angle configuration for the MLC ($\alpha_i \in \mathbb{N}$) [deg]

	Axial	
Radial	Edge	Centre
Outer	52	67
Inner	58	66

In order to verify the findings of the GA, an FEA is performed on a MLC rebar model with the indicated optimal cord angle configuration. The DACE surrogate model predicts a peak strain of 0.0434 at the design point indicated in Table 7.2. An FEA of this configuration was performed in ABAQUS/2018, with two CPU parallelisation. The strain distribution shown in Figure 7.9 has a maximum value of 0.0439 (0.04301 logarithmic strain) at 5 % axial length (50 mm) from the edge. Interestingly, this optimal cord angle configuration does no have a uniform load distribution throughout the reinforcement layers, with a minimum strain of 0.0192 on the outer layer at the axial centre.

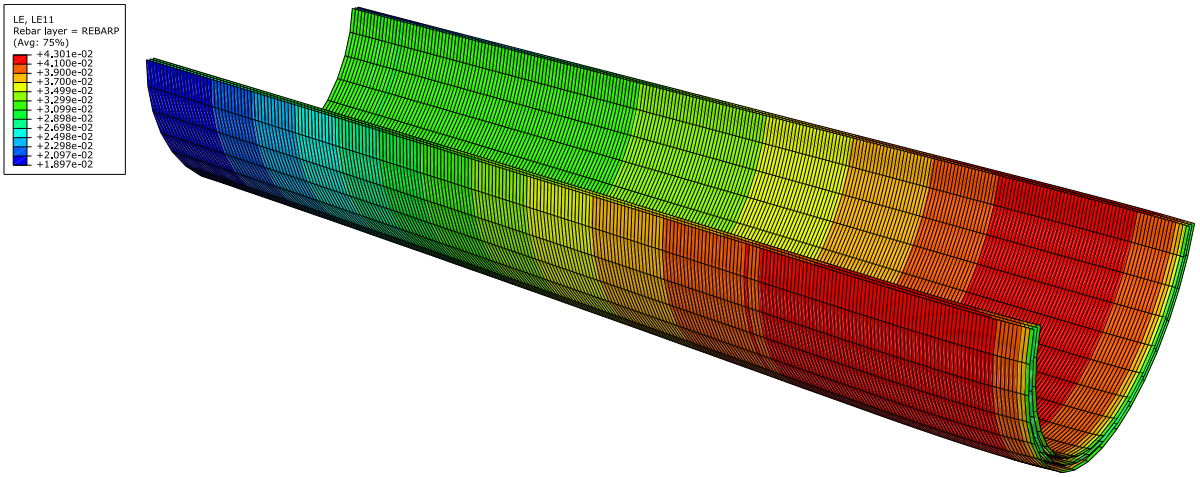

Figure 7.9: Strain distribution in the MLC with optimal cord angle configuration according to the 4D GA optimisation
Left side: centre, right side: edge

III

Large Bore Hose

8

Finite Element Analysis of Multilayered Cord-Rubber Hoses

The rebar models in Sections 6.6 and 6.7 showed well defined trends in their strain and deformation distributions, as well as a computational time saving of 70 % over the truss models. Consequently the rebar method is used to create a parametrised Finite Element (FE) model of the Large Bore Hose (LBH).

Sections 8.1 and 8.2 present the geometry and material data used in the LBH FE models. Comparatively to the Multilayered Cylinder (MLC), four angles will be used to define the cord angle distribution throughout the reinforcement layers of the LBH. The definition of these parameters and resulting cord angle distribution is discussed in Section 8.3. Subsequently the FE mesh is covered in Section 8.4, based on the axisymmetric geometry of the LBH.

8.1. Geometry

The LBH has a face-to-face length of 6 m and an internal diameter of 406 mm. It consists of six parallel cord layers spaced evenly between the inner and outer rubber layers. An axisymmetric sketch of the LBH profile is shown in Figure 8.1, where several axial points of interest are indicated.

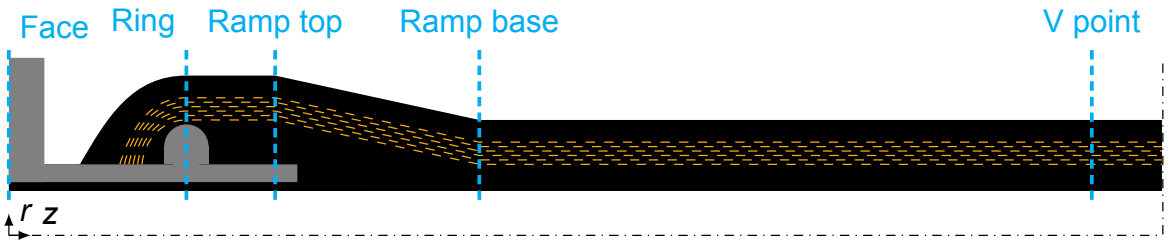

Figure 8.1: Axisymmetric sketch of the parametric LBH FE model

8.2. Material data

The rubber is modelled using the Ogden material model ($N = 3$, see Section 2.2.1) with the parameters shown in Table 8.1a, which were obtained by evaluating uniaxial tensile test data using ABAQUS/Standard. This material model is stable in the regions indicated in Table 8.1b (i.e. where $\partial\sigma/\partial\varepsilon > 0$). The uniaxial test data and corresponding Ogden fit are shown in Figure 8.2a.

The cord material are Polyethylene Terephthalate (PET) yarns, of which the uniaxial tensile test data is shown in Figure 8.2b. Since PET is hyperelastic, the Marlow material model is used provided with this test data.

Table 8.1: Ogden material model properties

(a) Parameters

n	1	2	3
μ_n	-0.171	0.479×10^{-3}	0.706
α_n	2.365	9.891	1.590

(b) Permitted strain ranges

Strain mode	Min. compression	Max. tension
Uniaxial	-0.075	2.660
Biaxial	-0.477	0.040
Planar	-0.074	0.080

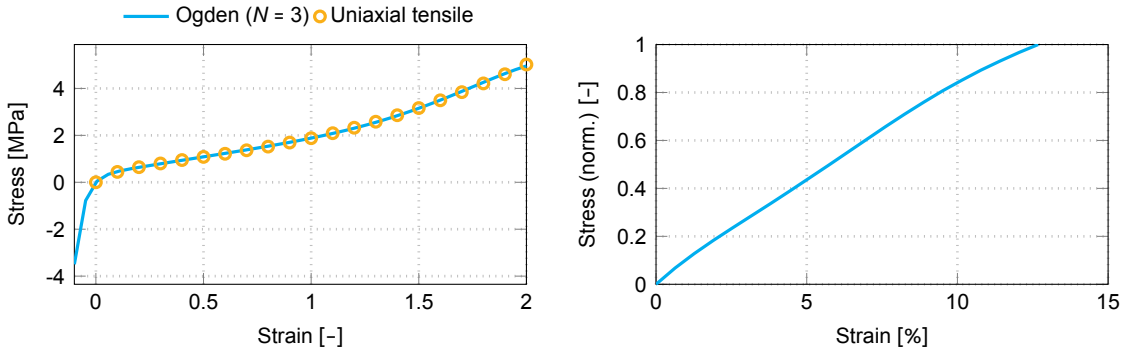

(a) Rubber uniaxial tensile test data and Ogden fit

(b) Cord uniaxial tensile data

Figure 8.2: Material data used in the LBH FEA

8.3. Angle definition and winding parameters

The parametrised model of the MLC had four input parameters that specified the cord angle variation both axially and radially. Furthermore the Design and Analysis of Computer Experiments (DACE) model and subsequent optimisation were proven in a four-dimensional design space. Therefore four input parameters were selected for the LBH as well. The challenge, however, is that the LBH is a more complex structure and traditionally has its cord angles specified on three axial locations (indicated in Figure 8.1): the ramp top (RT), the ramp base (RB), and the hose body (V-point). If the cord angle on the outer and inner layers were to be specified in each of these locations, six input parameters would be required. In order to reduce the cord angle parameters, these two parameters had to be related to the others. Since there are three axial locations of interest, the angles at the ramp base are made dependent on those at the ramp top and V-point.

Since the cord angles are constant both between left of the ramp top (w.r.t. to Figure 8.1) and in the hose body, the slope of the angle distribution was enforced to be zero at these points to ensure a smooth stiffness transition (prevent local stress concentrations). The cord angle distribution in a reinforcement layer between the ramp top (z_{RT}) and V-point (z_V) with angles α_{RB} and α_V at these points, respectively, is given by Equation (8.1). An example of this angle variation is shown in Figure 8.3, based on the input parameters defined in Table 8.2.

$$\alpha(z) = \sum_{n=1}^{4} p_n z^n \quad \text{with} \quad \begin{bmatrix} p_1 \\ p_2 \\ p_3 \\ p_4 \end{bmatrix} = \begin{bmatrix} 1 & z_{RT} & z_{RT}^2 & z_{RT}^3 \\ 0 & 1 & 2z_{RT} & 3z_{RT}^2 \\ 1 & z_V & z_V^2 & z_V^3 \\ 0 & 1 & 2z_V & 3z_V^2 \end{bmatrix}^{-1} \begin{bmatrix} \alpha_{RT} \\ 0 \\ \alpha_V \\ 0 \end{bmatrix} \tag{8.1}$$

Figure 8.4: Axisymmetrix mesh of the LBH

Table 8.2: Input parameter numbering

	Axial	
Radial	Ramp Top	V-point
Outer	α_1	α_3
Inner	α_2	α_4

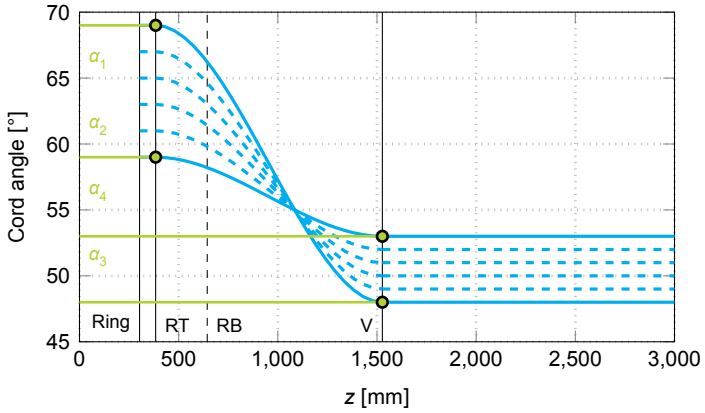

Figure 8.3: Example of radial and axial angle variation

8.4. Finite element analysis

The LBH has a quasi-axisymmetric geometry, where the smeared properties of the rebar elements allow the cord reinforcement layers to be modelled axisymmetrically (as was the case in Sections 5.3.2 and 6.4.2). The LBH FE model consists of three parts: the coupling, the rubber body, and the cord layers.

The coupling is a steel solid part that serves as a connection point for other hoses, as well as a retainer for the cords which are turned around the ring. Since it is assumed not to deform significantly upon pressurisation of the hose, it is modelled as a 2D analytical rigid shell whose motions are coupled to an axial reference point at the axial centre (symmetry midplane). The rubber mesh geometry was obtained from the profiles generated by TANIQWind, where the inner diameter and outer rubber layer define the rubber part. Even though the rubber is applied in separate layers (e.g. in between the cord layers), compression and vulcanisation of the LBH is assumed to result in perfect cohesion between these layers. Since the rubber material is specified as being incompressible, internal pressure on the rubber elements inside the coupling caused convergence difficulties. To increase the numerical stability of the model this rubber liner inside the coupling is included in the geometry of the solid part as shown in Figure 8.4, while perfect adhesion is assumed on the coupling-rubber interface (using a master-slave tie constraint). As was the case in Sections 5.3.2 and 6.4.2, the rebar mesh consists of `CGAX4H` elements. The mesh is partitioned with respect to the geometry of the rubber part, ensuring severely deformed elements are generated (e.g. large aspect ratio). The mesh is furthermore partitioned in several axial sections, allowing monitoring of the maximum strain values occurring in each of these sections:

- ε_1: Coupling - ramp top: $z \in (2616, 3000)$ mm
- ε_2: Ramp top - ramp base: $z \in (2356, 2616)$ mm
- ε_3: Ramp base - V-point: $z \in (1473, 2356)$ mm
- ε_4: V-point - hose centre: $z \in (0, 1473)$ mm

The mesh of the cord layers exists of `SFMGAX1` elements that follow the profiles as generated by TANIQWind, which is based on the manufacturing process parameters (e.g. thickness of the rubber tape). Each element in the mesh is assigned its unique set and rebar parameters. The number of cords in each reinforcement layer is dependent on the angle in the hose body, where a coverage c of 120 % is enforced at the axial centre. This is in contrast to the MLC, where TANIQWind was used so select a suitable winding pattern that achieves near 120 % coverage (thus allowing it to differ slightly). Furthermore this FE model ignores the cord build-up behind the ring as a result of the pattern (where the cords need to travel behind the ring to the next loop).

The angle distribution between the coupling and ramp top is generated using TANIQWind, where the cord angle is specified as 90° at the coupling profile. Subsequently, as mentioned before, the cord angle between the ramp top (α_{RT}) and the V-point (α_V) is obtained using Equation (8.1). Finally the cord angle is kept constant in the cylindrical section of the hose body (α_V) past the V-point. The number of cords n_C is obtained through Equation (2.11) (with r_V the radius of the cord layer at the V-point and D_C the cord diameter):

$$n_C = 2\pi c \frac{r_V \cos \alpha_V}{D_C} \tag{8.2}$$

Subsequently the rebar spacing s at a given z-coordinate is given by:

$$s(z) = \frac{2\pi r(z)}{n_C} \cos \alpha(z) = \frac{D_C}{c} \frac{r(z)}{r_V} \frac{\cos \alpha(z)}{\cos \alpha_V} \tag{8.3}$$

Since the coupling reference point defines the motion of the rigid shell, it can only displace and rotate along the z-axis. Half symmetry conditions are applied on the rubber nodes at $z = 0$, halving the FE model size. The cord elements have their degrees of freedom coupled to their host rubber elements, were mesh sectioning ensures cord surface nodes to always be in line with two nodes of its rubber host element.

A mesh convergence analysis was performed by loading the LBH with an internal pressure of 70 bar (7 MPa) and resulting axial force of 9062 kN, to simulate the pressure acting on the end caps. The initial element size was set to 10 mm and decreased with $\sqrt{2}/2$ in every step, such that the (2D) mesh density doubles with each step. The convergence criterion was <0.1 % improvement which, as can be seen in Table 8.3, is achieved with a mesh of element size 7.07 mm.

Table 8.3: Mesh sensitivity analysis of LBH rebar mesh

S_{max} cords		Element size [mm]		
		10	7.07	5
Hose body	[MPa]	576.79	576.83	576.85
	[%]	0.01	0.00	0.03
Ramp	[MPa]	433.55	434.62	434.92
	[%]	0.25	0.07	0.08

Whereas the LBH was inflated to 70 bar for the mesh convergence analysis, the inflation pressure is increased in the Finite Element Analyses (FEAs) for the generation of the data set required for the surrogate model. The LBH is inflated with an internal pressure of 120 bar (12 MPa) combined with a corresponding axial load of 15 535 kN, to ensure maximum cord strain is achieved. The step is limited to 5 % of the load (0.6 MPa) while at each step the maximum strain value is monitored through a FORTRAN user subroutine. Once this value is reached the analysis is terminated and the burst pressure is calculated through linear interpolation with the recordings of the previous step. The maximum strain values are recorded in the four sections of the LBH listed in Section 8.4. This allows the failure ratio ρ defined as the ratio of the peak strain occurring near to coupling over the peak strain in the hose body. This failure ratio is to be used as a design constraint in the cord angle optimisation, since for the safety of operators the failure should occur in the hose body.

9

Reinforcement Angle Optimisation of Multilayered Cord-rubber Hoses

The parametrised Finite Element (FE) rebar model developed in Chapter 8 is used to generate a four-dimensional data set containing 2000 points to be used as a Design and Analysis of Computer Experiments (DACE) surrogate model, following the approach used in Chapter 7. Additionally a 50 point data set is used to assess the accuracy of this DACE model. Whereas one surrogate model was used in Chapter 7 to emulate the global maximum strain in each Multilayered Cylinder (MLC) design, in total six DACE models will be created. These will be covered in Section 9.1. Subsequently these models will be used in a genetic optimisation algorithm. The process parameters, fitness evaluation, and optimisation results are discussed in Section 9.2.

9.1. Surrogate models

During the Finite Element Analyses (FEAs) of the axisymmetric rebar Large Bore Hose (LBH) models the global maximum strain is monitored. At each analysis increment, with a maximum of 5 % of the total load (12 MPa) the maximum strains in four sections of the LBH are recorded. When the cord failure strain is surpassed, the burst pressure and corresponding strains in the sections are calculated. Additionally, for each design point the total cord usage is calculated. Two data sets were generated: a 2000 points data set distributed using Latin hypercube sampling to ensure good coverage of the entire design space used to fit the DACE models, and a randomly selected data set of 50 points as control data to assess the accuracy of the DACE models. The random points are generated using MATLAB's `rand` function, which provides uniformly distributed random numbers.

9.1.1. Maximum strain values

The LBH is divided into four sections axially, which are of particular interest to assess the failure ratio when the maximum cord strain is reached. The following sections are being monitored:

- ε_1: Coupling - ramp top: $z \in (2616, 3000)$ mm
- ε_2: Ramp top - ramp base: $z \in (2356, 2616)$ mm
- ε_3: Ramp base - V-point: $z \in (1473, 2356)$ mm
- ε_4: V-point - hose centre: $z \in (0, 1473)$ mm

The failure ratio ρ is defined as:

$$\rho = \frac{\max(\varepsilon_1, \varepsilon_2)}{\max(\varepsilon_3, \varepsilon_4)} \tag{9.1}$$

The failure ratios of the 2000 points DACE data set are shown in Figure 9.1 at the axial coordinates where the maximum cord strain was reached. The best (lowest) failure ratios are observed in the hose body ($z \in (0, 1473)$ mm), while the largest ratios are observed on top of the ring ($z = 2697$ mm). The maximum acceptable failure ratio $\rho = 0.85$ is indicated with a horizontal dashed line, where all design points below this line meet the safety requirement.

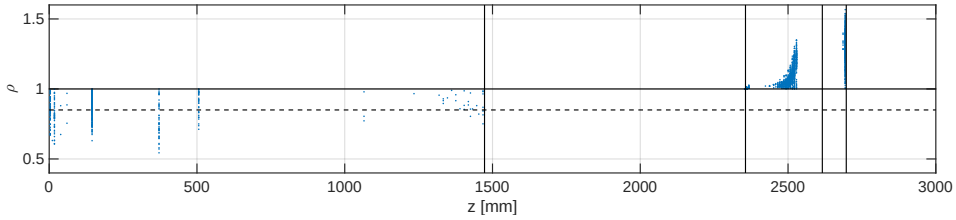

Figure 9.1: Failure ratios at location of first cord failure for DACE model points

A four-dimensional model is fitted to each of these strain measurements. The relative error of predicted strain values at the 50 independent control points with the actual FEA values is the highest for ε_4, with a 12.8 % maximum error as indicated in Table 9.1. The mean errors for the other strain values as well as the failure ratio are less than 1 %, indicating a good fit of the DACE models.

Table 9.1: Error between prediction of the 2000 point DACE models and 50 point test set

Error [%]	ε_1	ε_2	ε_3	ε_4	ρ
Max	1.47	1.58	4.80	12.80	4.18
Mean	0.26	0.33	0.61	1.51	0.56
Std Dev	0.29	0.39	0.88	2.44	0.73

9.1.2. Burst pressure

The burst pressure, i.e. the pressure at which maximum cord strain is reached, is a metric that indicates the relative strength of the design point. Lower burst pressure are observed to be paired primarily with first cord failure occurring between the ramp base and coupling in Figure 9.2 ($z > 2356$ mm). It indicates that ensuring the failure to occur in the hose section will result in a higher overall burst pressure, whereas weaker designs tend to fail in the unsafe region.

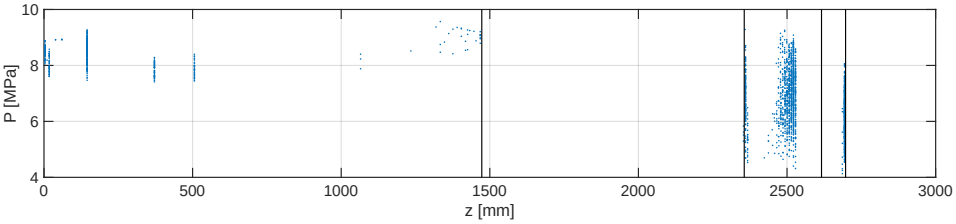

Figure 9.2: Burst pressure at location of first cord failure for DACE model points

The relative errors between the predicted and the FEA reported burst pressures for the 50 control points have a mean of 0.31 %, with a standard deviation of 0.35 % and a maximum of 1.56 %.

9.1.3. Cord usage

The cord usage is obtained by calculating the length of the cord path in each layer multiplied by the number of cords. The latter is based on the desired coverage in the hose body (120 %), as is defined by Equation (8.2). The cord length between the coupling and ring is obtained using TANIQWind software, whereas in the other sections the cord length is dependent on the cord angle $\alpha(z)$ (with β the slope of the ramp):

$$\Delta l = \begin{cases} \frac{\Delta z}{\cos\alpha} & z \in [2616, 2697] \\ \frac{1}{\cos\beta} \int \frac{1}{\cos\alpha(z)} \, \mathrm{d}z & z \in [2356, 2616] \\ \int \frac{1}{\cos\alpha(z)} \, \mathrm{d}z & z \in [1473, 2356] \\ \frac{\Delta z}{\cos\alpha} & z \in [0, 1473] \end{cases} \tag{9.2}$$

Designs with low cord usage are observed to fail predominantly in the coupling region, as can be seen in Figure 9.3. These points are desirable in the minimal cord usage optimisation, however failure in this region is deemed unsafe ($\rho > 0.85$ in Figure 9.1).

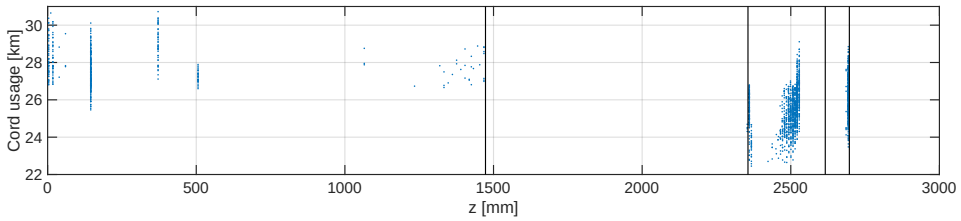

Figure 9.3: Cord usage at location of first cord failure for DACE model points

The DACE model predicting the cord usage has mean relative error of 0.03 % with a maximum of 0.08 %. The high accuracy of the model fit is contributed to quasi-linear relations existing between the coverage, resulting number of cords, and path length based on the specified angles.

9.2. Genetic algorithm optimisation

In Section 7.2 two sets of Genetic Algorithm (GA) optimisations were performed: with real-valued parameters ($\alpha_i \in [46, 69] \in \mathbb{R}$) and integer-limited cord angles ($\alpha_i \in [46, 69] \in \mathbb{N}$). The latter had a higher success ratio in identifying the most optimal point because of the reduced number of possible design points compared to the former case. However, since the accuracy of the manufacturing process is about 1°, the integer-limited approach is a desirable and computationally efficient choice. To test the consistency of the optimal configuration returned by the GA, 500 optimisation runs were performed. The standard GA options as defined by MATLAB were used.

9.2.1. Design fitness function

The aim of the optimisation framework is to reduce cord usage in the LBH product. A lower cord usage reduces the manufacturing time, which allows a higher production rate. Furthermore the decreased material consumption benefits the sustainability of the product, where less material is discarded (or has to be recycled) at the end-of-life. In the global parameter analysis on the DACE data set, however, can be seen that lower cord usage is generally related to undesirable failure ratios. In order to ensure first cord failure to occur in the hose body, and thus the safety of the LBH design, the failure ratio ρ is set as a maximum value constraint of the design fitness. When $\rho > 0.85$ a penalty factor of 1000 is assigned to the design, increasing the likelihood of it being discarded by the GA.

9.2.2. Integer-limited input parameters

The integer-limited GA managed to successfully converge on a feasible design in 492 out of 500 runs (98.4 %). The distributions of the input parameters are shown in Figure 9.4. Interestingly α_3 lies consistently on the boundary of the allowed parameter range, which represents the cord angle on the outer layer at the centre of the LBH. If a constant coverage is assumed on a cylindrical profile with constant cord angle, the cord usage is independent of this angle (and thus also number of cords). This means that the cord usage is independent of the cord angle in the central hose body. Cord usage reductions are therefore obtainable in the ramp and coupling region, where designs with a larger angle in the central hose body resulted in lower cord usage.

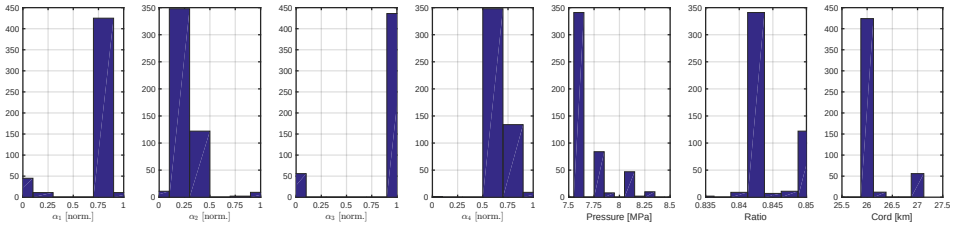

Figure 9.4: Optimal configurations identified by integer-limited GA (492/500)

9.2.3. Optimal cord angle combination

The strain distribution of the optimal design point identified by both the real-valued and integer-limited is shown in Figure 9.5. Failure strain is reached in the hose body, with a failure ratio ρ = 0.845. The optimal cord angles are shown in Table 9.2. The inner cord layer can be observed to reach the failure strain, whereas the outer layer is loaded only 45.8 % of this value. The strain distributions through the thickness show quasi-equal loading on the ramp. This, in combination with a highly unequal strain distribution in the hose centre, results in a favourable failure ratio.

Table 9.2: Optimal cord angle configuration for the LBH ($\alpha_i \in \mathbb{N}$) [deg]

	Axial	
Radial	Edge	Centre
Outer	■	■
Inner	■	■

Since a large cord angle on the outer layer in the hose centre results in a lower number of cords (given a constant coverage), and these layers have the largest diameter, the weight reduction is achieved in the outermost layers. The model has a cord usage of 25.990 km, which is a weight saving of 14.9 % compared to the reference design.

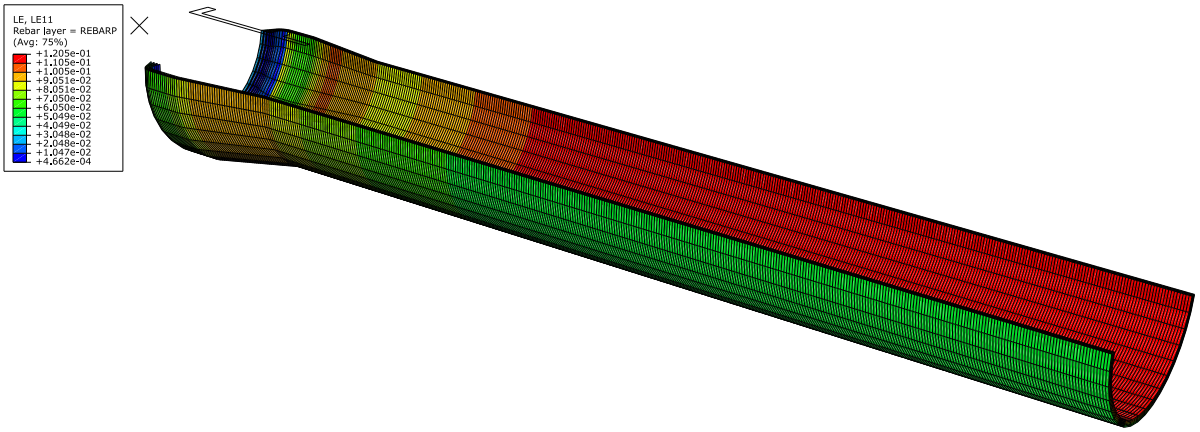

Figure 9.5: Strain distribution in the LBH design with minimal cord usage satisfying the failure ratio requirement

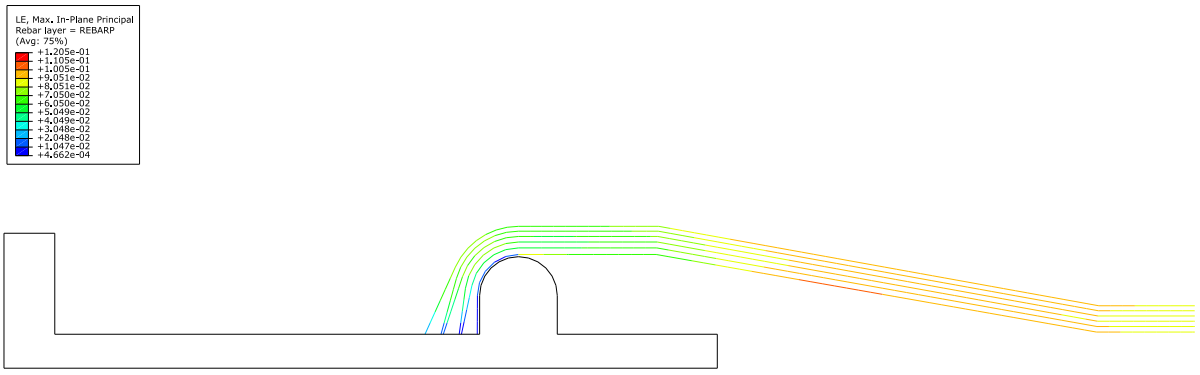

(a) Coupling

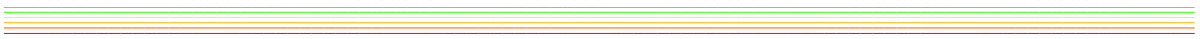

(b) Hose centre

Figure 9.6: Close-up of the strain distribution

10

Conclusions and Recommendations

Conclusion

This research was performed in cooperation with TANIQ, where the objective was to create an optimisation framework to minimise cord usage in Large Bore Hose (LBH) products by developing an optimization framework and axisymmetric parametrised Finite Element (FE) model. The reduction in cord usage was measured with respect to in-use reference design, which was the result of a design iteration. This reference LBH requires 30.5 km of reinforcing cord, applied in six layers.

With the aim of reducing computational resources required for performing Finite Element Analyses (FEAs) in the design optimisation, an axisymmetric FE model of the LBH was developed. This approach used ABAQUS's rebar method to smear the directional properties of the reinforcing cord layers over surface elements. In the single and multi layer cylinder work packages this method showed a time reduction of 40 % and 70 %, respectively, compared to the baseline three-dimensional truss method.

Unit tests performed on rubber cubes with cord reinforcements along the midplane showed good agreement in reaction force required to perform an axial stretch between the rebar and truss methods. The truss method, however, indicated diverging results when the mesh size decreased as the trusses add directional stiffness to a small number of rubber elements, whereas the rebar maintains smeared properties over all elements. The unit tests were performed using both hyperelastic and elastic-plastic material models for the cord reinforcements, which showed good agreement, however at small strain values.

Recreation of a McKibben artificial muscle actuator, a rubber bladder with an external cord braid, showed consistent behaviour between the rebar and truss methods using an elastic-plastic material model for the cords and the truss method using a hyperelastic material model. The rebar method with hyperelastic material model showed significant divergence with the former during stretching of the actuator, where the cord angle change was more pronounced at a cost of lower reported strain values. However, since the divergence was small during inflation of the actuator and the rebar method indicated a time reduction of 40 % over the truss method, this dissimilarity was accepted for the subsequent parametric studies.

The parametric studies performed on a three-layer cord-rubber pressure vessel visualised the effects of radial and axial cord angle variation on the peak strains occurring upon phase II inflation, where deformation is dominated by straining of the cords following cord rotation in phase I. The neutral angle, at which cords are aligned with the major principal stress, plays an important role on both phase I and phase II deformation behaviour. At small initial cord angles (smaller than the neutral angle) the truss and rebar methods showed good agreement in deformation behaviour and reported peak strains. Designs with initial cord-angles larger than the neutral angle (i.e. resulting in axial expansion and radial contraction during phase I deformation) showed a difference in reported peak strain values between both models. The rebar method showed quasi-symmetrical behaviour around the neutral angle whereas the higher values indicated by the truss model were deemed a result of local stress concentrations at the clamped edge. This stress concentration is a consequence of the basic geometry of the cylindrical pressure vessel, where the peak strain occurred either at the edge or the axial centre depending on the relation of the initial cord angles to the neutral angle.

Radial angle variation (i.e. each layer having a unique uniform cord angle) confirmed that the peak strain is lowest when all three layers were loaded equally. This was shown to be achievable by varying the cord angle radially, since the hoop stress in thick-walled cylindrical pressure vessels is variable through the thickness. A larger difference in cord angle between the reinforcement layers showed to prohibit cord rotation during phase I deformation, resulting in larger peak strains. Consequently, as a design guideline to minimise the peak strain, the average cord angle should be near the neutral angle, with the angles on the inner layer being slightly smaller than the outer angle. This will result in phase I deformations being counteracted, effectively loading the outer reinforcement layer. Since this study assumed a fixed cord coverage in the layers, the number of cords is dependent on the cord angle and layer radius.

Axial angle variation indicated that the cord angle is of higher importance at the centre of the cylinder compared to at the edge, since the clamped edge decreases the effect of the latter on the structural response. Interestingly, an initial cord angle at the edge smaller than the neutral angle in combination with a larger angle at the centre lowered the peak strain occurring. In such cases a radial expansion near the clamped edge during phase I deformation prevents a local stress concentration, whereas the larger angle in the centre results in a radial contraction. This allows for the axial location of the peak strain to be manipulated through axial cord angle variation. Peak strains were observed to occur consistently on the inner cord layer, indicating that a combination of radial and axial angle variation can result in efficient load distribution throughout the cord layers while preventing local stress concentrations.

In order to decouple FEA from the optimisation algorithm, enabling multiple optimisation runs, a Design and Analysis of Computer Experiments (DACE) surrogate model was fit to a 2000 point four-dimensional data set covering both radial and axial angle variation. The DACE model showed high accuracy when compared to the previously studied two-dimensional spaces, where the mean relative errors were 1.36 % and 1.30 % with the radial and axial cord angle variation data sets, respectively. Since the error was observed to be largest at the edge of the design space (interpolation), the allowed variable range was restricted to exclude boundary values during the Genetic Algorithm (GA) optimisation.

Limiting the input parameters to integer values, in accordance with manufacturing feasibility, increased the success rate in identifying the cord angle configuration with lowest peak strain from 45 % to 86 %. Default GA settings were used in MATLAB, where the consistent termination after the minimum number of generations indicated possible reduction of the number of functions calls. The design identified by the optimisation had larger angles at the centre of the cylinder compared to at the edge, with the peak strain occurring at 10 % axial length from the edge. A FEA of the proposed design confirmed the accuracy of the DACE model in predicting the peak strain value with only 0.07 % difference.

Because the rebar method showed consistent behaviour in the parametric study, as well as robustness against local stress concentrations thanks to the smeared properties, it was used to develop a FE model of the LBH product based on a proved reference design. The model was parametrised by allowing cord angle specification on the inner and outer layers at the ramp top and central hose body. Between these points a cubic angle variation was used, to ensure a smooth stiffness transition and prevent local stress concentrations.

The coverage was defined as 120 % at the hose centre, meaning cord usage was independent of cord angle in the central hose body. Cord usage reductions were therefore obtainable in the ramp and coupling region, where designs with a larger angle in the central hose body resulted in lower cord usage. As a result, design with lower cord usage were observed to result in failure occurring near the ramp and coupling at a lower inflation pressure, which does not satisfy the safety constraint. A maximum failure ratio was set as a design constraint, ensuring failure to occur in the cylindrical hose body and higher burst pressures.

A DACE model constructed using 2000 design configurations showed a mean error of less than 1 % in peak strain values in various sections along the hose axis compared to an independent random data set of 50 design points. GA optimisations performed on this surrogate model showed a 69 % success rate in identifying the design configuration with lowest cord usage satisfying the safety constraint. A FEA of the proposed design showed at most 0.3 % difference with the DACE prediction. Interestingly the strain distribution in this design shows the outer layer serves primarily to ensure failure does not occur in the safety critical region, while the inner layer shows the highest strain in the central hose body. Compared to the reference design, the proposed design uses 14.9 % less cord material.

The stability and consistency of the rebar method throughout the work packages indicated good potential in decreasing FEA computational requirements in performing a design optimisation of quasi-axisymmetric cord-rubber structures. The usage of a DACE surrogate model allows the decoupling of FEAs from the optimisation algorithm while ensuring accurate strain predictions. The combination of these two elements result in a robust design optimisation framework, which can be expanded to take into account additional design requirements such as the burst pressure.

Recommendations

During the span of the project a LBH prototype was built, where tensile cord tests were performed to obtain accurate tensile properties. The burst test of the prototype, however, did not provide sufficient data that could support validation of the rebar FE model. If this model were to be used to perform a strength sizing (i.e. for burst pressure), a series of validation tests should be performed. Since the cord layers are embedded deep into the rubber, it is impossible to directly measure the strain in the cord layers. The following data can be collected in function of the internal pressure:

- Radial and axial deformation (using digital image correlation techniques)
- Cord failure (visually or using microphones, in case the LBH does not burst on first cord failure)
- Failure location (visual inspection)

A difference in strain distribution and magnitude between hyperelastic rebar and truss models has been observed in the various FEA work packages. This difference was deemed acceptable for the optimisation processes, since the rebar showed smooth and symmetric trends around the neutral angle. The difference was most pronounced during stretching of the McKibben actuator. Even though this loading is unrepresentative for LBH inflation, the cause of this difference has not been determined. Both rebar and truss elements can only undergo axial deformation according to their definition by ABAQUS. Extended discussions with ABAQUS customer service did not result in conclusions regarding the origin of this disagreement. Validation of the FE model could provide more clarity into the accuracy of either methods.

This difference does not occur when an elastic-plastic material model is used instead. When the strain in a uniaxial element is strictly increasing, however, no difference should be oberservable between hyperelastic and elastic-plastic models. The elastic-plastic material model is not representative for the hyperelastic behaviour of Polyethylene Terephthalate (PET) cords, and should therefore not be used in FEA of LBH designs. Nevertheless, it could prove useful in understanding the difference observed between hyperelastic rebar and truss models.

The optimisation processes in this thesis assumed a specified coverage (at the axial centre). This approach was chosen to ensure sufficient coverage of the rubber layers while allowing proper impregnation of the cord layers. An alternative research could be performed where the number of cords is defined, allowing the coverage to vary. This could provide additional insight on the effect of the cord angles on peak strains and deformation behaviour, similarly to the Multilayered Cylinder (MLC) sensitivity study. Also the LBH optimisation could be revisited, where specifying a cord number could yield different results.

Alternative or additional design constraints could be implemented into the optimisation framework, such as e.g. an upper limit on axial expansion or friction requirement. The latter was not considered since every design was assumed feasible to manufacture. In reality sufficient friction is required to allow cord angle transitions, which could pose a constraint on the manufacturing feasibility. With a validated FE model the burst pressure can be imposed as a minimum constraint, to ensure the design meets working pressure requirements.

In this thesis four cord angles were identified as parameters to the optimisation algorithm. A cubic angle trend was assumed in axial direction along the LBH, however, many alternative relations between these parameters (e.g. linear, quadratic) could potentially be explored. The optimisation framework furthermore allows for addition of other parameters. It is important to note that additional dimensions will increase the complexity of the design space. The number of design points required to ensure similar coverage in all dimensions increases exponentially, and consequently the total computational cost. The following parameters come to mind:

- Cord angles at the ramp base
- Cord angles at the hose centre
- Cord usage (possibly variable radially)
- Cord number (possibly variable radially)
- Number of cord layers

Finally, standard GA options were used in MATLAB. While the GA had a 86 % success rate in identifying the most optimal MLC, the success rate in the LBH optimisation was only 53 %. The success rate can possible be improved by tweaking the population size, mutation rate, and convergence criterion.

Bibliography

[1] E.O. Bolarinwa and O.A. Olatunbosun. Finite element simulation of the tyre burst test. *Proceedings of the Institution of Mechanical Engineers, Part D: Journal of Automobile Engineering*, 218(11): 1251–1258, 2004. doi:10.1243/0954407042580075.

[2] M. Behroozi, O.A. Olatunbosun, and W. Ding. Finite element analysis of aircraft tyre – effect of model complexity on tyre performance characteristics. *Materials & Design*, 35:810–819, 2012. ISSN 0261-3069. doi:10.1016/j.matdes.2011.05.055. New Rubber Materials, Test Methods and Processes.

[3] A.K. Kondé, I. Rosu, F. Lebon, O. Brardo, and B. Devésa. On the modeling of aircraft tire. *Aerospace Science and Technology*, 27(1):67–75, Jun 2013. ISSN 1270-9638. doi:10.1016/j.ast.2012.06.008.

[4] M.L.P. Tonatto, M.M.d.C. Forte, S.C. Amico, P.B. Roese, and R.T. Araujo. Numeric analysis of the burst pressure pipe based on rubber and polymeric cords. *Polímeros*, 25:109–116, Feb 2015. ISSN 0104-1428. doi:10.1590/0104-1428.1678.

[5] M.L.P. Tonatto, V. Tita, R.T. Araujo, M.M.d.C. Forte, and S.C. Amico. Parametric analysis of an offloading hose under internal pressure via computational modeling. *Marine Structures*, 51:174–187, 2017. ISSN 0951-8339. doi:10.1016/j.marstruc.2016.10.008.

[6] M.L.P. Tonatto, V. Tita, M.M.d.C. Forte, and S.C. Amico. Multi-scale analyses of a floating marine hose with hybrid polyaramid/polyamide reinforcement cords. *Marine Structures*, 60:279–292, 2018. ISSN 0951-8339. doi:10.1016/j.marstruc.2018.04.005.

[7] Q. Gao, P. Zhang, M. Duan, X. Yang, W. Shi, C. An, and Z. Li. Investigation on structural behavior of ring-stiffened composite offshore rubber hose under internal pressure. *Applied Ocean Research*, 79:7–19, 2018. ISSN 0141-1187. doi:10.1016/j.apor.2018.07.007.

[8] F.S. Almeida and A.M. Awruch. Design optimization of composite laminated structures using genetic algorithms and finite element analysis. *Composite Structures*, 88(3):443–454, 2009. ISSN 0263-8223. doi:10.1016/j.compstruct.2008.05.004.

[9] V.K. Maes, L. Pavlov, and S.M. Simonian. An efficient semi-automated optimisation approach for (grid-stiffened) composite structures: Application to ariane 6 interstage. *Composite Structures*, 209:1042–1049, Feb 2019. ISSN 0263-8223. doi:10.1016/j.compstruct.2016.02.082.

[10] C. Bisagni and L. Lanzi. Post-buckling optimisation of composite stiffened panels using neural networks. *Composite Structures*, 58(2):237–247, 2002. ISSN 0263-8223. doi:10.1016/S0263-8223(02)00053-3.

[11] L. Lanzi, C. Bisagni, and S. Ricci. Neural network systems to reproduce crash behavior of structural components. *Computers & Structures*, 82(1):93–108, 2004. ISSN 0045-7949. doi:10.1016/j.compstruc.2003.06.001.

[12] X. Yang, M. Behroozi, and O.A. Olatunbosun. A neural network approach to predicting car tyre micro-scale and macro-scale behaviour. *Journal of Intelligent Learning Systems and Applications*, 6:11–20, 2014. doi:10.4236/jilsa.2014.61002.

[13] S.N. Lophaven, H.B. Nielsen, and J. Søndergaard. DACE - a matlab kriging toolbox, version 2.0. Technical report, Informatics and Mathematical Modelling, Technical University of Denmark, DTU, 2002.

[14] K. Kalnins, G. Jekabsons, and R. Rikards. Metamodels for optimisation of post-buckling responses in full-scale composite structures. In *Proceedings of 8th World Congress on Structural and multidisciplinary optimisation, Lisbon, Portugal*, 2009.

[15] K. Wang, C. Zhang, J. Su, B. Wang, and Y. Hung. Optimisation of composite manufacturing processes with computer experiments and kriging methods. *International Journal of Computer Integrated Manufacturing*, 26(3):216–226, 2013. doi:10.1080/0951192X.2012.684723.

[16] M.A. Luersen, C.A. Steeves, and P.B. Nair. Optimisation of a laminated composite cylindrical shell with curvilinear fibre paths using a surrogate-based approach. volume 9 of *ASME International Mechanical Engineering Congress and Exposition*, 2014. doi:10.1115/IMECE2014-36285.

[17] G. K. Klute and B. Hannaford. Accounting for elastic energy storage in mckibben artificial muscle actuators. *Journal of Dynamic Systems, Measurement, and Control*, 122(2):386–388, 12 1998. ISSN 0022-0434. doi:10.1115/1.482478.

[18] R.H.W. ten Thije, R. Akkerman, and J. Huétink. Large deformation simulation of anisotropic material using an updated lagrangian finite element method. *Computer Methods in Applied Mechanics and Engineering*, 196(33):3141–3150, 2007. ISSN 0045-7825. doi:10.1016/j.cma.2007.02.010.

[19] S. van der Linden. Design optimisation of a thick filament wound reinforced rubber hose coupling section. Master's thesis, Delft University of Technology, Sep 2017.

[20] R.J. Young and P.A. Lovell. *Introduction to Polymers*. CRC Press, third edition, 2011. ISBN 978-1-4398-9415-6.

[21] R.J. Cembrola and T.J. Dudek. Cord/rubber material properties. *Rubber Chemistry and Technology*, 58(4):830–856, 1985. doi:10.5254/1.3536096.

[22] A. Ali, M Hosseini, and B B Sahari. A review and comparison on some rubber elasticity models. *Journal of Scientific and Industrial Research*, 69(7):495–500, Jul 2010.

[23] R.W. Ogden. Large deformation isotropic elasticity–on the correlation of theory and experiment for incompressible rubberlike solids. *Proceedings of the Royal Society of London. A. Mathematical and Physical Sciences*, 326(1567):565–584, Feb 1972. doi:10.1098/rspa.1972.0026.

[24] R.S. Rivlin. Large elastic deformations of isotropic materials iv. further developments of the general theory. *Philosophical Transactions of the Royal Society of London. Series A, Mathematical and Physical Sciences*, 241(835):379–397, Oct 1948. doi:10.1098/rsta.1948.0024.

[25] M. Mooney. A theory of large elastic deformation. *Journal of applied physics*, 11(9):582–592, Sep 1940.

[26] O.H. Yeoh. Some forms of the strain energy function for rubber. *Rubber Chemistry and Technology*, 66(5):754–771, Nov 1993. doi:10.5254/1.3538343.

[27] E. Tönük and Y.S. Ünlüsoy. Prediction of automobile tire cornering force characteristics by finite element modeling and analysis. *Computers & Structures*, 79(13):1219–1232, May 2001. ISSN 0045-7949. doi:10.1016/S0045-7949(01)00022-0.

[28] J. Phromjan and C. Suvanjumrat. A suitable constitutive model for solid tire analysis under quasi-static loads using finite element method. *Engineering Journal*, 22(2):141–155, Mar 2018. doi:10.4186/ej.2018.22.2.141.

[29] G. Marckmann and E. Verron. Comparison of hyperelastic models for rubber-like materials. *Rubber chemistry and technology*, 79(5):835–858, Nov 2006. doi:10.5254/1.3547969.

[30] S. Koussios. *Filament Winding. A Unified Approach*. PhD thesis, Delft University of Technology, 2004.

[31] *Resorcinol: Chemistry, Technology and Applications*. Springer Berlin Heidelberg, 2005. ISBN 978-3-540-25142-2. doi:10.1007/3-540-28090-1.

[32] F. C. Shen. A filament-wound structure technology overview. *Materials Chemistry and Physics*, 42(2):96–100, 1995. ISSN 0254-0584. doi:10.1016/0254-0584(95)01554-X.

[33] S. Grove. Optimum fiber orientation in filament wound structures. *Journal of Materials Science Letters*, 18(15):1203–1203, Aug 1999. ISSN 1573-4811. doi:10.1023/A:1006694000701.

[34] P.C. Bregman, M. Kuipers, H.L.J. Teerling, and W.A. van der Veen. Strength and stiffness of a flexible high-pressure spiral hose. *Acta Mechanica*, 97(3):185–204, Sep 1993. doi:10.1007/BF01176525.

[35] P. Mertiny, F. Ellyin, and A. Hothan. Stacking sequence effect of multi–angle filament wound tubular composite structures. *Journal of Composite Materials*, 38(13):1095–1113, Jul 2004. doi:10.1177/0021998304042077.

[36] Anil K Bhowmick. *Rubber products manufacturing technology*. CRC Press, 1994.

[37] S.F.M. de Almeida and Z.S.N. Neto. Effect of void content on the strength of composite laminates. *Composite Structures*, 28(2):139–148, 1994. ISSN 0263-8223. doi:10.1016/0263-8223(94)90044-2.

[38] W.J. Cantwell and J. Morton. The significance of damage and defects and their detection in composite materials: A review. *The Journal of Strain Analysis for Engineering Design*, 27(1):29–42, 1992. doi:10.1243/03093247V271029.

[39] A.K.R Noor and J.A. Tanner. Advances and trends in the development of computational models for tires. In A.K. Noor and R.J. Hayduk, editors, *Advances and Trends in Structures and Dynamics*, pages 517–533. Pergamon, 1985. ISBN 978-0-08-032789-1. doi:10.1016/B978-0-08-032789-1.50057-4.

[40] F. Tabaddor. Mechanical properties of cord-rubber composites. *Composite Structures*, 3(1):33–53, 1985. ISSN 0263-8223. doi:10.1016/0263-8223(85)90027-3.

[41] Dassault Systèmes. *SIMULIA User Assistance 2018*, 2018.

[42] B. Davids. Structural analysis of multi-layered filament wound cord-reinforced rubber products. Master's thesis, Delft University of Technology, Jul 2014.

[43] S. Reese. Meso-macro modelling of fibre-reinforced rubber-like composites exhibiting large elastoplastic deformation. *International Journal of Solids and Structures*, 40(4):951–980, 2003. ISSN 0020-7683. doi:10.1016/S0020-7683(02)00602-9.

[44] S.B. Sharma and M.P.F. Sutcliffe. A simplified finite element model for draping of woven material. *Composites Part A: Applied Science and Manufacturing*, 35(6):637–643, 2004. ISSN 1359-835X. doi:10.1016/j.compositesa.2004.02.013.

[45] P. Helnwein, C.H. Liu, G. Meschke, and H.A. Mang. A new 3-d finite element model for cord-reinforced rubber composites—application to analysis of automobile tires. *Finite Elements in Analysis and Design*, 14(1):1–16, 1993. ISSN 0168-874X. doi:10.1016/0168-874X(93)90075-2.

[46] P. Mertiny, F. Ellyin, and A. Hothan. An experimental investigation on the effect of multi-angle filament winding on the strength of tubular composite structures. *Composites Science and Technology*, 64(1):1–9, 2004. ISSN 0266–3538. doi:10.1016/S0266-3538(03)00198-2.

[47] J. Xing, P. Geng, and T. Yang. Stress and deformation of multiple winding angle hybrid filament-wound thick cylinder under axial loading and internal and external pressure. *Composite Structures*, 131:868–877, 2015. ISSN 0263-8223. doi:10.1016/j.compstruct.2015.05.036.

[48] M.R. Gurvich. On effective modeling of laminated cord-rubber composites. *Rubber Chemistry and Technology*, 80(4):608–620, 2007. doi:10.5254/1.3548183.

[49] A. Pirrera, M. Capuzzi, N. Buckney, and P. Weaver. Optimization of wind turbine blade spars. In *53rd AIAA/ASME/ASCE/AHS/ASC Structures, Structural Dynamics and Materials Conference*, Apr 2012. doi:10.2514/6.2012-1500.

[50] X. Fu, S. Ricci, and C. Bisagni. Multi-scale analysis and optimisation of three-dimensional woven composite structures combining response surface method and genetic algorithms. *CEAS Aeronautical Journal*, 8(1):129–141, Mar 2017. ISSN 1869-5590. doi:10.1007/s13272-016-0227-y.

[51] D. Wang, D. Tan, and L. Liu. Particle swarm optimization algorithm: an overview. *Soft Computing*, 22(2):387–408, Jan 2018. ISSN 1433-7479. doi:10.1007/s00500-016-2474-6.

[52] R. M. Jones. *Deformation theory of plasticity*. Bull Ridge Corporation, 2009.

[53] X. Yu, B. Cartwright, D. McGuckin, L. Ye, and Y.-W. Mai. Intra-ply shear locking in finite element analyses of woven fabric forming processes. *Composites Part A: Applied Science and Manufacturing*, 37(5):790–803, 2006. ISSN 1359-835X. doi:10.1016/j.compositesa.2005.04.024.

[54] R.H.W. ten Thije and R. Akkerman. Solutions to intra-ply shear locking in finite element analyses of fibre reinforced materials. *Composites Part A: Applied Science and Manufacturing*, 39(7):1167–1176, 2008. ISSN 1359-835X. doi:10.1016/j.compositesa.2008.03.014.

[55] B. Tondu. Modelling of the mckibben artificial muscle: A review. *Journal of Intelligent Material Systems and Structures*, 23(3):225–253, 2012. doi:10.1177/1045389X11435435.

[56] P.A. Gustafson and A.M. Waas. The influence of adhesive constitutive parameters in cohesive zone finite element models of adhesively bonded joints. *International Journal of Solids and Structures*, 46(10):2201–2215, 2009. ISSN 0020-7683. doi:10.1016/j.ijsolstr.2008.11.016.

[57] M.D. McKay, R.J. Beckman, and W. J. Conover. A comparison of three methods for selecting values of input variables in the analysis of output from a computer code. *Technometrics*, 21(2): 239–245, 1979. ISSN 00401706.

[58] ASTM D885/D885M-10A. Standard test methods for tire cords, tire cord fabrics, and industrial filament yarns made from manufactured organic-base fibers. Technical report, ASTM International, 2014.

A

Cord Tensile Testing

In order to obtain accurate tensile properties of the polyester cord material that will be used to manufacture a Large Bore Hose (LBH) prototype, a series of tensile tests were performed at the *Delft Aerospace Structures and Material Laboratory*. The first test, discussed in Appendix A.1, investigates the effect of the strain rate on the tensile properties. A second test, Appendix A.2, performed more accurate measurements using an extensometer at a strain rate of LBH burst testing.

A.1. Effect of crosshead travel rate on tensile modulus

The strain rate is known to affect the tensile properties of hyperelastic materials such as polyester. An increased strain rate generally results in a higher modulus, higher tensile strength, and smaller elongation at break [20]. The ASTM D885 test standard [58] describes a travel rate of 100 % to 120 % of the nominal gauge length (initial crosshead separation) per minute, which means the strain at failure is reached in 9 s for fibres with a maximum strain of 15 %. This is significantly faster than what is observed in cord-rubber hoses under working conditions (and burst testing), where pressurisation of the hose takes around 10 min.

A.1.1. Test objectives

The aim of this test is to analyse the effect of the strain (travel) rate on the tensile properties of the fibres that will be used in the hose prototype.

A.1.2. Test setup

Spiral end fixtures were used to mount the cords in the test bench, shown in Figure A.1. The cords are clamped and subsequently wound around a spiral guide with a 40 mm diameter, which prevents local stress concentrations at the clamps through a gradual load introduction. The centres of the spiral end fixtures have a vertical separation of 250 mm.

Loading of the specimen is a constant-rate-of-specimen extension. ASTM D885 [58] specifies a crosshead travel rate of 120 % nominal gage length per minute, i.e. 300 mm min^{-1} with an initial crosshead separation of 250 mm. Two sets of tensile tests are performed with the following travel rates:

- **300 mm min^{-1}:** A fast travel rate, based on ASTM D885 (120 % nominal gauge length per minute) [58].
- **10 mm min^{-1}:** A slow travel rate such that the time to failure per specimen is 10 min (4 % nominal gauge length per minute).

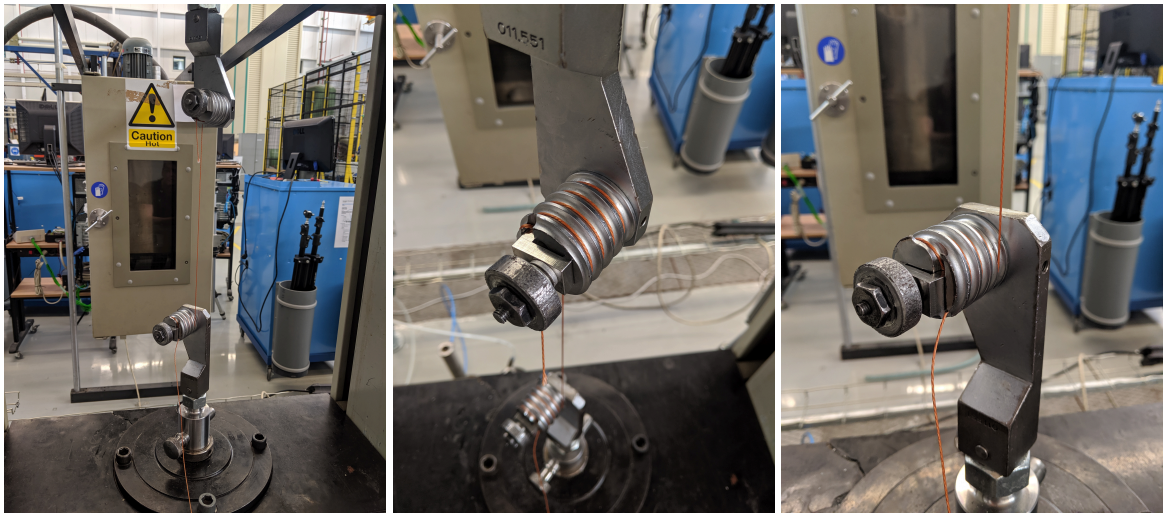

(a) Overview (b) upper spiral end fixture (c) Lower spiral end fixture

Figure A.1: Test setup using spiral end fixtures

A.1.3. Observations

Failure of the specimen was observed to occur consistently near either of the spiral guides. This could be as a result of the cords experiencing friction on the end fixtures. This shear force is proportional to the normal stress, which originates from the cord being wound around the spiral guides. ASTM D885 [58] states that specimen that break near the clamps should be discarded. However since this phenomenon is consistent and no other clamps are available at the lab, the data is retained.

Due to temporary unavailability no extensometer is used during this test. As a result only the relative crosshead travel provided information on the extension of the fibres. Since the fibres are wound around the spiral end fixtures (for a total of seven times, Figure A.1), a significant part of the specimen (78 %) experiences friction forces due to contact. As this friction reduces the (local) extension of the specimen, the (global) strain value cannot be obtained.

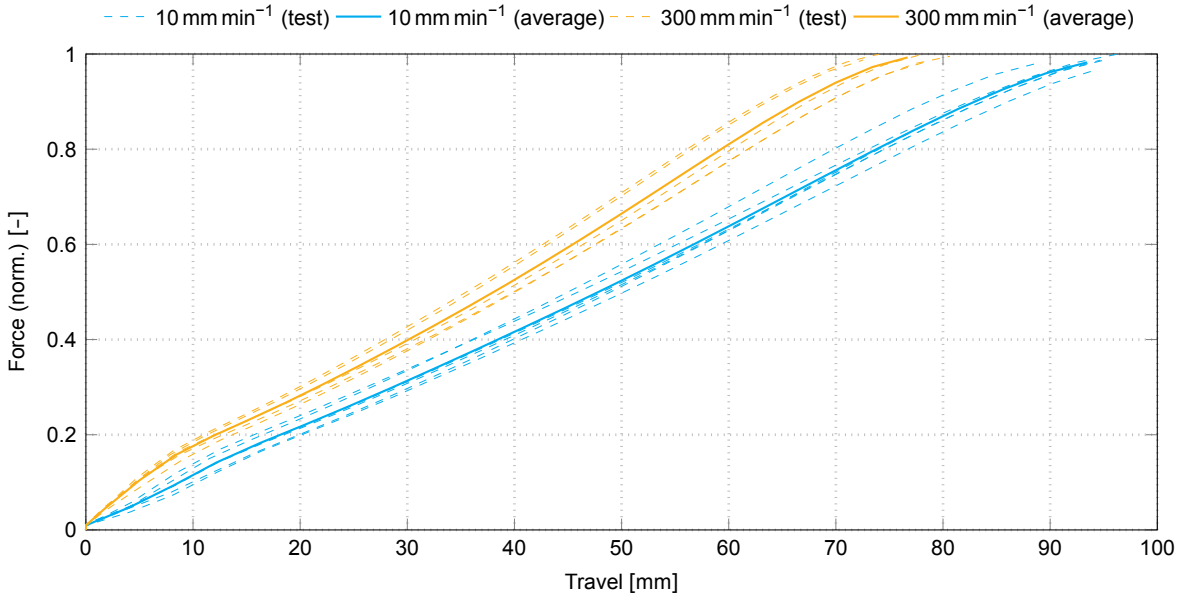

Figure A.2: Force-displacement data of fibre tensile test 1

In Figure A.2 the effect of the travel rate on the tensile properties of PET 1100 2x3 can be seen. The average breaking strength and travel at break are displayed in Table A.1. The standard deviation on the travel at break is caused by the strain variability on the spiral guides, where the (local) strain is limited by friction forces. The forces at break, however, have little variation.

Table A.1: Mean force and travel at break with different travel rates

Travel rate	**Force**		**Travel**	
[mm min^{-1}]	Mean [N]	Std Dev [%]	Mean [mm]	STDEV [%]
10	[redacted]	1.1	93.4	2.7
300	[redacted]	0.7	76.7	3.9

A higher travel rate can be observed to increase the fibre strength but decrease the failure strain, resulting in stiffer behaviour. Since pressurization of the LBH is a slow process (±10 min until burst), subsequent cord tensile tests will be performed at (4 %) 10 mm min^{-1}.

A.2. Force-strain measurements

Continuing on the conclusions drawn in the previous cord tensile test, another set of tests is performed to obtain strain data. The spiral end fixtures do not allow to accurately determine an original (effective) nominal gauge length, as strain in the cord around the spiral guide is reduced due to friction. Therefore, an extensometer will be used to accurately measure the elongation of a unconstrained specimen section.

A.2.1. Test objective

The aim of this test is to obtain force-strain data of PET 1100 2x3 cords, at a travel rate which is representative of working conditions of cord-rubber hoses.

A.2.2. Test setup

Spiral end fixtures were used to mount the cords in the test bench. The cords are clamped and subsequently wound around a spiral guide with a 40 mm diameter, which allows for a gradual load introduction. The centres of the spiral end fixtures have a vertical separation of 500 mm. The travel rate, following the conclusions of the first test, was set at (4 %) 20 mm min^{-1}.

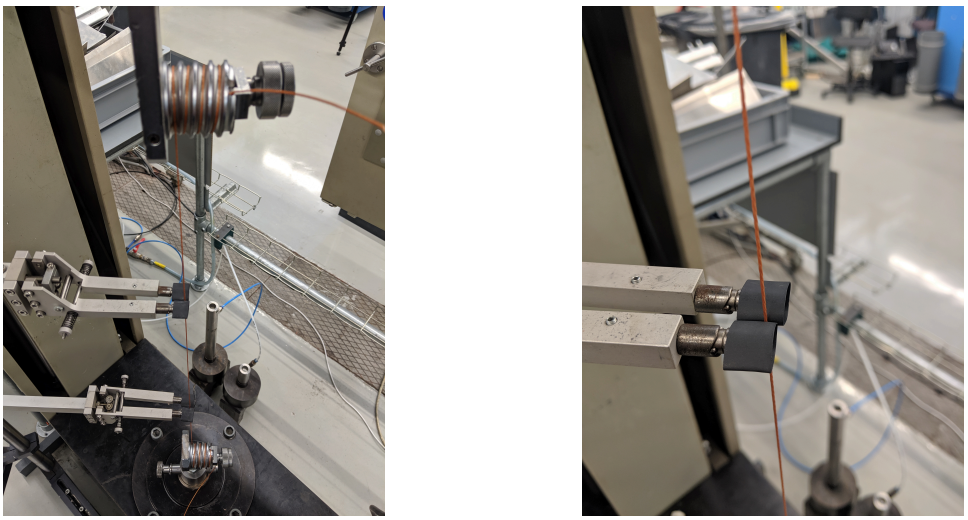

(a) Overview (b) Close up of padded extensometer

Figure A.3: Test setup using spiral end fixtures and extensometer

The extensometer was centred between the end fixtures with a vertical separation of 250 mm. It was attached to the specimen after straightening the cord by applying a 5 N tensile load. Figure A.3a shows the test setup with extensometer, where the horizontal arms grab onto the cord to measure the elongation. The sharp edges of the extensometer caused local damage to the filaments, resulting in premature failure near the extensometer heads (around 250 N with large deviation). To prevent the sharp edges of the extensometer from damaging the cord specimen, shrinking tape was applied for the subsequent tensile tests (shown in Figure A.3b). This resulted in specimen failure to occur again near the spiral guides, consistent with the observations in Appendix A.1. The initial test data showing premature failure caused by the extensometer was discarded.

A.2.3. Observations

Failure of the specimen was observed to occur consistently near either of the spiral guides, consistent with Appendix A.1. Figure A.4a shows the extensometer measurements of 10 tests, with Table A.2 providing the average force and strain at break (visualised by the thicker line in Figure A.4a). The extensometer measurements differ significantly from the data provided by the supplier, with a 21 % lower strain and a 7 % lower force at break.

Table A.2: Mean force and strain at break of extensometer measurements

	Force [N]	**Strain [%]**
Mean	[redacted]	13.31
STDEV [%]	1.4	2.3

Figure A.4b shows the mean force-strain curve of the extensometer measurements (*Extensometer*) and its respective curve if the strain was calculated based on the crosshead travel (*Crosshead*). The strain at break of the latter is 60 % higher than what is measured by the extensometer. Since ±500 mm is wound around each spiral end fixture (4 loops with a 40 mm diameter), the actual specimen is three times longer than the initial crosshead separation. As a result the strain based on crosshead travel will be higher than the extensometer measurements.

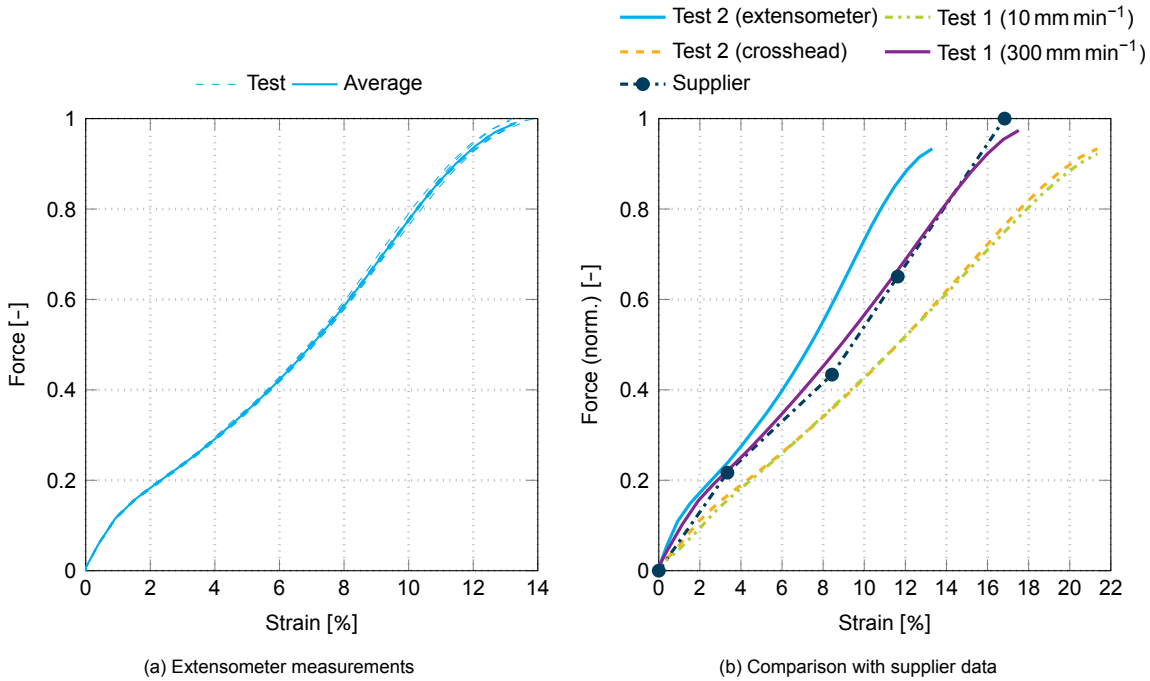

(a) Extensometer measurements

(b) Comparison with supplier data

Figure A.4: Force-strain curves of the cords measured using an extensometer

The crosshead-based strain ε^{CH} is obtained by the crosshead travel ΔL^{CH} and the initial gauge length (crosshead separation) L^{CH}:

$$\varepsilon^{\mathrm{CH}} = \frac{\Delta L^{\mathrm{CH}}}{L^{\mathrm{CH}}} \tag{A.1}$$

The average force-displacement curves of (4 %) 10 and (120 %) 300 mm min^{-1} strain rates in Figure A.2 show the effect of the strain rate on the tensile properties. The slopes of these curves indicate the stiffness of the cord specimens at different strain rates. Since during the first test the crosshead travel was measured instead of the strain, the travel data (i.e. *x*-axis) of both curves has to be transformed into approximate strain to allow a stiffness comparison between the (second) test data and what is provided by the supplier. The crosshead-based strain of the second test $\varepsilon_2^{\mathrm{CH}}$ is calculated using Equation (A.1) and shown in Figure A.4b. Subsequently the average force-displacements curves of the first test are overlayed, where the crosshead travel $\Delta L^{\mathrm{CH}}_{\{10,300\}}$ is scaled using Equation (A.2), retaining the relative stiffness ratio.

$$\bar{\varepsilon}^{\mathrm{CH}}_{\{10,300\}} = \Delta L^{\mathrm{CH}}_{\{10,300\}} \frac{\varepsilon^{\mathrm{CH}}_{2_{\max}}}{\Delta L^{\mathrm{CH}}_{10_{\max}}} \tag{A.2}$$

The stiffness ratio between the supplier data and the *Crosshead* curve is comparable to that between the 10 and 300 mm min^{-1} curves. Since the supplier confirmed having used friction based end fixtures and assuming the ASTM D885 [58] test standard was followed (i.e. a strain rate of 120 % nominal gauge length per minute), the difference between the force-strain data measured with an extensometer and the supplier data is explained. It is however more accurate to use tensile properties measured using an extensometer, since the friction acting on the fibres around the clamps has no effect on the measured elongation.